

# Dissociation Dynamics of Unstable Molecular Systems

A Thesis

*submitted for the award of Ph.D. degree of*

MOHANLAL SUKHADIA UNIVERSITY

in the

*Faculty of Science*

*by*

**Amrendra Kumar Pandey**



*Under the Supervision of*

**Dr. Bhas Bapat**

Associate Professor

Space and Atmospheric Sciences Division

Physical Research Laboratory

Ahmedabad, India

**DEPARTMENT OF PHYSICS  
MOHANLAL SUKHADIA UNIVERSITY  
UDAIPUR**

**Year of submission: 2014**



## ***DECLARATION***

I, **Mr. Amrendra Kumar Pandey**, S/O Mr. Ram Bihari Pandey, resident of Room No:101, PRL Thaltej Hostel, Thaltej, Ahmedabad-380054, hereby declare that the work incorporated in the present thesis entitled, “**Dissociation Dynamics of Unstable Molecular Systems**” is my own and original. This work (in part or in full) has not been submitted to any University for the award of a Degree or a Diploma. I have properly acknowledged the material collected from secondary sources wherever required. I solely own the responsibility for the originality of the entire content.

Date : May 26, 2014

(Amrendra Kumar Pandey)



## *CERTIFICATE*

I feel great pleasure in certifying that the thesis entitled, “**Dissociation Dynamics of Unstable Molecular Systems**” embodies a record of the results of investigations carried out by Mr. Amrendra Kumar Pandey under my guidance. He has completed the following requirements as per Ph.D. regulations of the University.

- (a) Course work as per the university rules.
- (b) Residential requirements of the university.
- (c) Regularly submitted six monthly progress reports.
- (c) Presented his work in the departmental committee.
- (d) Published minimum of one research paper in a refereed research journal.

I am satisfied with the analysis of data, interpretation of results and conclusions drawn. I recommend the submission of thesis.

Date : May 26, 2014

Dr. Bhas Bapat  
(Thesis Supervisor)  
Associate Professor,  
Physical Research Laboratory,  
Ahmedabad, India

Countersigned by  
Head of the Department



# Contents

<b>Acknowledgements</b>	<b>ix</b>
<b>Abstract</b>	<b>xiii</b>
<b>List of Publications</b>	<b>xv</b>
<b>Acronyms and Abbreviations</b>	<b>xvii</b>
<b>List of Tables</b>	<b>xix</b>
<b>List of Figures</b>	<b>xxi</b>
<b>1 Introduction</b>	<b>1</b>
1.1 The origin of new physics . . . . .	1
1.2 Development of theoretical methods . . . . .	5
1.3 Development of experimental methods . . . . .	6
1.4 Motivation of the work . . . . .	9
1.5 Overview of the thesis . . . . .	10
<b>2 Experiment</b>	<b>13</b>
2.1 Collision processes and measurement of kinematics . . . . .	13
2.2 Kinematics of dissociative ionization . . . . .	14
2.2.1 Preparation of the initial state . . . . .	15
2.2.2 Measurement of the final state . . . . .	15
2.3 The measurement scheme . . . . .	16
2.3.1 Recoil Ion Momentum Spectrometer . . . . .	17

2.4	The experimental set-up . . . . .	17
2.4.1	Interaction region . . . . .	18
2.4.2	Extraction region . . . . .	18
2.5	Detection of the reaction products . . . . .	21
2.5.1	Charged particle detector . . . . .	21
2.5.2	Position sensitive detector . . . . .	22
2.5.3	Electron detector and signal processing . . . . .	24
2.5.4	Ion detector and signal processing . . . . .	24
2.6	Data acquisition . . . . .	27
2.7	Building the ion momentum vectors . . . . .	30
2.8	Resolution of the RIMS . . . . .	33
<b>3</b>	<b>Data Analysis</b>	<b>37</b>
3.1	Identification of fragmentation pathways . . . . .	37
3.2	Coincidence maps . . . . .	39
3.2.1	Nature of fragmentation . . . . .	39
3.2.2	Mean life time of the transient molecular ion . . . . .	41
3.2.3	Analysis of the fragmentation channels . . . . .	42
3.3	Fragmentation properties from the complete kinematics . . . . .	43
3.3.1	Kinetic Energy Release . . . . .	44
3.3.2	Transient molecular ion geometry . . . . .	45
3.3.3	Anisotropy measurement . . . . .	46
3.3.4	Branching ratios of the fragmentation channels . . . . .	48
3.4	Corrections in the measured kinematics . . . . .	48
3.4.1	Ion transmission losses . . . . .	49
3.4.2	Effect of dead time of the detectors in ion-coincidence . . . . .	51
3.4.3	MCP detection efficiency . . . . .	54
3.4.4	Effect of transmission meshes . . . . .	54
<b>4</b>	<b>Theory</b>	<b>57</b>
4.1	The molecular system . . . . .	58
4.1.1	Separation of nuclear and electronic motions . . . . .	60

4.1.2	Electronic structure properties . . . . .	63
4.1.3	Properties of the PECs . . . . .	65
4.1.4	Vibrational structures of the PECs . . . . .	67
4.2	Dissociative ionization processes in molecules . . . . .	69
4.2.1	Direct processes of dissociation . . . . .	70
4.2.2	Indirect processes of dissociation . . . . .	72
4.3	Methods of calculation . . . . .	75
4.3.1	Linear variational procedure . . . . .	75
4.3.2	Building the N-electron basis functions for SCF method . . . . .	77
4.3.3	Hartree-Fock SCF method . . . . .	79
4.3.4	Configuration interaction SCF methods . . . . .	80
4.3.5	MCSCF, CASSCF and MRCI methods . . . . .	82
4.3.6	Calculation performed . . . . .	84
<b>5</b>	<b>Results</b> . . . . .	<b>87</b>
5.1	The basis of a comparative study . . . . .	88
5.2	The experimental results . . . . .	91
5.2.1	The TOF spectrum . . . . .	91
5.2.2	The T1-T2 correlation maps . . . . .	93
5.2.3	Estimation of CSD-to-ND ratios . . . . .	94
5.2.4	CSD-KER spectrum of N <sub>2</sub> and CO dications . . . . .	97
5.3	The computational results . . . . .	97
5.3.1	Calculation of Potential Energy Curves . . . . .	98
5.3.2	Need of precise calculations . . . . .	100
5.3.3	Calculation of FC Factors and tunneling life times . . . . .	102
5.3.4	Calculation of KER . . . . .	102
5.4	Identification of the KER features . . . . .	103
5.4.1	Direct dissociation channels . . . . .	103
5.4.2	Indirect dissociation channels . . . . .	107
5.5	Calculation of the partial cross sections . . . . .	109
5.6	Conclusions . . . . .	111

<b>6 Summary and discussions</b>	<b>113</b>
<b>A Calculation of transmission loss</b>	<b>117</b>
<b>B Vibrational levels of <math>N_2^{++}</math> and <math>CO^{++}</math></b>	<b>121</b>
<b>Bibliography</b>	<b>125</b>

# Acknowledgements

In my view, acknowledgement is an account of the various sources of support that can not be completely grasped even after recognizing the contributions of the individuals and institutions. Also, for such a long time, like a PhD tenure, it is not only the knowledge and information that is achieved, if it is, it would feel insufficient and be dissatisfying at the end. I consider it as my accomplishment the way I have experienced the human faculties and world views in this time that would have otherwise certainly different. It is my privilege to be a part of the Physical Research Laboratory and I thank all the members of the institution for their support.

First, I would like to express my gratitude to my supervisor Dr. Bhas Bapat for his constant encouragement and guidance. I appreciate his insight and knowledge on the subject and admire his urge for the broader understanding. I am deeply grateful to him for his involvement in my work. I have always benefited from the discussions we had on the subject. In addition, he always inspires me to pursue the independent research. Apart from his role as an adviser, I must acknowledge him for being extremely supportive and I wish to thank him for his patience.

I would also like to thank Dr. K.R. Shamasundar, IISER Mohali, for his support and guidance in the theoretical aspect of this work. I am grateful to him for critical comments and suggestions that proved to be very beneficial.

I am grateful to my group members for their support. I am obliged to Prof. K P Subramanian for his constant encouragement and interest in my work. I acknowledge Dr. I A Prajapati and Dr. S B Banerjee for their assistance in the

experimental work. I am also thankful to Prashant Kumar, V K Lodha for their help in many occasions. I want to thank my seniors Rajesh Kushawaha and Arvind Saxena for their useful suggestions. A special thanks goes to Koushik Saha for his sincere involvement and the discussions we had on the many topics. Apart from this, I thank to the senior members of my group for providing the valuable knowledge about the history and development of this institution. I also find the discussions on the various interesting topics that we had on the tea worth acknowledging. I enjoyed their company and warmth all this time.

I would like to thank Prof J N Goswami, the Director PRL, and Prof. Utpal Sarkar, the Dean, for their support. I must thank PRL academic committee for reviewing my research work and giving suggestions and critical comments. I am also thankful to all the members of SPA-SC division and Laser physics group for their valuable suggestions that emerged out in the seminars. I would like to thank all the faculties who taught me during the coursework. I learned many things from R Ramesh, B Bapat and R Rangarajan. Late Prof D Lal and R K Verma were very inspiring.

I would also like to thank and appreciate the members of the PRL Library, computer center, administration and dispensary for their sincere support. I want to thank the staffs of the canteen, cleaning service, transport service and CISF for their long responsible service and care.

I would like to thank my friends Abhishek, Arun, Chinmay, Koushik, Siddhartha, Sunil, Susanta, Vema and Yogita for making this journey enjoyable. I am deeply grateful for their friendship. In this time, many memorable and meaningful moments belong to their company. I also enjoyed company of Arko, Tonmay, Manojit, Sashi, Fazlul, Priyanka, Gourav, Gulab and many others. I learned many things from them. I am grateful to my old friends Sanat and Aditya for helping me whenever needed. I thank Shaili for her friendship and encouragement. I also thank Diganta for his friendship and pleasant company. A special thanks goes to all the people who made a very healthy and cheerful environment, because of them I really enjoyed

my stay in PRL and Thaltej campus.

Finally, I owe my deepest gratitude to my family members for their unconditional support. They always showed me their trust and encouraged me throughout my PhD years. I am indebted to my mother and father for their wholehearted love. I would like to express the deepest appreciation to my brother, Madhurendra, for helping me in programming and computer skills. I would like to express my regard to my elder brother and his family for encouragement and support. I sincerely appreciate my sisters for giving me time from their occupied lives.



# Abstract

A molecular system is generally viewed as a composite of two sub-systems of electrons and nuclei which are drastically different on the basis of their dynamical time scales. These two sub-systems, however are coupled by the Coulomb interactions. The assumptions and approximations based on the inherent differences in the dynamical properties of the electrons and nuclei are used to construct the picture of a molecule. The resulting model of the molecular system explain and predict many molecular processes very successfully. However, there are processes in which their predictions do fail. Dissociation processes of highly charged molecular systems provide a unique opportunity to examine and explore their nature in this regard. Such studies are employed as a probe to investigate the regime and conditions of the validity of assumptions and approximations that are otherwise remain valid in the molecular processes.

This thesis is concerned with experimental as well as theoretical investigations to explore some of the fragmentation properties of the doubly ionized molecular ions of  $N_2$  and  $CO$ , which are isoelectronic molecules with different symmetries but nearly identical total ionization cross-sections. By combining ab initio calculations with the experimental investigation of the kinematics of dissociative double ionization of these molecules, we have identified various transient states contributing to the dissociation process. Further we have quantified the BO and non-BO processes therein. It has emerged as an important result because of the striking differences between their observed proportions for these dications. The work reported in this thesis empasize the relevance of such comparative studies.



# List of Publications

1. *Charge symmetric dissociation of doubly ionized  $N_2$  and CO molecules*  
A. Pandey, B. Bapat, K.R. Shamasundar, The Journal of Chemical Physics, **140**, 3 (2014)
2. *Effect of transmission losses on measured parameters in multi-ion coincidence momentum spectrometers*  
A. Pandey, and B. Bapat, International Journal of Mass Spectrometry, **361**, 0 (2014)
3. *A comparative study of Dissociative Ionization of  $N_2$  and CO*  
A. Pandey, B. Bapat, K.R. Shamasundar, Journal of Physics: Conference Series, **488**, 5 (2014)



# Acronyms and Abbreviations

AO	Atomic Orbital
CE	Coulomb Explosion
CI	Configuration Interaction
CSD	Charge Symmetric Dissociation
CAD	Charge Asymmetric Dissociation
CSF	Configuration State Function
DI	Dissociative Ionization
DLD	Delay Line Detector
FWHM	Full Width Half Maximum
GTO	Gaussian Type Orbital
HF	Hartree Fock
KER	Kinetic Energy Release
LCAO	Linear Combination of Atomic Orbitals
MCP	Multi Channel Plate
MCSCF	Multi Configuration Self-Consistent-Field
MO	Molecular Orbital
MRCI	Multi Reference Configuration Interaction
PEC	Potential Energy Curve
RIMS	Recoil Ion Momentum Spectrometer
SCF	Self Consistent Field
STO	Slater Type Orbital
TOF/ToF	Time Of Flight



# List of Tables

2.1	A sample of the list mode data file . . . . .	29
B.1	Properties of vibrational levels of $N_2^{++}$ . . . . .	122
B.2	Properties of vibrational levels of $CO^{++}$ . . . . .	123



# List of Figures

2.1	A schematic diagram of the RIMS setup . . . . .	19
2.2	A schematic view of the MCP and micro channel . . . . .	22
2.3	A schematic diagram of the DLD . . . . .	23
2.4	Signal processing of the electron detector . . . . .	25
2.5	Schematic diagram of the data acquisition of RIMS set up . . . . .	26
2.6	Schematic representation of multi-hit coincidence . . . . .	28
2.7	TOF calibration curve for RIMS . . . . .	32
2.8	Transverse and linear momentum distribution of Ar gas . . . . .	34
3.1	A schematic diagram of the time correlation map . . . . .	40
3.2	A schematic diagram of the KER spectrum . . . . .	43
3.3	Schematic representation of the molecular ion geometry . . . . .	45
3.4	Asymmetry parameter $\beta$ . . . . .	47
3.5	Loss corrections in the KER spectrum . . . . .	53
4.1	A schematic representation of the molecular coordinates . . . . .	59
4.2	Properties of vibrational levels of a PEC . . . . .	67
4.3	KER from direct processes . . . . .	71
4.4	KER from indirect processes . . . . .	73
5.1	Illustration of the molecular symmetries of N <sub>2</sub> and CO MOs . . . . .	88
5.2	First-Hit ToF spectrum of N <sub>2</sub> and CO molecules . . . . .	92
5.3	Partial first-Hit ToF spectrum of N <sub>2</sub> and CO . . . . .	93
5.4	Time correlation maps of CSD of N <sub>2</sub> <sup>++</sup> and CO <sup>++</sup> . . . . .	94

5.5	Loss corrected CSD-KER spectrum of $N_2^{++}$ and $CO^{++}$ . . . . .	97
5.6	PECs of $N_2^{++}$ . . . . .	99
5.7	PECs of $CO^{++}$ . . . . .	100
5.8	Identification of CSD-KER features of $N_2^{++}$ . . . . .	104
5.9	Identification of CSD-KER features of $CO^{++}$ . . . . .	105
5.10	Properties of vibrational levels of $N_2^{++}$ and $CO^{++}$ . . . . .	106
5.11	Fractional estimation of the sources of DI using CSD-to-ND ratios .	110
A.1	Illustration of the transmission loss . . . . .	118
A.2	Loss angle and loss factor as a function of ion's energy . . . . .	119

# Chapter 1

## Introduction

### 1.1 The origin of new physics

Up to the very end of the 19th century, atoms were recognised as tiny indivisible particles and the building blocks of the matter. Evidently, to make distinction between different substances, it was hypothesized that there are many types of atoms and that distinction was based on their masses. All atoms of a given element was assumed identical in all respect and their relationship with molecules and compounds was established by the chemical analysis performed by Joseph Priestly (1733-1804), Antoine Lavoisier (1743-1794), Joseph Louis Proust (1754-1826), John Dalton (1776-1844), Joseph Gay-Lussac (1778-1850) and many others. Further, a correspondence between the properties of individual atoms with the thermodynamic properties of the system was assumed to exist by Amadeo Avogadro (1776-1856). The size of the atoms could also be comprehended up to this end. Using the ideas of kinetic theory of gases that was developed by Rudolf Clausius and James Clerk Maxwell and was finally generalized by Ludwig Boltzmann, the first estimates for the sizes of atoms and the number of atoms per unit volume was made by Joesph Loschmidt in 1865. It would be noted that, in fact all the atomic properties were deduced from the measurement on bulk not on the individual atomic/molecular systems. On the other hand, the classical mechanics which was very successful and well established for the classical objects was indisputably

assumed valid for atomic systems.

The idea that atoms are indivisible, indestructible, structureless particles started to unsettle by the new findings from the precise experimental results. The finding of resonances in molecular spectra, discovered by Johann Balmer in 1885 in the spectral "lines" of the Hydrogen, was first to suggest the existence of structure in the atomic systems. The photoelectric effect, which Heinrich Rudolph Hertz reported as a phenomenon in which a charged object losses its charge more readily when illuminated by ultra violet light in 1887 and that was further investigated by Phillipp Lénárd in 1902 was also found to be unaccountable with the classical theory. Later, it complemented the quantum theory of atomic structure. The other notable problems that were not understood by the classical theory are heat capacity of solids and the black body radiation.

The discovery of electrons by J J Thomson in 1897 as a constituents of atoms which were also known to be (negative) charged particles followed by the discovery of nucleus by Rutherford that he showed to be a heavy and tiny positive charged particle (same kind as of alpha particle that was used in the experiment) changed the notion of atomic systems. In 1913, Niels Bohr gave a theory of atomic systems which was competent with the new discoveries of sub atomic particles and the quantum ideas of Planck and Einstein that they have used in explaining the Black body radiation, photoelectric effect and Heat capacity of solids in the preceding years. This establishes the first quantum theory of atoms.

Starting from the Planck hypothesis which was introduced in 1900 by Max Planck, that used quantization (of the properties of the matter) for the first time, it took about thirty years to create a new theory of matter, known as quantum mechanics. The development was guided by many more crucial experimental findings discovered in the period. Franck-Hertz experiment, Stern-Gerlach experiment, X-ray electron scattering by Compton are a few to name. The hypothesis of matter waves by De Broglie, exclusion principle to decide the ordering of the electrons in atoms by Wolfgang Pauli, postulate of the existence of the electron spin by George Uhlenbeck and Samuel Goudsmit and uncertainty principle by Werner Heisenberg were the conceptual leaps that were taken and used to construct the

quantum mechanics. Statistics namely Bose-Einstein and Fermi-Dirac statistics were developed for the two known kind of quantum systems. Also, Paul Dirac developed the quantum theory for electromagnetism. In this period, the two formalism named as matrix and wave formalism for the quantum systems were developed. The wave formulation of the quantum system was developed by E. Schrödinger in 1926, just after the development of matrix formulation by three scientists Werner Heisenberg, Max Born, and Pascal Jordan in 1925. In 1927, Max Born gave the probabilistic interpretation of the quantum mechanics. The development of quantum mechanics can be found in [1–4].

The radical shift from the classical theory that realized to be requisite was the notion of quantization of atomic properties and the inherent uncertainty in the measurement. In the classical theory, there was no limit on the scale of measurement. Under this idea, the properties of the classical systems are ideally deterministic. Also, measurements can be viewed as an act that does not alter the system's property. And the modifications introduced by the measurement was accountable by further means. On the contrary, in the new description of matter, where the properties are quantized, the limiting scale on the measurement imposed by the unit of quantization introduces an inherent uncertainty in the observed properties. This inherent uncertainty in the measurement leads to the probabilistic description, that also assure it as the best possible description of the system [5].

As a result, in the mathematical formulation of the quantum system, each point in space is regarded as the variable to the state, unlike in classical theory in which the state can be completely defined by position and momentum of the particles of the system. This makes even a single particle system an infinite variable problem. This inherent nature of the quantum systems imposes an inescapable condition that the exact solution of the system can not be calculated except for few cases in which analytical solution is possible. In addition to the inherent limit to get the exact solutions, as for classical systems, the nature of many-body system generates a situation in which only numerical solutions are possible. After the basic formulation of the quantum system, the remaining and vital part was and still does to develop methods to obtain accurate solutions for the quantum states.

In the probabilistic description, the one most important concern arises that how a quantum system interact with the other systems and how their properties change in the process of interaction. For example, it became increasingly interesting to see the behavior of atomic systems in the ionization processes. The measured quantities such as the angular distribution of the ejected electrons in the ionization provide the knowledge of the state which is taking part in the interaction. Measuring such kinematical properties are used as a way to probe the properties of atomic and molecular systems in the course of interaction. In addition, it has become intriguing to investigate the nature of interaction of atoms and molecules in these processes in smaller length and time scales. The underlying reason is that the theoretical methods to calculate the quantum states are based on some set of approximations and the precise experiments guide to achieve better understanding of these systems by probing the limits of the underlying assumptions and approximations.

In atomic case, since the constituents of the system namely electrons and nuclei differ in the masses, the approximation of treating nuclei as infinitely heavy objects is used extensively. Under this approximation, for Hydrogen atom, the simplest atomic system, the Schrödinger equation can be solved analytically. For any atomic system bigger than H atom, only numerical solution can be obtained. For heavier atomic systems, the relativistic contribution would also be taken in to account in order to achieve accurate results [6, 7].

In case of molecules, the assumption of treating nuclei as infinitely heavy objects allows to visualize the motion of electrons and nuclei in parts as their dynamical time scales are very different. The approximation of separating the nuclei and electronic motions is called BO approximation. It was first introduced by Born and Oppenheimer in 1927 [8]. It is the very soul of the quantum chemistry and is extensively used in describing the properties of the molecules and molecular reactions. In this picture, the nuclei motion is governed by a mean field created by the electrons of the system. The motion of nuclei is generally visualize on the function known as potential energy surfaces/curves. The BO approximation enables to provide a quantum mechanical description of the concepts of molecular bond, molecular geometry and many other notions which were used to describe the

chemistry of molecules. The mathematical formulation of the BO approximation will be discussed in chapter 4. BO approximation has been very successful in explaining many chemical processes, but also there are many cases where it fails to explain the observed properties [9–13]. It has been a topic of great interest to investigate such processes. In the last three decades, with the advent of sophisticated experimental techniques, better knowledge of the evolution of the system opens up the way to examine the nature of these processes.

## 1.2 Development of theoretical methods

The first many body quantum mechanical calculation was performed by Hylleraas on Helium atom in 1928 [14], which became the basis of configuration interaction (CI) methods. In the same year, a self consistent method for calculating the electronic states of the atoms and ions was first formulated by Douglas R. Hartree [15–17]. Later, this method was improved by Vladimir Fock and John Slater to make it consistent with antisymmetric property of electrons and now is known as the Hartree-Fock Self Consistent Field (HF-SCF) method. In case of molecules, the first numerical quantum mechanical calculation was performed by Walter Heitler and Fritz London on the hydrogen molecule in 1927 [18]. Their method was generalised by John C. Slater and Linus Pauling in later years and now commonly known as Valence Bond theory. An alternative method to achieve the approximate solutions for molecular systems was developed by Friedrich Hund and Robert S. Mulliken in 1928. In the theory, they introduced the concept of molecular orbitals. John Lennard-Jones proposed to write the molecular orbitals as the linear combination of atomic orbitals in 1929. In 1938, the molecular orbitals of  $H_2$  were calculated by Charles Coulson. In 1951, Clemens C.J. Roothaan developed the SCF Hartree Fock method using LCAO approximation that established the generalized theory of MO calculation [19]. This also led to many other ab initio methods in the following years.

The development of efficient computer technology starting in the 1940s made feasible to build the sophisticated methods for the calculation of properties of atoms

and molecules. Many post-HF theories like Multi configuration Self Consistent Field (MCSCF), Complete Active Space SCF method (CASSCF), Multi Reference Configuration Interaction (MRCI), Coupled Cluster (CC), Moller Plesset Perturbation theory (MBPT) were developed in the next three decades. Also the time dependent theories that span the molecular dynamics and theories that incorporated relativistic effects were developed. Many new methods were evolved to issue the specific problems in the different fields. In 1970-80s, the first computer packages were build to perform the calculation on various atomic and molecular properties. Many review articles and books on these methods can be found in the literature [20–24]. In this work, high precision non-relativistic calculation, specially for small molecules are of concern. The HF-SCF, MCSCF, CASSCF and MRCI methods, which we have used in the calculation, will be discussed in brief in the chapter 4.

### 1.3 Development of experimental methods

Till the mid of 1960s, collisional experiments on the atomic and molecular systems were concerned about the ionization energies and cross sections [25–27]. The coincidence experiments were started around 1965. The coincidence measurement was first implemented in a atomic scattering experiment performed by V. Abrosimov et. al, they studied  $\text{Ar}^+$ -Ar collisions at 12 and 50 KeV by this technique [28]. Such experiments were used to measure the inelastic energy loss as a function of projectile and target deflection angles and initial projectile energy for the different pair of Ar ions created in the collision [29–31]. The other notable coincidence measurement was performed by H. Ehrhardt et in 1969 [32]. It was the first measurement in which the ejected and scattered electrons from the He atom were detected simultaneously and their correlated angular distribution were recorded. Such experiments are known as (e,2e) experiments [33]. Many similar coincidence experiments were designed for multiple ionization processes [34, 35]. These coincidence measurements emerged to be a remarkable development because it allowed to observe the correlated kinematics between the fragmented systems after collision and provided the better picture of atomic and molecular orbitals [33].

However, in these experiments, the differential energy and angular correlation between incident and ejected electrons was obtained by using separate detectors. The complete kinematics was deduced from the observed coincident events by scanning for all emission angles and energies. Because of this reason, in spite of their nobility, these experiments were of extremely small detection efficiencies. At the same time in these experiments, the angular scanning was performed by rotating the detectors in steps that in turn made them a very time consuming exercise.

In the study of collisional processes of the molecules, the first coincidence measurement was performed by McCulloh et. al in 1965 [36]. In the following years, several coincidence measurement methods were evolved to access the different aspects of the dynamics of the ionization and dissociation of the molecules. These methods were different from each other by the combination of the ejected particles measured in coincidence. Photoelectron-photoion coincidence (PEPICO) [37], photoelectron-photoelectron coincidence (PEPECO) [38] and other experiments based on e-ion, ion-ion [39] coincidence and electron-ion-ion [40–42] coincidence were developed. These coincidence measurements facilitated for the first time the kinematics of different ionization and dissociation channels separately.

In the study of dissociative ionization processes, KER spectra of the dissociation of molecules were reported [39, 43–46] using electrostatic and TOF methods. For the first time, the vibrational structure in the KER spectrum of dissociation of dications could be achieved by DFKER spectroscopy in 1995 [47]. These were the first experiments in which the various dynamical processes could be identified in the resulting KER spectrum upon dissociation. However, the major limitation of these methods was that they measure the kinetic energies of the fragments, not their momentum.

The first experiment based on the measurement of the momentum of the fragments was performed by Ullrich in 1987 in atomic collision experiments. The experiments were performed on the atomic targets (Ne) using high energy heavy-ion atom projectiles. By measuring the TOF of the ions using a TOF spectrometer, they deduced the component of the momentum parallel to the spectrometer axis.

It was used to measure the differential ionization cross section of the target with respect to the projectile scattering angle [48, 49]. The complete momentum measurement of the fragmented ions can be traced in the work performed by Ali et. al. [50] in 1992 and that marked the birth of ion momentum spectroscopy. They employed a combination of TOF method and the position detection to measure the energy loss in a collision experiment of 50 KeV Ar<sup>15+</sup> on Ar. The TOF and position information were used to calculate the longitudinal momentum components of the ions and the energy loss in the collision. They also established the possibility to extract all the three component of momentum of ions in the work [50, 51].

These Ion momentum spectrometers (IMS) were able to provide the complete momentum vectors of the recoil ions with a good momentum resolution covering the almost  $4\pi$  sr solid angle of the reaction volume [52]. Since each momentum component of the ions are measured separately, such measurement access the entire kinematical space of the collision. Consequently, any derivative properties of the collision can be deduced from the measured parameters.

In the next step, the reaction microscopes [53] were build to measure the complete momentum vectors of ions and ejected electrons simultaneously in coincidence. The first experiment measuring the complete kinematics of single ionization of He by impact of Se<sup>28+</sup> was reported by Moshhammer et. al [54, 55]. Using ion momentum spectrometer, the complete kinematics of double ionization of Helium was performed by Bapat et. al and many others [56–58]. These experiments provided the better angular resolution for the differential collision cross sections than that was achieved by conventional (e,2e) type experiments.

The use of the ion momentum spectrometer was very soon realized in the study of molecular reactions [59, 60]. After employing the multi-particle detection, it has become powerful tool to measure the dissociation dynamics of unstable molecular systems. The details of an ion momentum spectrometer, especially a recoil ion momentum spectrometer will be discussed in the chapter 2. The other notable technique, that are used extensively for studying the molecular reactions is velocity map imaging (VMI). There are many articles available in the literature on these techniques [61, 62].

## 1.4 Motivation of the work

With the advent of the complete kinematic measurement of the products of evolution of the transient state of the atoms/molecules in the collision processes and possibility to calculate their quantum states with a very high precision, now it has become possible to understand the dynamical evolution of the system. Ionization of atomic and molecular systems are one of the much studied processes in this regard. When an atomic/molecular system interact with some ionizing element that provides sufficient energy to the system for ionization, ionization takes place. The angular distribution of the ionized electrons is related with the nature of the perturbation and the shape of the orbital, and thus become a source to probe the participating orbitals in the ionization. The ionization of the atomic and molecular systems has been probed in very small time scales in order to get more detailed nature of the process. With the advent of femto and atto second lasers, the snapshots of these processes in the real time scale are now possible to observe [63–65].

On the other hand, the nature of dynamical evolution in the dissociation process is different from the ionization because of the involvement of significant motion of nuclei. The motion of nuclei and electrons in a molecular system normally follows dynamics of different time scales because of the large differences in their masses. The BO approximation which allows to separate the dynamics of electronic and nuclei motions defines potential functions for the motion of nuclei in the molecular system. The process of dissociation can be visualized on these potential functions known which are known as potential energy surfaces/curves (PES/PEC) under BO approximation. In this picture, the nature of the PEC will decide the evolution of the transient molecular system that may undergo dissociation. If the PEC is purely repulsive in nature, the dissociation from such state is inevitable. The other cases in which, PEC possess a local minima, in the course of evolution, dissociation depends upon the additional factors. Such PECs support vibrational levels and dissociation from the vibrational levels depends upon the tunneling life time of the state, which is given by the tunnelling width and the tunnelling height for the state. In such cases, it is essential to know the vibrational structure of the PECs in order to know

their contribution in the dissociation. Under BO approximation since it does not allow coupling of different states of the system, dissociation can occur from either a repulsive state or vibrational states having small tunneling life time. These are called direct dissociation processes. On the other hand non-BO processes which allow coupling between states may be seen as another source of the dissociation. It is a matter of great interest to identify these sources of dissociation that in turn provide the nature of the dynamical evolution. The BO and non-BO mechanisms in the dissociation can be identified by comparing the experimental kinematics with the predicted kinematics in the picture of PECs of the dissociation.

In the dissociative ionization process, ionization of the molecule happens by collision with some ionizing element as a first step. After the formation of ionized molecular ion which happens in very small time period, dissociation occurs depending upon the nature of the potential curve on which it is created. The study of dissociative ionization is tractable over dissociation because in general there are many PECs which are excited in the formation of molecular ion i.e. in the ionization process. This opens up many possibilities for non-BO dynamics to happen and become more suitable candidate for such studies. On the other hand, in case of dissociation of a neutral molecule, normally it happens on the single PEC and the excited states of the system are in general separated by a large energy and thus are virtually non-interacting.

## 1.5 Overview of the thesis

In this thesis, the study on the dissociative ionization of doubly-ionized  $N_2$  and CO are presented. Experiments to observe the kinematics of dissociation have been performed on these molecules. Recoil ion momentum spectrometer is used to record the kinematics of dissociation products. We have also performed ab initio calculation on these molecules. Under BO approximation, the kinematics of the dissociation have been analyzed and compared with the experimental kinematics. We identify the BO and non-BO sources in the dissociation of these dications. We also provide a partial quantification of the BO and non-BO processes in the

dissociation of these dications by comparing their kinematics. This thesis put a comprehensive analysis of dissociation of these dications. It presents a more exhaustive and accurate theoretical analysis of the process and also on the experimental ground, it accounts various corrections in order to get accurate cross sections. The comparative study that we have performed on the dissociative ionization has been shown to brought up many features about the nature of dynamics that was not possible with separate case analysis.

In the second chapter, the experimental method for complete kinematic measurement has been introduced. A brief account of the Recoil Ion Momentum Spectrometer has been discussed. List mode data acquisition and the multi hit detection system has also been discussed in the view of capturing the correlated kinematics of the dissociation ionization. Finally, the calculation of the momentum vectors of the ions from the observed quantities is derived. A brief account of the resolution of the RIMS set up is also provided in the end.

The third chapter deals with the derivation of the various kinematical properties of dissociation from the observed parameters, and is divided in the three major parts. In the end of the chapter, corrections in the observed kinematics that is required to account the various losses and instrumental efficiencies are given.

In the fourth chapter, an account of the theoretical picture of the process of dissociative ionization is given. The various methods that has been used to calculate the electronic states of the molecule are discussed. Calculation of the vibrational levels, Franck Condon factors and tunneling life time are also provided.

In the fifth chapter, we discuss the Charge Symmetric Dissociation of dications of  $N_2$  and  $CO$ , observed in electron impact collision experiment. A detailed analysis of their dissociation is given in the chapter.

Chapter six summarizes the work done in the thesis and presents a discussion on its relevance and future directions.



# Chapter 2

## Experiment

In this chapter, the experimental techniques for obtaining the complete kinematics of dissociative ionization are described. In the first section, the general features of a collision experiment are reviewed. The kinematics of a dissociative ionization in the context of a collision experiment are discussed in the section 2.2. The experimental scheme to record the kinematics of dissociative ionization and the component of a recoil ion momentum spectrometer are described in section 2.3. In the next section, details of the experimental setup used in this study are provided. In section 2.5, measurement of the kinematical parameters and the properties of the detectors are given. Data acquisition system is described in the section 2.6. The derivation of the momentum vectors from the recorded parameters and the energy and momentum resolutions of the RIMS are covered in the last two sections.

### 2.1 Collision processes and measurement of kinematics

Collision processes are used to study the nature of interaction between two separate systems that are allowed to interact in a certain manner and are generally referred as projectile and target depending upon the way the collisions are performed in experiment. In context of atomic and molecular physics, it is generally used to probe the properties of atomic and molecular systems. In these cases, projectiles

(which is normally electrons, photons and ions) are used as a means of perturbation to the target atomic or molecular system. In experiments, it is performed by making the stationary target bombarded with the projectile. Depending upon the strength of perturbation caused to the atomic and molecular system, different aspects of the electronic structure such as properties of excited states, ionization, dissociation in case of molecules of these systems can be studied [61, 66].

To measure the strength of perturbation which is about the energetics involved in the collision and its effect on the system which is about how system dynamically evolve afterward, two states namely initial (before collision) and final (after collision) states are defined. In both states the interaction with projectile is zero and thus their differences are employed to measure the kinematics of the interaction.

## 2.2 Kinematics of dissociative ionization

In the collision processes which involve break up of the system (viz ionization, dissociation) into smaller systems, kinematics of the each sub-system created in the collision is essential to measure. Such measurements are called complete kinematic measurement and are able to provide the properties of the interaction. The process of dissociative ionization (DI) involves ionization as well as dissociation of the molecular system. Since the ionization process is extremely fast as compared to the dissociation, DI can be viewed as a two step process, in which first the ionization takes place and then the molecular ion dissociates into its fragments. In order to get the complete kinematics, it is essential to measure the kinematics of each fragment created in the process as well as kinematics of the electrons ejected in the ionization. Because of the large difference in the dynamical time scale of the processes, the complete kinematics can be divided into two parts; the kinematics of ionization and of dissociation. Studying these two parts separately provide almost accurate picture of the DI as far as the difference in their dynamical time scales is large. In this picture, the kinematics of ionization deals with energy and momentum sharing of electrons ejected in the ionization process. On the other hand, kinematics of the fragmented ions provide properties of the dissociation of

the produced molecular ion in ionization.

To measure the kinematics of DI in a collision event, molecular systems which are prepared in a certain initial state are allowed to interact with the projectile. The kinematics of the final state of the system is recorded after the collision. It is important to mention that the initial and final state of the system must be uniquely determined in order to derive the kinematics of the process precisely, however this is an ideal situation and is limited by a number of experimental factors.

### 2.2.1 Preparation of the initial state

The molecules are prepared in a particular state that defines the initial state of the system before collision. For the study of dissociative ionization the relevant energy scale is the vibrational scale (sub-eV energy) of the molecular system and thus having all the molecules in a single vibrational level is appropriate and essential. In experiments, before collision, the molecules are normally prepared in the zeroth vibrational level of their ground electronic state. Since the excited vibrational levels of the molecules in their ground state are widely separated from the zeroth level, at any constant low-temperature ( $\sim 300$  K) only the zeroth vibrational level of the molecule will be populated and thus can be readily taken as initial state of the system. For instance, in case of  $N_2$  molecule, the first vibrational level of the system will be populated only 1 in ten thousand relative to its zeroth vibrational level and thus would contribute negligibly small in the kinematics of the dissociative ionization. Population in other excited vibrational levels of the ground electronic state would be even smaller and can be safely neglected.

### 2.2.2 Measurement of the final state

In dissociative ionization, the fragmented partners of the molecular ion gain kinetic energy from the dissociation. The complete kinematics of dissociation can be probed by measuring the momentum of each fragmented partner. Since the interaction between dissociating partners, if they are charged ions is Coulombic, ideally it will never become zero. But in order to distinguish the dissociation energies arising

from different vibrational levels and electronic states in the dissociation, a few ten thousands Å of separation, which is still in atomic scale, between fragmented partners is sufficient to assume them non-interacting systems. The further evolution of the system do not change their kinematics. This defines the final state and is also termed as the asymptotic limit of the system.

## 2.3 The measurement scheme

In the DI process, the fragmented ions gain kinematic energy in the dissociation. An ion momentum spectrometer measures the parameters resulted due to the kinematics of the ions gained in the collision. In order to deduce the kinematics of the ions from the measured parameters, in the ion momentum spectrometer, two conditions are employed. The collisions are allowed to happen in a very small region called interaction region. The volume of the interaction region would ideally be zero. The other constraint imposed is that all the molecules have zero kinetic energy before the collision. This assumption ensures that the deduced kinetic energy is arising entirely from the collision process. The kinematics of the fragmented ions are obtained by using the recorded parameters under these two assumptions. On the other hand, in reality, the finite size of the interaction region and non-zero energy of the molecules before ionization, appear as limit of the resolution of the spectrometer.

After dissociation, the fragmented partners are allowed to fly some distance, far greater than their asymptotic limit separation, before they get detected at the detector. The reason for detecting these fragmented ions at large distances from the ionization region is to measure their kinematical properties with sufficient resolution. Consequently, it imposes a strict condition on the design of the ion momentum spectrometers to transport the fragmented ions from ionization region to the detector plane preserving their kinematics. This appears as one of the major challenge in building an ion momentum spectrometer to maintain the homogeneity of the extraction fields, used for transportation, in the entire space between the ionization region and the detector. These experimental constraints will be discussed

in the following sections.

### 2.3.1 Recoil Ion Momentum Spectrometer

Since the collisions between the molecules and projectiles are generally not directionally constrained, in order to know the angular dependence of the interaction, it is essential to measure the collision events arising from the entire  $4\pi$  direction. Recoil Ion Momentum Spectrometer (RIMS) collects the collision products from the entire  $4\pi$  direction by guiding the fragmented ions in one direction. This is achieved by employing a combination of unidirectional electric fields from the interaction region up to the detectors. Accordingly, instead of using a  $4\pi$  detector it uses a planar detector, placed in the plane perpendicular to the extraction fields. A schematic diagram of the components of a RIMS is given in the Figure 2.1. RIMS utilizes the combination of time-of-flight (TOF) technique with position imaging detection to measure the complete momentum vectors of the fragmented ions [62, 67, 68]. The TOF of an ion which is defined as the time the ion takes to reach the detector from the ionization region depends upon its mass to charge ratio and the longitudinal component of the initial momentum. The TOF measurement provide the identification of the detected ions as well as their longitudinal components of the momentum. The two transverse components of momentum are calculated from the position measurement of the ions on the detector plane. The independent measurement of the quantities (TOF,X,Y) for each ion allows to calculate the free momentum components ( $p_z, p_x, p_y$ ) separately and thus any kinematical parameter can be derived using the recorded data. A review on the RIMS and other momentum spectrometers can be found in [69–71].

## 2.4 The experimental set-up

The entire assembly of the RIMS is housed in a stainless steel cylindrical chamber of diameter 300 mm and height 570 mm. In the ionization plane, it has eight ports to accommodate electron gun, molecular gas beam, faraday cup and remaining

ports are provisional to accommodate other components. The ion and electron detectors are placed on the either side of the ionization plane. The entire chamber is vacuum sealed and continuously pumped by a combination of a 520 litre/sec turbo molecular pump and a dry scroll pump. The working pressure in the entire experiment is always better than  $5 \times 10^{-8}$  mbar. The details of the set up can be found in [72]. The components of the spectrometer are described below.

### 2.4.1 Interaction region

The well localised interaction region is achieved by allowing the collisions between projectile and target in a crossed-beam geometry. The molecules are injected in form of an effusive beam produced by a capillary of inner diameter 0.15 mm and length 12 mm. For the 0.15 mm diameter capillary, the working gas load pressure of few mbar of the reservoir would result a molecular beam of knudsen number equal to about 1, which ensures the thermal equilibrium in the produced effusive beam. A discussion on the effusion property of a molecular gas beam can be found in [73]. The electron beam produced by a 200 mm long electrostatic electron gun are introduced in crossed beam geometry with target beam. The electron source is a directly heated cathode and it uses Einzel lens and electrostatic deflectors for focusing and steering the electron beam. The focal length can be varied over 250–300 mm. The focal spot of the beam is about 0.5–0.8 mm which in combination with the effusive molecular beam produces an ionization region of volume  $3\text{mm}^3$ . A 80 mm diameter faraday cup biased at +30 V is used to collect the electrons after ionization region in the opposite side.

### 2.4.2 Extraction region

A combination of uniform unidirectional electric fields are used to extract the fragmented ions and electrons in opposite directions. The common axis of the extraction fields is taken as normal to the interaction plane in which electron beam and molecular beam lies and it defines the axis of the spectrometer (z-axis in Figure 2.1). The extraction fields are not only meant to collect the collision products from

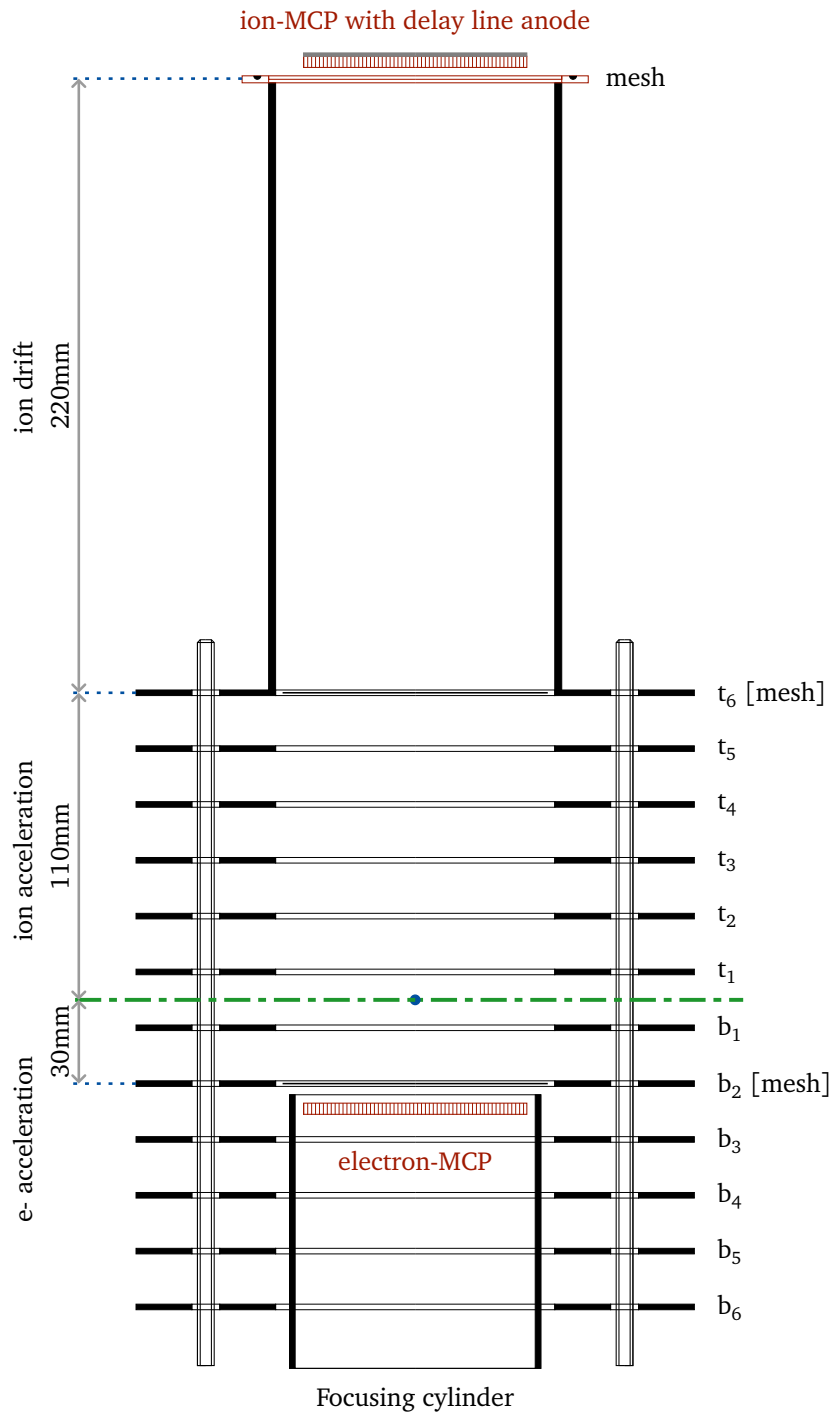


Figure 2.1: A schematic diagram of the RIMS is shown. The horizontal dashed line in between  $t_1$  and  $b_1$  rings is the collision plane, in which the projectile and the molecular beams lie and intersect. The ionization region is shown by a dot in the collision plane. The rings labelled as  $t_6$ - $b_6$  are used to create an uniform electric field used for extraction of ions and electrons.

the entire  $4\pi$  region but also to identify the ions by measuring their time-of-flight. Since the momentum components of the ions are derived from their TOF and two positions on the detector plane under the assumption that there is no field present in the transverse direction and the extraction field is radially constant, it is essential to maintain the homogeneity of the field in the entire region. In RIMS, the homogeneous field region of 100 mm diameter starting from the electron detector and extending up to the ion detector, that is sufficient to entirely enclose the ion detector of diameter 80 mm, is divided into two parts, the acceleration region in which the electric fields are applied and the drift region which is a field-free region. Acceleration region is created by using co-axially stacking of 12 thin aluminium rings. For the drift region, a 100 mm diameter aluminium cylinder is used. Each ring used in the acceleration region is 2 mm thick having 100 mm inner and 200 mm outer diameter. They are co-axially stacked, each separated by 20 mm distance and assemble a 220 mm long cylindrical arrangement for acceleration region. Figure 2.1 shows the details of the arrangement. The horizontal dashed line represents the ionization plane. Whereas, the dot in the middle of the ionization plane represents the ionization region. The stacking of the 12 rings are marked by  $t_1$ - $t_6$  and  $b_1$ - $b_6$  with respect to the ionization plane. The region in between ionization plane and  $t_6$  is used for ion acceleration. Whereas, the region below ionization plane is used for electron acceleration. The potential divider arrangement is employed for generating electric field in the region starting from  $b_6$  to  $t_6$ . The applied potential is equally distributed across the rings using 100 k $\Omega$  resistors of very high tolerance and low temperature coefficient. The measured values of the applied potentials of the rings deviate less than 0.05% to their nominal values. The potential applied across top and bottom rings are such that the interaction plane lies at the zero potential.

The drift tube, an aluminium cylinder of length 220 mm, placed after the  $t_6$  ring is also at same potential as the  $t_6$ . The length of the drift tube is in accordance with the first order Wiley-McLaren space focusing condition which states that the drift region length to be twice of the length of the ion acceleration region. The first order Wiley-McLaren space focusing condition is a geometrical condition to minimise the

effect of finite size of the ionization volume on the TOF of ions travelling through the extraction region [74].

The ring  $b_2$  (30 mm below the ionization plane),  $t_6$  (110 mm above the ionization plane) and the top of the drift tube contain high transmission wire meshes to improve the homogeneity of the field across the spectrometer. The transmission coefficient of the wire meshes is 95%. The uniformity of the electric field estimated by the simulation is better than 1 in  $10^3$ .

The extraction field accelerates ions upward and electrons downward, created in the ionization volume. The field strength used in the study is 60 V/cm, which is high and lead to poorer resolution, but essential to record the high energy dissociation products. The resolution of the RIMS and the energy dependent loss will be discussed in the sections 2.8 and 3.4.1 respectively.

## 2.5 Detection of the reaction products

In RIMS, for detecting reaction products of collision, microchannel plate (MCP) and delay line detector are employed. These are charged particles detectors and thus RIMS is able to capture the kinematics of collisions involving only ionic products. MCPs are large surface area planer detector and are used to detect electrons and ions. The delay line detector is used for position measurement of the ions reaching the MCP employed for ion detection.

### 2.5.1 Charged particle detector

A MCP is a large surface area planar detector consisting densely packed parallel arrays of micro-channels of typical size of  $10\ \mu\text{m}$  and average separation of  $15\ \mu\text{m}$ . The inner wall of the micro-channels are coated with a semiconducting material which serves as secondary electron multiplier. When a charged particle enters in one such channel, it causes a secondary electron emission which grows and accelerated toward the back side by the potential difference maintained between the ends of the MCP. The tubes of the micro-channels are stacked with very small

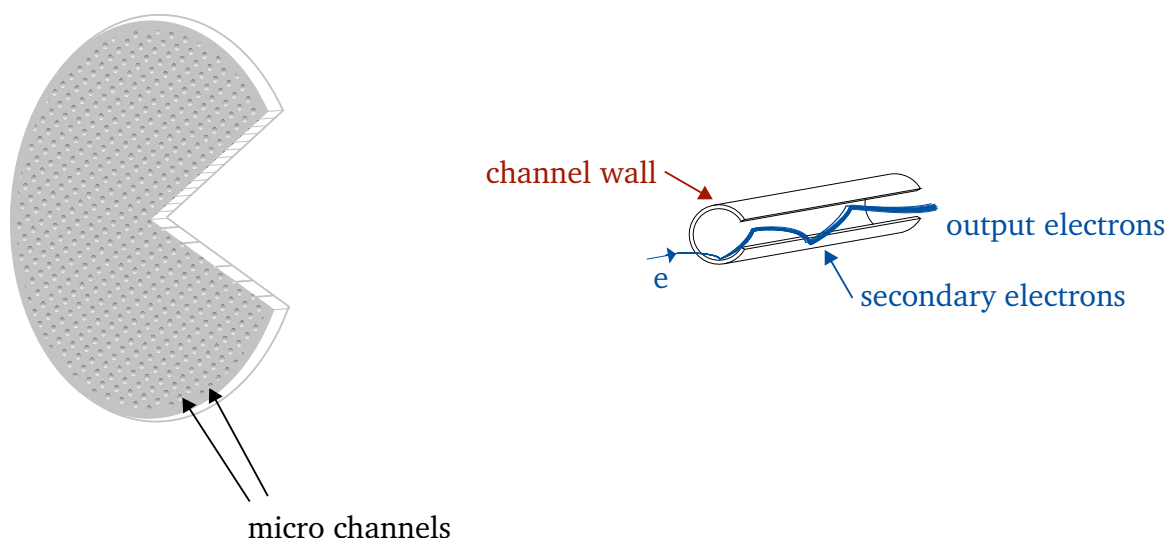


Figure 2.2: A schematic view of the MCP and micro channel is shown. MCP consists of many micro channels each produces a separate signal and thus is suitable for the position measurement. In the right side, a charged ion/electron causing the secondary electron emission in the micro channel is illustrated.

angle (about  $8^\circ$ ) with the plane of the detector to increase the probability of multiplication. The typical gain from each channel is about  $10^4$ . Normally, a stacking of two or three MCPs are used to increase the gain and are referred as Chevron or Z-stack configurations, respectively. The width of a single MCP is about 2 mm with standard available diameters of 40 mm, 80 mm etc. The resulted electron bunch on the back side of the MCP is collected by an anode and represents the detection of the charge particle. In the MCP, each micro channel produces a separate signal which are spatially confined, that makes the MCP appropriate for the position measurement. A schematic diagram of a MCP and the process of signal generation from a micro channel are shown in the Figure 2.2. A more detailed discussion of the properties of MCP can be found in [75].

### 2.5.2 Position sensitive detector

A delay line anode is used in combination with MCP for position measurement [76]. A delay line is a bare copper wire stretched across on an insulating plate maintaining

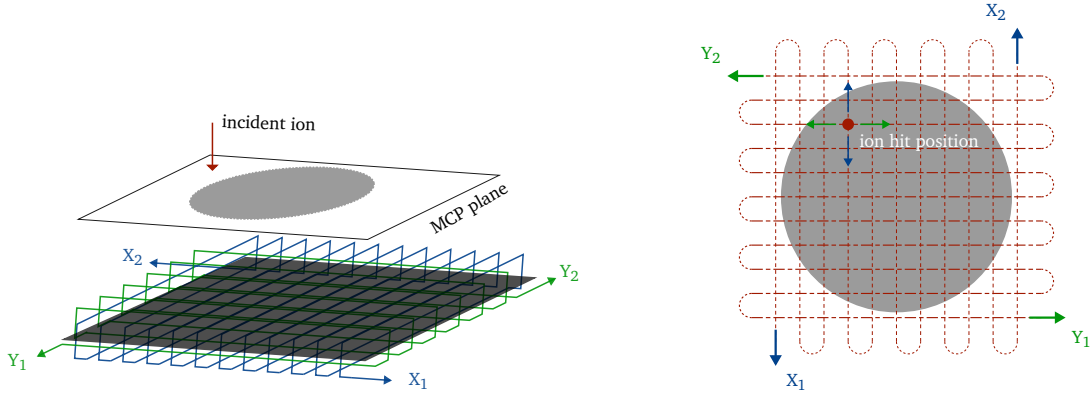


Figure 2.3: A schematic diagram of the side view [left] and top view [right] of the delay line detector coupled with MCP is shown. In the top view, the ion hit position on the MCP plate is shown by a dot. The propagation of the x,y signals are shown by arrows near the ion hit position. The collection of these four signals at the end of the delay lines is also shown.

a constant separation (which is about 0.5 mm) between the consecutive loops. For 2D position measurement, two crossed-pairs of isolated wires are used. When the electron shower from the back of the MCP plate falls on the wire at some position, it causes two image signals that travel to the opposite ends of the delay-line. The time difference between the signals at the end of the delay line is proportional to the distance of the electron shower from the mid-point of the delay line. In case of crossed pair delay lines, their mid-points are kept common and it defines the center from where position (x,y) of the charged particle is measured. It can be expressed as

$$x = (t_{x1} - t_{x2})v_{signal}, \quad y = (t_{y1} - t_{y2})v_{signal} \quad (2.1)$$

Where  $v_{signal}$  is the pulse propagation velocity along the delay-line and is almost equal to the speed of light. On the other hand, sum of the propagation time of the signals travelling to the opposite ends of the detector will only depend upon the total length of the delay-line and will be identical for all ions irrespective of their positions. This condition is used as a consistency check for the genuine signals. A

schematic diagram of a DLD (delay line detector) coupled with a MCP is shown in the Figure 2.3.

### 2.5.3 Electron detector and signal processing

For detection of ejected electrons in the ionization process, 40 mm diameter MCP is used in Chevron configuration. A schematic diagram of the electrical circuit of the MCP for the electron detection (e-MCP), generating a signal for the incident electron is shown in the Figure 2.4. The front of the e-MCP, faces the interaction region and receives ejected electrons from the ionization region. To generate the signal corresponding to the incident electron, a constant voltage difference is applied in between front and back of the MCP. This is achieved by applying +2100 V on the anode that is distributed across the MCP depending upon its internal resistance and the biasing resistances, the one between anode and MCP back ( $R_{b2}$ ) and the other between MCP front and the ground ( $R_{b1}$ ). The internal resistance of the MCP is 120 M $\Omega$  and biasing resistances  $R_{b2}$  and  $R_{b1}$  are 1 M $\Omega$  and 2 M $\Omega$  respectively. The potential on the front and back of the e-MCP can be calculated, which is 35 V and 2080 V respectively. The signal is extracted through a capacitor and resistor and is amplified by a preamplifier of gain value 100. The amplified signal is then fed to a constant fraction discriminator (CFD) and its NIM output is used as START pulse for the TDC.

The e-MCP is placed 40 mm away from the interaction region (in the middle of  $b_2$  and  $b_3$  disks, Figure 2.1). In order to direct the ejected electrons to the e-MCP, a focusing cylinder which is at ground potential has been used. The reason to place the e-MCP far from the interaction region is to avoid the flow of stray ions from the e-MCP to the ion-MCP facing each other. For the same reason a weak barrier potential is applied near the e-MCP.

### 2.5.4 Ion detector and signal processing

Ion detector is a 80 mm Chevron configuration MCP coalesced with a delay-line detector for position measurement. The assembly has 76 mm active diameter

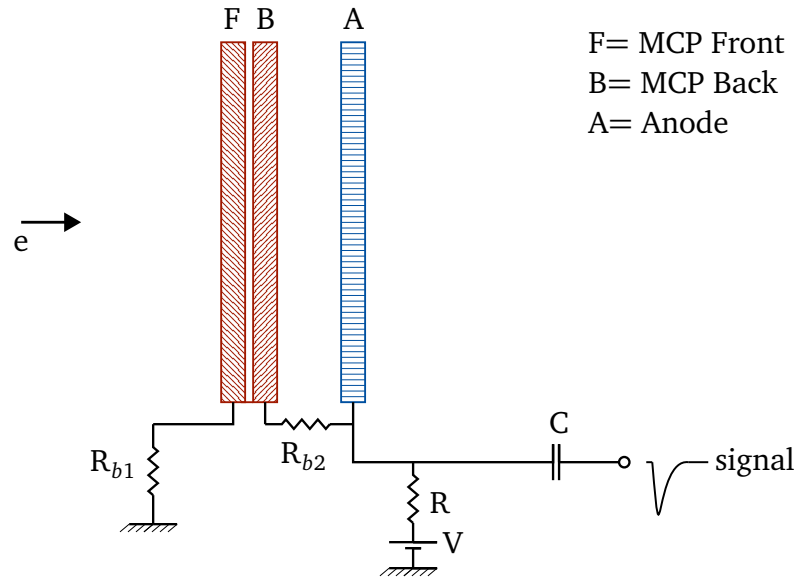


Figure 2.4: A schematic diagram of the MCP for electron detection is shown.  $e$ , on the right side represents the incident electron.  $R_{b1}$  and  $R_{b2}$  are the biasing resistances.  $V$  is the applied biasing voltage. The signal is extracted using a RC circuit.

with  $250 \mu\text{m}$  position resolution and 1 ns time resolution. It has been determined in the previous work on this set up that beyond -3600 V the efficiency of the detector become no more a function of charge of the incident ions by monitoring the  $\text{Ar}^+/\text{Ar}^{++}$  cross section ratio [77]. However, the front of the MCP for the ion detection (ion-MCP) is kept at -2800 V to keep the background ion counts small. The energy (charge) and mass dependence of the incident ions on the MCP efficiency has been studied in the past and will be discussed in the section 3.4.3. We have found that there would be a small variation in the detector efficiencies for the various charged species studied in this work. However, we have taken into account the corresponding efficiencies of the ions while comparing the cross sections of their different fragmentation channels.

The five signals, one from the MCP and four signals from the delay lines are separately amplified by preamplifiers and fed to constant fraction discriminator to generate NIM standard timing pulses. The five NIM outputs are then fed to multi-channel TDC and it conclude the detection of the incident ion with position information.

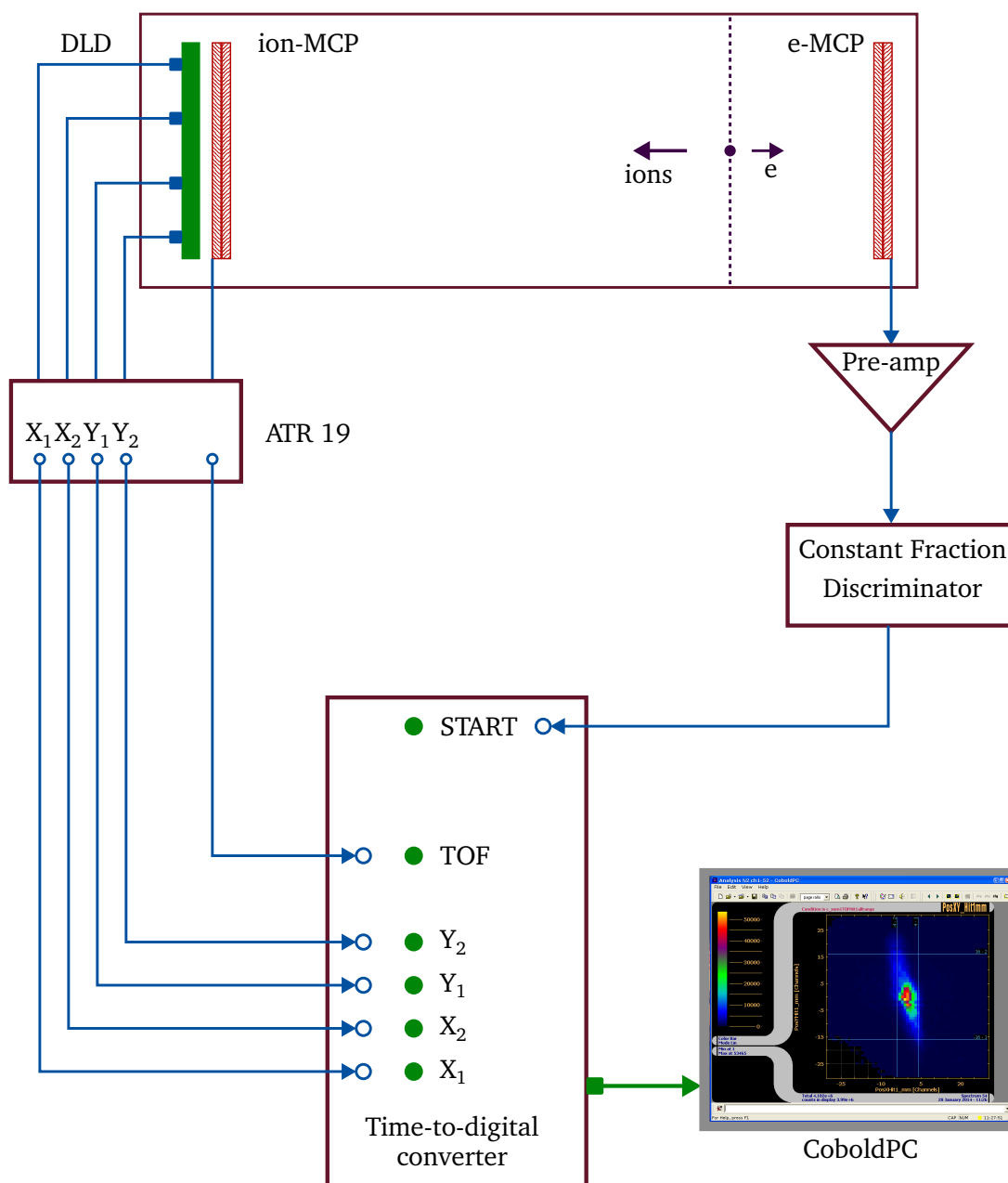


Figure 2.5: A schematic diagram of the data acquisition of RIMS set up is shown.

## 2.6 Data acquisition

Measurement of the kinematics of DI in the RIMS set up is based on the coincidence measurement technique. Occurrence of an event in the RIMS can be defined as detection of an electron and at least one ion (this is called single-coincidence measurement, if more than one ions are observed it is called multi-coincidence) which follow certain timing constraints and collision conditions [78, 79]. Since the ionization process is extremely rapid and small mass of the electron results in almost instantaneous detection after ionization, in the data acquisition the detection of electron is used as a marker of the ionization event. In case of pulsed ionization, the leading edge of the ionizing source pulses can also be used as a marker of the event. The details about the detectors, signal processing and data acquisition can be found in [80].

Data acquisition of the RIMS is based on six timing signals: one from the e-MCP, one from the ion-MCP and four from the delay-line. The e-MCP signal serves as a START for every event and trigger five channels of the TDC to resistor delay-line and ion-MCP signals. The first four channels are stopped by the delay-line signals and the fifth channel is stopped by the ion-MCP signal. The time window for TDC up to which the channels are open is  $32 \mu\text{s}$  with 500 ps resolution. After acquiring an event or after waiting for the maximum limit time window, channel clocks are reset for the next signal on the e-MCP. The data acquisition sequence is shown in the Figure 2.5.

RIMS is capable of multi-ion coincidence (up to quadruple-coincidence) which allows to record the complete correlated kinematics of the fragmentation involving up to four ionic products. It is achieved by enabling the five channels of the TDC to record four timing pulses arriving within  $32 \mu\text{sec}$  time window. The smallest time difference between the consecutive pulses to be recorded is 20 ns which is the dead time of the detectors. The ions detected in the set time window (called Hits) are termed to be detected in coincidence and are taken to be produced in the same collision event. This inference of the multi-ion coincidence measurement is based on the statistical nature of the outcome of the collision. The statistical

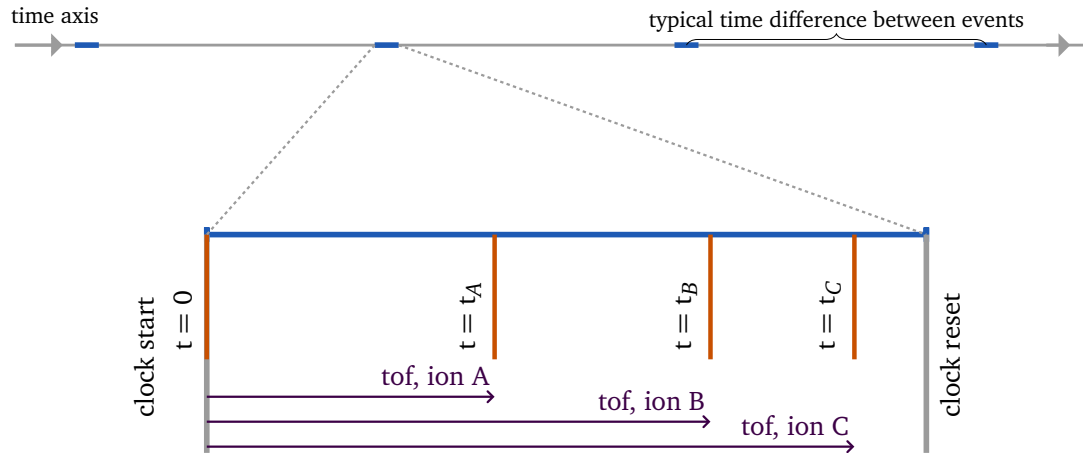


Figure 2.6: A schematic diagram of multi-hit coincidence detection and requirement of well-spaced events is shown. The typical time difference between two consecutive collision events is maintained very large (about 100 times) in comparison to the time window used for multi-hit coincidence (see the text for details).

average time difference between two ionization event is kept very large in the experiments as compared to the time window set for the coincidence detection between ions. The experiments are performed at very low count rate ( $< 300$  Hz), which translates in average time difference of at least 3 msec between consecutive ionization event, that is about 100 times larger than the time window set for coincidence. A schematic of the multi-ion coincidence is shown in Figure 2.6. The horizontal line represents the time axis. The time window of coincidence measurement and the average time difference between two ionization event are also shown.

The digitized outputs from the TDC are stored event by event using a PC interface written in the MS Visual C++ language. The program is provided by the detector manufacturers and is called CoboldPC, which stands for "Computer Based Online-Offline Listmode Data Analyser". The program writes the event into a list mode by using its DAQ (Data acquisition) module. The DAN (Data analysis) module of the program is used for analysis of the list mode data after acquisition. List mode data records the information of each event separately and thus it is very useful in sorting events on the basis of their recorded information. It allows to

Event number	Ion1	Ion2	Ion3	Ion4
...	...	...	...	...
101	$(t, x, y)_{101,1}$	–	–	–
102	$(t, x, y)_{102,1}$	–	–	–
103	$(t, x, y)_{103,1}$	$(t, x, y)_{103,2}$	$(t, x, y)_{103,3}$	–
104	$(t, x, y)_{104,1}$	–	–	–
105	$(t, x, y)_{105,1}$	$(t, x, y)_{105,2}$	–	–
106	$(t, x, y)_{106,1}$	$(t, x, y)_{106,2}$	$(t, x, y)_{106,3}$	$(t, x, y)_{106,4}$
107	$(t, x, y)_{107,1}$	–	–	–
108	$(t, x, y)_{108,1}$	$(t, x, y)_{108,2}$	–	–
...	...	...	...	...

Table 2.1: A sample of a list mode file is shown. The TOF and position information of the fragmented ions observed in coincidence are stored as an event list. Each row represents one collision event. For any event list, the recorded ions are time ordered ( $t_1 < t_2 < t_3 < t_4$ ) each separated by at least 2 ns, having upper limit 32  $\mu$ sec on the TOF.

store every collision products that may result in the experiment. After acquisition, the events of particular interest can be separated and analysed independently. The event list used in our case contains  $(x_1, x_2, y_1, y_2, t)$  entries obtained from delay-line anode and electron-ion coincidence for each recorded ion. In fact the program acquires five timing signals from the corresponding five TDC channels which are converted to the position and TOF information by using appropriate instrument dependent conversion factors.

The embryonic data, the triplet  $(x, y, t)$  for each ion, is used to identify the ionic species (using their TOF) and to calculate the ion momentum vectors  $(p_x, p_y, p_z)$ . The derivation of the momentum vectors from their position and TOF information of the ions is discussed in the next section. A sample list mode data file is given in the table 2.1.

## 2.7 Building the ion momentum vectors

The momentum vectors of the ions are obtained from three independently measured quantities,  $(t, X, Y)$  in the experiment. The component of momentum along the spectrometer axis (defined by the unidirectional extraction fields),  $P_z$  is obtained from the observed TOF of the ion. The other two normal components are obtained from the  $(X, Y)$  position measurement.

The TOF of an ion having mass  $m$  and charge  $q$  depends upon the spectrometer parameters i.e. field strength and length of the components of the extraction region and its initial momentum along the spectrometer axis,  $P_z$ . Since spectrometer parameters do not vary in the experiment, their contribution in the TOF for the ions having same  $m/q$  will be equal. On the other hand, ions are not created with unique momentum because of the thermal spread of the parent gas ensemble and also because of the energy gained in the fragmentation processes. This cause the ions having  $P_z$  of different magnitude and thus the TOF of the ions differ from each other. However, the corresponding energies for thermal spread ( $\sim 0.01$  eV) of the parent gas ensemble and arising from the fragmentation ( $\sim 10$  eV) are much smaller than the energy the ion gains from the extraction field ( few hundred eV). As a result, the effect of the ion's initial momentum,  $P_z$  appear as a distribution in the TOF spectrum around the mean value, which correspond to the TOF of the ions having  $P_z=0$ .

The TOF,  $t$  of the ion of mass  $m$  and charge  $q$ , having initial momentum  $P_z$ , travelling across the single field extraction region which comprises an acceleration region of length  $s$ , field strength  $E_s$  and a drift region of length  $D$  can be written as-

$$t = t_s + t_D \quad (2.2)$$

$$= \frac{-P_z/m + \sqrt{(P_z/m)^2 + 2(qE_s/m)s}}{qE_s/m} + \frac{D}{\sqrt{(P_z/m)^2 + 2(qE_s/m)s}}$$

Following first order space focusing Wiley-McLaren condition [74] for single

field configuration, it will be discussed in section 2.8,  $2s = D$  and arranging few terms in the expression, the TOF can be rewritten as

$$t = \frac{-P_z/m + \sqrt{2/m(P_z^2/2m + qsE_s)}}{qE_s/m} + \frac{2s}{\sqrt{2/m(P_z^2/2m + qsE_s)}} \quad (2.3)$$

The expression in the square root in both the term compares the kinetic energy of the ion corresponding to its initial longitudinal momentum,  $P_z$  with the total kinetic energy the ion gains from the acceleration region. As mentioned before  $P_z^2/2m \ll qsE_s$  and thus can be ignored to a good approximation. Now  $t$  can be written as

$$t = \frac{-P_z}{qE_s} + 2\sqrt{\frac{m}{q} \frac{2s}{E_s}} \quad : P_z^2/2m \ll qsE_s \quad (2.4)$$

The second term in the expression is only dependent on the instrumental parameters and on mass and charge of the ion. Also it can be seen that  $t$  has become linear with  $P_z$ . The second term represents mean value of the TOF distribution,  $t_0$  : TOF of ions having zero  $P_z$ .

$$t_0 = 2\sqrt{\frac{m}{q} \frac{2s}{E_s}} \quad (2.5)$$

The longitudinal momentum component  $P_z$  is calculated from the expression

$$P_z = qE_s(t - t_0) \quad (2.6)$$

The transverse momentum components  $P_x$  and  $P_y$  are calculated from the position measurements.

$$P_x = m \times (x - x_0)/t \quad (2.7)$$

$$P_y = m \times (y - y_0)/t \quad (2.8)$$

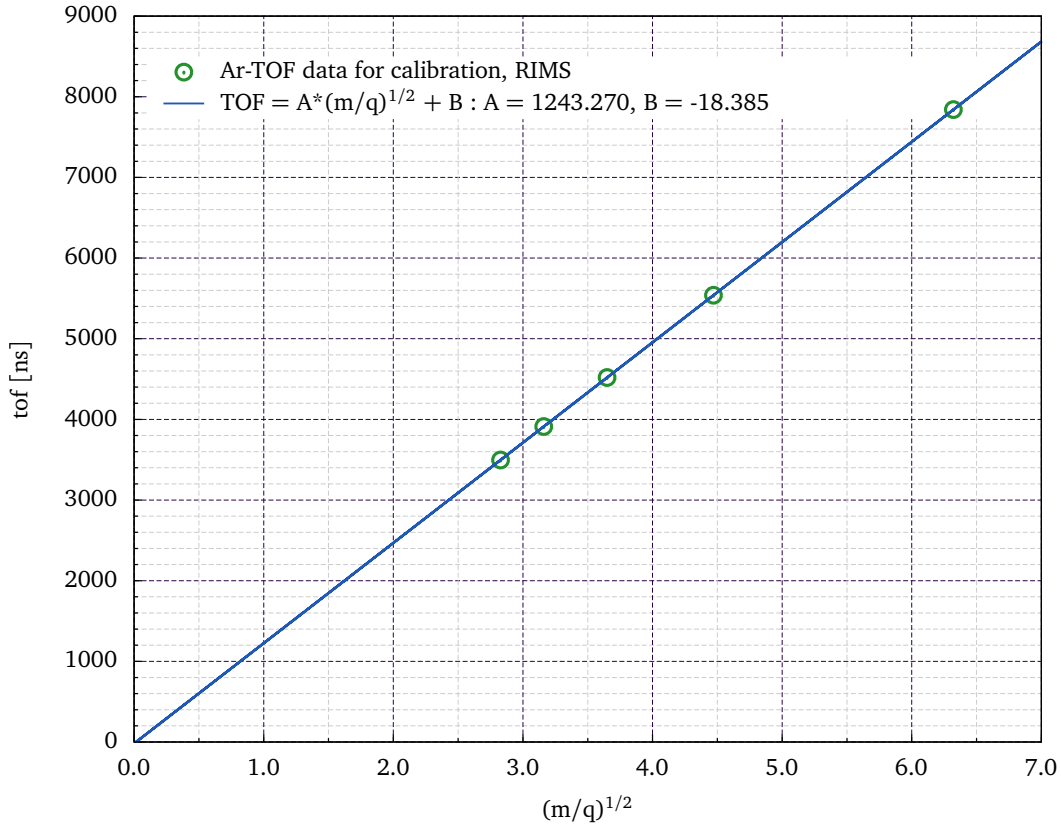


Figure 2.7: TOF calibration curve for RIMS obtained with Ar gas is shown. The observed five Ar ion species in a high energy electron impact (1.3 keV) experiment are linear-fitted with their  $\sqrt{m/q}$  values. The chi square value for the fit is 0.9999999. The value of slope and intercept are written in the figure label.

Equation (2.6), (2.7),(2.8) provide the complete momentum vector  $(P_x, P_y, P_z)$  of each detected ion.

It is important to mention that the observed mean TOF,  $t_0$  is used to identify the ionic species. The calibration curve between TOF and  $m/q$ , obtained with Ar gas is shown in the Figure 2.7. The observed five  $t_0$  corresponding to five ionic species of Ar are linear-fitted. The chi square value for the fit is 0.9999999, which shows the linearity of the TOF with  $\sqrt{m/q}$  and thus the precision and consistency of the spectrometer parameters in the experiment.

## 2.8 Resolution of the RIMS

The spatial and thermal spread of the molecular gas ensemble limits the resolution of the RIMS spectrometer. In order to get the better resolution, the first approach is to reduce these parameters as much as possible. In the experiment, we have used a very fine capillary to produce the molecular beam. Also we have employed effusive gas beam which produces adequately collimated beam maintaining the thermal equilibrium of the gas ensemble. Further, to minimise the effect of spatial spread on the TOF of ions, RIMS, which is a single field TOF spectrometer, is configured in the first order space focusing Wiley-McLaren condition that imposes a geometrical condition relating the length of the ion-extraction region,  $s$  and the length of the drift region,  $D$  ( $=2s$ ) [74]. For a single field TOF spectrometer, only one such condition is applicable. In order to achieve higher order focusing, double- triple-extraction fields are used. Further account on the focusing conditions for many field configurations can be found in [81, 82].

The first order space focusing Wiley-McLaren condition can be obtained by writing  $s$  in the Eq. (2.2) (taking  $P_z = 0$ ) as a sum of two components,  $s_0$  which represents the mean extraction field length and the variation,  $\delta s$  which represents the spatial spread. Since the spatial spread,  $\delta s$  ( $\sim 2\text{mm}$ ) is very small as compared to the extraction length  $s_0$  ( $=110\text{mm}$  in RIMS), terms involving  $s$  in the Eq. (2.2) can be expanded in the power of ratio  $\delta s/s_0$ . The Wiley-McLaren condition makes the first-order term, which is the largest term involving  $\delta s$  of the equation zero and thus reduces the effect of the spatial spread.

The effect of the employed focusing condition on the resolution can be realised by the fact that, in a single-field TOF spectrometer maintaining the  $s$  and  $\delta s$ , for  $s=D$ , which is not in accordance with focusing condition, the upper limit of the resolution will be just about 330, whereas in the focusing condition in which the second order term of  $\delta s/s_0$  will define the resolution, the limiting value will be about 9860.

We first obtain the momentum resolutions of the ion from the observed spatial and time resolution in the experiment. Momentum resolutions are used to

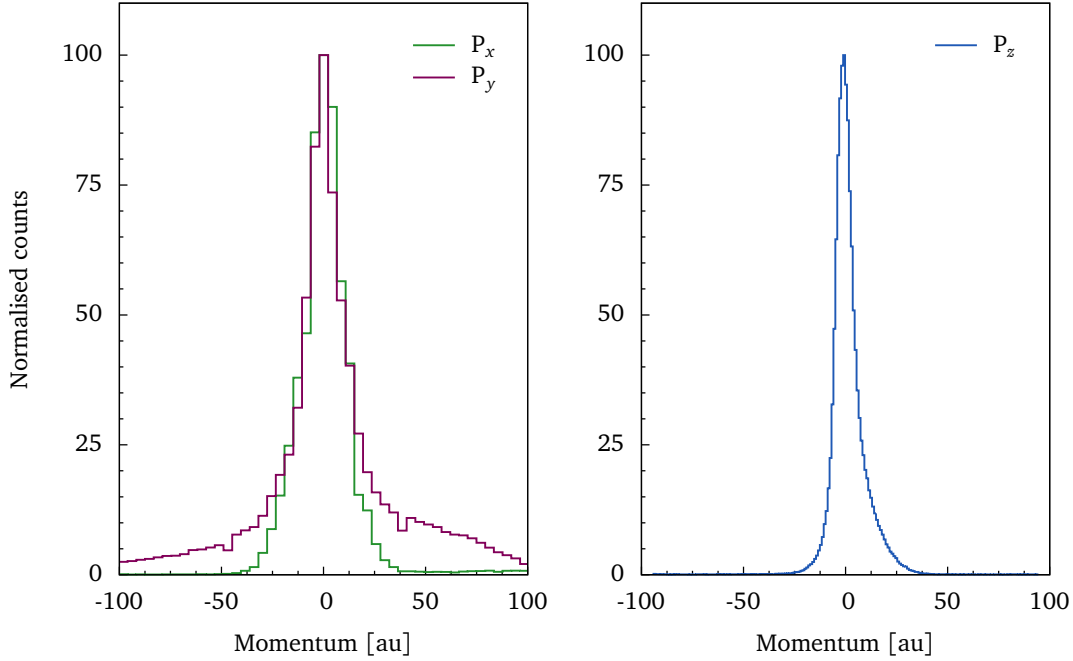


Figure 2.8: Transverse ( $P_z$ ) and longitudinal momentum distributions ( $P_x$  and  $P_y$ ) of Ar gas obtained with high energy electron impact is shown. The transverse momentum  $P_z$  is derived from the TOF of the ions and having the narrowest distribution among all the three momentum distributions. The longitudinal momentum components ( $P_x$  and  $P_y$ ) are derived from the position measurement and their wider distributions reflect the comparatively poor resolution in position. However, the difference between x- and y-components is due to the non-spherical interaction volume and spurious signals due to ionization of residual gas along the track of the projectile.

derive the energy and angular resolutions required for other kinematical properties. Resolutions corresponding to the three momentum vectors can be written as :

$$\Delta P_z = qE_s \Delta t, \Delta P_{x,y} = m \times \Delta x/t, m \times \Delta y/t \quad (2.9)$$

The limit on the momentum resolution of the ions are imposed by the time ( $\delta t = 1$  ns) and spatial resolution ( $\Delta x, \Delta y = 0.25$  mm) of the MCP and delay-line position sensitive detectors. For  $\text{Ar}^+$ , when  $E_s = 60$  V/cm, the limit of resolution turns out to be 2.1 a.u. for  $P_x, P_y$  and 0.3 a.u for  $P_z$ .

The actual momentum resolution, however depends upon the convolution of the initial spatial and thermal spread of the molecular gas beam and other experimental factors like non-uniformity of the field etc. To obtain the resolution

of the spectrometer, the observed TOF and position distributions are used. For this purpose, e-impact data of Argon gas (monoatomic, no contribution from the fragmentation) has been used. The Full Width Half Maximum (FWHM) values of the TOF and position distributions are used to calculate the momentum resolutions. The observed FWHM of (t,x,y),  $\Delta t = 21.8$  ns ,  $\Delta X = 5.1$  mm,  $\Delta Y = 5.4$  mm translate into momentum resolutions  $\Delta P_z = 10.3$  a.u.,  $\Delta P_x = 21.6$  a.u.,  $\Delta P_y = 22.8$  a.u respectively. The distributions for the components of momentum corresponding to the observed TOF and position distributions are shown in the Figure 2.8. The scalar momentum resolution for  $Ar^+$  is 33.0 a.u.. For any other ion of mass m, the momentum resolutions can be obtained by the equation:

$$\Delta P[m]_{x,y,z} = \Delta P[Ar]_{x,y,z} \times (m/Ar)^{1/2} \quad (2.10)$$

On the other hand, the energy resolution does not depend upon the mass of the ions. The kinetic energy resolution of an ion is calculated to be 200 meV. In case of fragmentation, the resolution will depend on the number of participating fragments. For instance, for the two body break up process, the resolution for the kinetic energy release spectrum will be 280 meV which is calculated by assuming the kinetic energies of the fragments as independent variables. Evidently, for higher order fragmentation the resolution will decrease further.



# Chapter 3

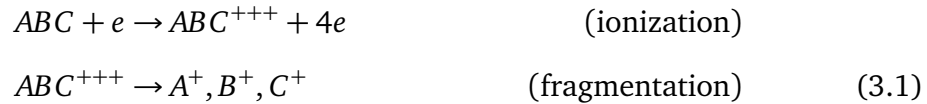
## Data Analysis

In the previous chapter, we have seen that the RIMS is capable of identifying the ions created in the collision events from their mean-TOF,  $t_0$  and concurrently accessing their momentum vectors from their measured TOF and position at the detector plane  $(t, X, Y)$ . In addition, multi-hit coincidence technique and collision conditions to achieve the correlated kinematics between the observed ions have also been discussed. In this chapter, derivation of the various kinematical properties of the fragmentation viz. Kinetic energy release, calculation of the life time, geometry of the transient molecular ion and angular dependence with projectile from the observed correlated kinematics between ions will be discussed. In the end of this chapter, various instrumental and statistical factors responsible for biased collection of the collision events that results in modified kinematical properties will be pointed out. In addition, the ways to achieve the accurate kinematics of the process will be discussed.

### 3.1 Identification of fragmentation pathways

The fragmentation pathways link the fragmented ions observed in coincidence with the parent transient molecular ion. More precisely, the parent transient molecular ions are discerned by looking at the fragmented ions observed in coincidence in experiments. For instance, for a triatomic molecular system ABC, the detection of

the three ions  $A^+$ ,  $B^+$  and  $C^+$  as three-Hits in a same coincidence time-window is considered as a collision event in which molecule ABC gets triply-ionized and then  $ABC^{+++}$  completely atomized resulting three ionic products. It can be written as follows :



There are other fragmentation channels, like shown in Eq. (3.1), which result only ionic products. In such cases all the ions observed in coincidence will cumulate the total atomic partners of the molecule and thus the fragmentation pathways can be easily asserted. Apart from the triple body fragmentation of  $ABC^{+++}$  shown in Eq. (3.1), there are other two body fragmentation channels in which both partners are ionic [  $(AB^{++}, C^+)$ ,  $(AB^+, C^{++})$  etc] belong in the same category. The complete kinematics of these channels are accessible as the kinematics of each fragmented partners can be measured in the experiment.

On the other hand, the fragmentation channels which involve neutral species, the observed ionic fragments will not add up to all the atomic partners of the molecule. In such cases, the identification of the fragmentation pathways is no more straightforward. For example, if  $(A^+, B^+)$  is observed as an event, it may be coming from the fragmentation of doubly-ionized ABC which results a neutral C as the other product. Also, it may be the case where the C ion has not been detected in the fragmentation of  $ABC^{+++}$ . These possibilities can be sorted out only by using additional means like by comparing the relative ionization cross sections of double and triple ionization and accounting the loss processes in the detection of ions and other statistical factors that might be responsible for suppression of the C ions.

However, for the channels which are identified to involve only one neutral partner, correlated kinematics between the observed ionic fragments can be used to achieve the full kinematics of the fragmentation employing momentum conservation rules. On the other hand, fragmentation channels involving more than one neutral fragments can not be studied kinematically. It will be discussed in the next

section that in few cases these possibilities can be pinned down by looking at the correlation maps of the events.

## 3.2 Coincidence maps

Identification of the fragmentation pathways can be affirmed by looking at the momentum correlations among the observed ions. The momentum of the fragmented ions that are produced from the same transient molecular ion would share a correlation following the momentum conservation rules. Momentum correlation maps are normally used for this purpose, are the two dimensional plots between the same momentum components of two fragmented ions. The effective way is to consider the time coincidences of the fragmented ions, which functionally identical to the correlation maps of their z-momentum components as the TOF of ions are linearly proportional to their z-momentum component. Since only the correlated ions would result in some pattern in the time coincidence maps and thus the presence of such pattern confirms the genuine coincidence events.

### 3.2.1 Nature of fragmentation

In addition to identifying the fragmentation channels by looking at the time coincidence maps, it has been found by Eland [83] that the nature of fragmentation can also be probed on the basis of the shape and structure of the islands in the coincidence maps. For the two body breakup, in the coincidence map of the Hit-1 (ion detected first) and Hit-2 (ion detected after the Hit-1), the ions in coincidence would appear as a linear strip. A schematic diagram is shown in the Figure 3.1. It is because for two body fragmentation, both partners acquire the same magnitude of momentum following the momentum balance for all the three components. Consequently the corresponding change in the TOF of ions occur in same proportion where the ratio of their charges appear as the slope of the island. It is useful in identifying the actual ionic species in cases where many having same  $m/q$  and thus equal mean TOF can be viable candidates. In the Figure 3.1, the ion pair making

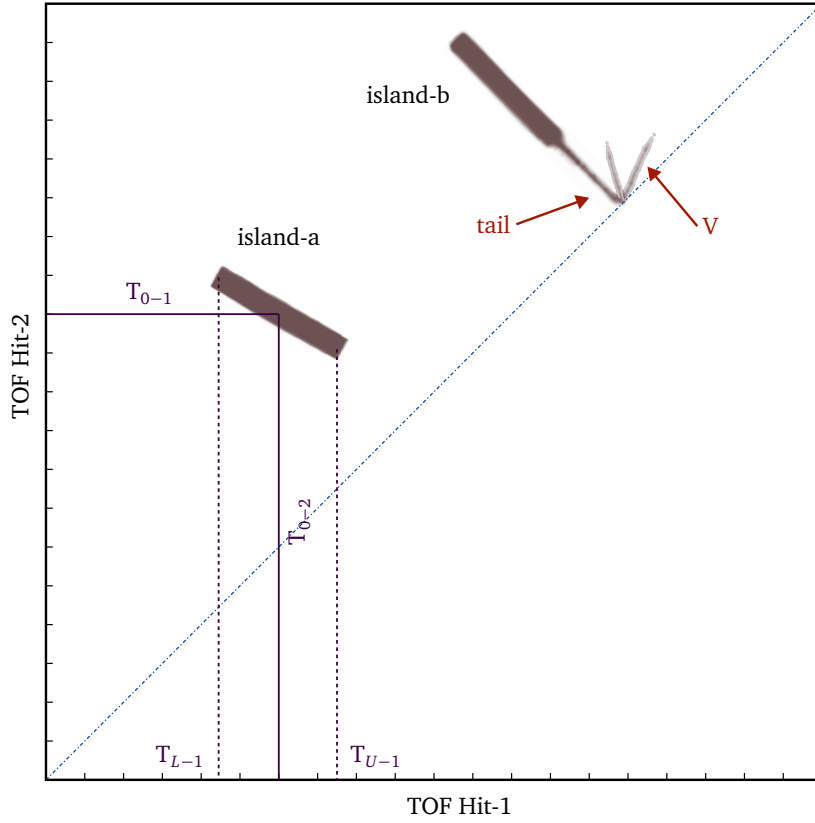


Figure 3.1: A schematic of time correlation map is shown. The two islands, island-a and island-b represent the two distinct pair coincidences. On the correlation map, the extent of the island shows the maximum kinetic energy release and the slope represents the relative charge states of the fragmented ions. The lower and upper extent of the TOF of Hit-1 in the island-a are shown by  $T_{L-1}$  and  $T_{U-1}$  respectively.  $T_{0-1}$  and  $T_{0-2}$  represent the mean TOF of the first and second Hit ions. The shape and features of the islands are used to reveal the various aspects of the fragmentation.

the island-b will have equal charges. Whereas, for island-a the ion appearing as the Hit1 would have smaller charge than its partner ion appearing as Hit2. The maximum acquired  $P_z$  in the process can be obtained from the extent of the island. It can be used to estimate the maximum kinetic energy released assuming equipartition between all the kinetic energy components in the fragmentation. The width of the strip represent the convoluted variance of the TOF of the fragmented ions.

For three body (or many body ) fragmentation, the process can be classified as concerted or sequential on the basis of the nature of fragmentation. In a concerted breakup all fragments are ejected simultaneously and thus the conservation of

momentum is described by a single equation relating all the fragments. Whereas in a sequential breakup, fragmentation takes place in steps and thus the order of fragmentation will decide the conservation rules relating the fragments in the momentum equations. The sequential process can be further classified for the channels involving one neutral fragment as initial charge separation (ICS) and deferred charge separation (DCS). ICS is the process where the neutral fragment produces in the last step, where as in DCS the neutral will release in the first step of fragmentation [84–86]. These classification was first made by Eland based on the observed shapes of the islands in time coincidence maps. For three body concerted break up, the islands are either dumbbell or cigar shaped distribution. For sequential breakups, the coincidence maps can be fitted with lines where their slope identifies their fragmentation pattern.

### 3.2.2 Mean life time of the transient molecular ion

Apart from the maximum kinematic energy released, the other important quantity which can be estimated from the observed time coincidence map is the mean life time of the transient molecular ion which has been observed for many molecular ions [87–89]. The characteristic distribution of the prompt fragmentation shows a single centroid which define the mean TOF,  $T_0$  of the fragmented ions in the correlation maps. Island-a in the Figure 3.1 is an example of the prompt dissociation. On the contrary metastable transient molecular ions will decay with some delay in their way to the detector in the extraction region and thus the TOF of the fragmented ions will alter from their mean TOF. Because of the metastability of the transient ion, the island corresponding to the prompt fragmentation grows a tail extending up to the diagonal in the coincidence map as shown in the Figure 3.1 for island-b. The tail is formed due to break up of the transient ion in the ion-acceleration region. If the transient molecular ions fragment in the ion-drift region, it forms a V-shape structure as shown in the schematic diagram. The mean life time  $\tau$  of the transient molecular ion can be estimated from the fractional counts in the tail and V-shape structure by using the following expression.

$$\frac{I_{tail}}{I_V} = f(\exp(T/2\tau)) \quad (3.2)$$

Where  $T$  is the TOF of stable transient molecular ion and  $f$  is the transmission factor of the spectrometer which is better than 90% in our case. Time correlation maps have been used to calculate the mean-life of transient molecular ions in few cases [89, 90]. In this work, though, we have not observed any metastability in the CSD breakup of dications of  $N_2$  and  $CO$ .

### 3.2.3 Analysis of the fragmentation channels

The time coincidence maps are used for the analysis of the fragmentation channels which involve more than one ionic fragments. The fact that the coincidence maps show only those events which have multiple ion-coincidences prevent the appearance of the ions that are recorded as single-coincidences (which often the most abundant outcome in the collision) on the coincidence maps. To analyse the fragmentation channels, first the sorting of the events from the recorded data is performed. This is done by defining the selection conditions on the TOF of ions. Since TOF of the ions have a distribution around their mean TOF value,  $T_0$ , the selection condition can be defined by two TOF values covering the mean. For instance, the conditions on the TOF for a  $T_n - T_m$  coincidence can be written as

$$T_n = T_{L-n} < T_{0-n} < T_{U-n} \quad \text{and} \quad T_m = T_{L-m} < T_{0-m} < T_{U-m} \quad (3.3)$$

Where,  $T_{0-n}$  and  $T_{0-m}$  are the mean  $T_0$  of  $n$ th and  $m$ th ions which are detected in coincidence.  $T_{L-n}$ ,  $T_{U-n}$  ( $T_{L-m}$ ,  $T_{U-m}$ ) define the lower and upper extent of the TOF of the  $n$ th ( $m$ th) fragment. The boundaries defined on the TOF of the ions are employed to sort the events of the selected channel from the list mode data. The mean TOF, mass and charge of the identified ions are then used to calculate  $(P_z, P_x, P_y)$  from the observed  $(t, X, Y)$  for the selected fragments.

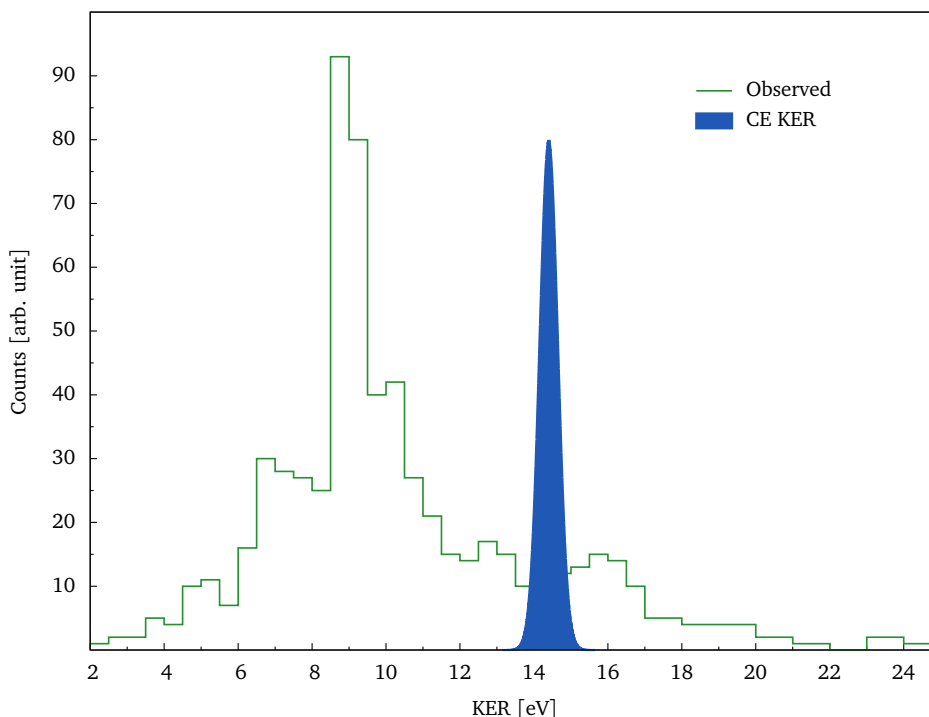


Figure 3.2: A schematic of observed KER spectrum is shown. A Coulomb explosion KER is also shown for comparison and to highlight the advantage of the complete kinematic measurement of the fragmented ions.

### 3.3 Fragmentation properties from the complete kinematics

More insight about the fragmentation process can be procured from the properties like Kinetic energy release, geometry of transient molecular ion and angular dependence of the fragmentation. Since these properties uses the complete kinematics of all the fragmented partners, their momentum and energy conservation establishes a link between the kinematics observed in the asymptotic limit with the kinematics at the time when fragmentation starts. This makes them very vital parameters in the study of molecular fragmentation because they provide the initial state of the transient molecular ions (deduced from the observed kinematics in the asymptotic limit) which is essential in order to understand the dynamical evolution of dissociation.

### 3.3.1 Kinetic Energy Release

When an unstable transient molecular ion is formed in a collision process, to minimise the total energy of the system, it starts dissociating and releasing the excess internal energy as the translational energy of the fragments. Kinetic Energy Release (KER) is the sum of the kinetic energies of all fragmented partners and thus it tells the energetics of the transient molecular ion when the fragmentation starts after ionization. It will be discussed in the next chapter how the knowledge of KER for a fragmentation event identifies the potential energy curve (PEC) on which the transient molecular ion is formed and evolved.

For two body breakup process,  $AB^{++} \rightarrow A^+, B^+$ , if  $P_A$  and  $P_B$  are the measured momentum of  $A^+$  and  $B^+$  respectively, the KER of this event can be written as

$$\text{KER} = \frac{P_A^2}{2m_A} + \frac{P_B^2}{2m_B} \quad (3.4)$$

In this case, the center of mass and laboratory frame momentum are taken identical. The estimated change in the KER for diatomic molecules ( $N_2$  or  $CO$ ) at room temperature is very small compared to their kinetic energy gain in the fragmentation.

In the Figure 3.2, a schematic of KER distribution observed from the complete kinematic measurement is compared with the Coulomb explosion KER for a given fragmentation channel. Before the advent of the momentum spectroscopy, in fact the mean KER was used to be estimated from the TOF coincidences [39] under Coulomb explosion (CE) model for fragmentation. CE model has been used to compare the observed KER in numerous cases [91–93]. However, mean KER value corresponding to the CE is a single value parameter for a fragmentation channel and does not offer any insight about the properties of the transient molecular ions. In the Figure 3.2, the centroid of the CE KER is shown at 14.4 eV which is the KER released in a fragmentation of two singly positive charged particles that were initially  $1.0 \text{ \AA}$  separated. The width of the CE KER peak represents the

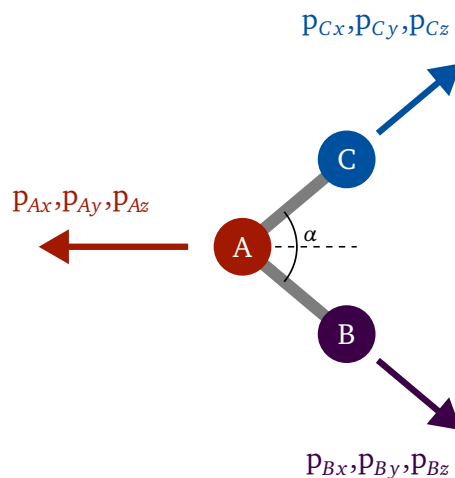


Figure 3.3: Derived geometry of a transient molecular ion is shown. The observed momentum of the fragmented ions are used to calculate the relative angular configuration of the transient molecular ion. Geometry of the transient system can be obtained by using the initial conditions (bond length information).

ground state probability distribution around the equilibrium bond length of the molecular system. KER distribution obtained from the complete momentum map shows the KER for each event separately and it thus represent the entire energetics of the fragmentation channel and thus is able to probe the properties of transient molecular ion and the nature of dynamical evolution in fragmentation can be explored with the help of theoretical modelling that will be discussed in the chapter 4. After realising the link of the KER with the electronic properties of transient molecular ions [94], experiments have been performed on many molecules to achieve the KER for their fragmentation channels with various projectile sources [47, 95–97].

### 3.3.2 Transient molecular ion geometry

Stable as well as unstable multiply charged molecular ions adjust themselves in order to achieve the minimal energy configurations that is normally different from the neutral parent molecule [98–101]. In many of these cases, more than one geometry configurations have been observed for a given fragmentation channel. The geometry of the transient molecular ion are estimated using the measured momentum of

the fragments under the assumption that after ionization the molecular ion first adopt the new conformation before the fragmentation starts. As a consequence of near equivalence between the laboratory and center of mass reference frames, the observed momentum of the ions can be taken as their center of mass momentum. If the measured momentum vectors of the ions  $A^+$  and  $B^+$  are  $P_A$  and  $P_B$  respectively, the relative angle between the fragment momentum vectors can be written as

$$\alpha_{A:B} = \cos^{-1} \left[ \frac{\vec{P}_A \cdot \vec{P}_B}{|P_A||P_B|} \right] \quad (3.5)$$

The above analysis for all the pairs of fragments will provide their relative angular momentum configuration. However, the bond angles of the transient molecular ion can be obtained from the derived relative angular momentum configuration by accounting Coulomb repulsion between the fragmented ions. The geometry of the transient molecular ion is defined using the derived bond angles and the initial condition of the fragmentation i.e. bond length information. A schematic diagram is given in the Figure 3.3, showing the estimated geometry of a tri-atomic molecular ion that was completely atomized resulting three fragments  $A^+$ ,  $B^+$ ,  $C^+$  of momentum  $P_A, P_B, P_C$  respectively.

### 3.3.3 Anisotropy measurement

Since RIMS is capable of covering the fragmentation events over the entire  $4\pi$  solid angle, as discussed in the section 2.3.1 also it measures all the three free momentum components separately that provide the momentum vectors for the ions, the angular distribution of the fragmented ions from the ionization point can be obtained. In general, the observed angular distribution of ions are isotropic. Since the initial orientation of the molecules before the interaction with projectile is kept random, the isotropic distribution suggests that there is no angular dependence (with some reference axis defined by the projectile) in ionization and fragmentation. On the other hand, anisotropic distribution of the fragmented ions is a signature

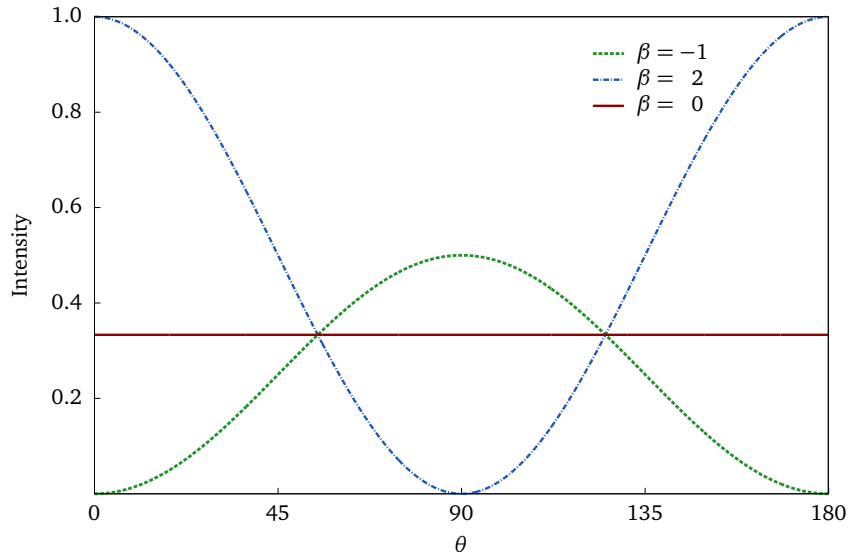


Figure 3.4: Asymmetry parameter  $\beta$  is plotted for three values; 0,-1,2.  $\beta = 0$  has no  $\theta$  dependence and represents the isotropic distribution. Whereas,  $\beta = -1$  and 2 represent the two modes (perpendicular and parallel) of distribution. Any observed distribution of the fragmented ions fall within  $\beta = -1$  and  $\beta = 2$ .

of the angular dependence of the interaction Hamiltonian with projectile. The normalised angular distribution can be represented by the equation

$$I(\theta) = 1/4\pi[1 + \beta P_2(\cos\theta)] \quad (3.6)$$

Where  $\theta$  is the angle between fragmented ion and the axis defined by the projectile (the projectile axis in case of charged ions and polarization vector in case of photons).  $P_2(\cos\theta)$  is the second Legendre polynomial and  $\beta$  is a parameter that represent degree of anisotropy ( $-1 \leq \beta \leq 2$ ). For isotropic distribution  $\beta$  is zero. Whereas,  $\beta = -1$  and 2 represent the two different (perpendicular and parallel) modes of distribution. The  $\beta$  value calculated from the observed distribution falls within these limiting values. The intensity variation as a function of the  $\theta$  for the three values of  $\beta$ , 0,-1, 2 are shown in the Figure 3.4. An account of the measurement of anisotropy can be found in [62]. The angular dependence of the fragmentation has been extensively studied for many molecules with various projectile sources in the past and has been established as an important aspect of

the study [102–107].

### 3.3.4 Branching ratios of the fragmentation channels

Apart from the analysis of the separate fragmentation channels, the relative branching ratios of different channels are another important parameter. The branching ratios of the fragmentation channels can be estimated from the time-coincidence maps. However, the raw counts observed in the coincidence maps needs to be corrected for detector efficiencies and ion losses, that will be discussed in the next section, to achieve the accurate branching ratios. Since the total ionization cross section has been well estimated for many molecules with various projectiles over a wide span of energy [108], it is possible now to investigate how these cross sections further subdivide for the different fragmentation channels in the course of dissociation. It is a very crucial aspect of the fragmentation as it helps to recognise the preferred pathways of the fragmentation for a given transient molecular ion. In this thesis, there is an attempt to understand the processes that decides the branching ratios for CSD break up of  $N_2$  and CO. It will be discussed in full length in the chapter 5.

## 3.4 Corrections in the measured kinematics

In ion momentum spectrometer, the detection of an ion depends upon many instrumental factors and ion specific parameters. It is essential to consider and estimate the effects of these factors on the ion detection probability. In the case, when the detection probability does not depend upon the energetics of the ions, the corrections are rather simple and affect only the relative cross sections and branching ratios of the collision products. The detector efficiency and the transmission efficiencies of meshes used in the extraction region are such factors and has been studied and taken care of in cross section measurements. These aspects are discussed in the section 3.4.3 and 3.4.4.

However, when the transmission and detection probabilities depend on the

energy of the ions, all the kinematical parameters like KER, angular dependence etc will be modified. In order to obtain the accurate kinematical information of the fragmentation, it is essential to quantify these probabilities and make corrections to the observed kinematics. One such factor arises because of the finite size of the ion-detector that imposes an upper limit on the ion's energy beyond which the transmission of ions depends upon their energetics. In the analysis of CSD channels of  $N_2$  and CO, the transmission loss has been taken in to account and it turns out to be a significant factor. The transmission loss has been discussed in detail in the section 3.4.1. The other factor which depends upon the energetics of the ions is the loss due to dead time of the detectors. It is also taken into consideration and discussed in the section 3.4.2.

At this point, it is important to mention one more crucial aspect about the detection efficiencies. Because of the probabilistic nature of the detection, if the detection probability for an ion is  $p$  ( $< 1$ ), then the double- and triple- ion coincidence probabilities will be  $p^2$  and  $p^3$  respectively and so on. As a result the likelihood to observe a higher order coincidence is always smaller than one of the lower order. For this reason, apart from the modifications made by their coincidence probabilities, the observed cross sections of a fragmentation channel will be further modified because of the inclusion of the events from higher-order coincidences that are detected being as lower-order coincidence events.

### 3.4.1 Ion transmission losses

The finite size of the ion-detector imposes an upper limit on the kinetic energy for complete transmission of ions formed in the ionization region. The transmission loss turns out to be an energy dependent function and thus the corresponding error in the observed quantities increases with the energy. The transmission loss for isotropic and non-isotropic distribution of ions created in the ionization region is derived in the Appendix A. In the fragmentation process the energy gained by a fragmented partner depends upon the relative masses of all partners, geometry of transient molecular ion and nature of the break up pattern. Since the mentioned

properties of the transient molecular ion and fragmentation are not identical for all cases, the observed kinematics of the fragmentation channels get distorted differently.

For two body break up process  $AB \rightarrow A + B$  ( $m_A \leq m_B$ ), with  $KER = \epsilon_A + \epsilon_B$ , the conservation of linear momentum ( $\epsilon_A \times m_A = \epsilon_B \times m_B$ ) implies that the lighter fragment will always have larger kinetic energy. Consequently the loss factor will be effectively determined by the loss of lighter fragment and the limiting value of the kinetic energy up to which there is complete collection will be given by

$$KER_{lim} = \epsilon_{Allim} \times (1 + m_A/m_B) \quad (3.7)$$

Where  $\epsilon_{Allim}$  is the limiting value of kinetic energy up to which there is no transmission loss. It only depends upon the experimental parameters and thus same for all ions having same charge. Using the loss factor for an ion for isotropic distribution, derived in the Appendix A, the loss factor in terms of KER for two-body fragmentation can be written as

$$LF(KER) = [1 - KER_{lim}/KER]^{1/2} \quad (3.8)$$

Since in a two-body breakup the kinetic energies of the partners are in inverse proportion of their masses and the loss factor for an ion is a function of its kinetic energy, but independent of its mass, the loss factors at given KER will in general be different for the two fragments. This characteristic affects the measured energy-differential and partial cross-sections as well as the branching ratios. More importantly, corresponding to a given loss energy, the loss angle for the lighter species is always larger than for the heavier one, many pair coincidences will be recorded as singles in two-body fragmentation. For many-body fragmentation having additional complications, multiple fragmentation events will be recorded as a lower order events than they truly are. This means that in most cases the measured branching ratio for multiple ion fragmentation will be incorrect.

However, for a pair breakup a reasonable correction can be applied. The limiting KE value  $\epsilon_{lim}$  for complete transmission can be obtained analytically or by a particle

trajectory simulation for the given spectrometer configuration. Thus the loss factor for that ion as well as for the fragmentation channel can be well accounted and the correction to the partial cross-section for that species can be readily made.

In the RIMS operated at 60 V/cm extraction field, the limiting value of the kinetic energy for a singly ionized ion is 4.85 eV, (estimated in the Appendix A). The transmission loss in the CSD break up of dications of N<sub>2</sub> and CO will start at KER value 9.70 eV and 8.48 eV respectively that can be calculated using Eq. (3.7). The observed and loss corrected spectra for the CSD break up of N<sub>2</sub><sup>++</sup> are shown in the Figure 3.5. The total cross section after accounting the transmission loss increases by 30%.

For three-body (in general, many-body) fragmentation, momentum sharing between fragments depends on the geometry of the transient molecular ion and the nature of the fragmentation pattern. Since the loss factor for fragmentation channels is decided by the fragment which gain maximum energy in the break up (that can not be identified without the knowledge of properties of transient molecular ion), the loss factor can not be generalised as in case of two-body fragmentation. However, if the transient molecular geometry and the nature of fragmentation is known, it is possible to estimate the loss factors for many body fragmentation.

It can be noted that in case of transmission loss, for the ions having kinetic energy larger than the limiting value  $\epsilon_{Allim}$ , the collection of ions has an angular dependence. This angular dependence is an artifact and its share can not be separated from the angular distribution caused by anisotropic fragmentation. As a result, if there are losses in transmission, the value of  $\beta$ , which is the measure of anisotropy always give the inaccurate conclusion about the nature of interaction. This point has been addressed by Pandey *et. al* [109].

### 3.4.2 Effect of dead time of the detectors in ion-coincidence

Another loss factor which affects the kinematics of the fragmentation channels comes in due to the deadtime ( $t_d$ ) of the detector and the signal processing

electronics. If the two ions in a breakup have nearly equal flight times, then they may not be detected as separate particles, thereby reducing the apparent (observed) yield for that channel. The problem is particularly important when the two ions have the same  $m/q$  ratio. The general expression for TOF of an ion can be written as (similar to the Eq. (2.4) section 2.7)

$$t = a \left( \frac{m}{q} \right)^{1/2} - \frac{P_{\parallel}}{qE_s} \quad (3.9)$$

where  $E_s$  is the field strength in the extraction region and  $a$  is related to other spectrometer parameters. Since two identical ions (such as  $N^+$ ,  $N^+$  from the breakup of  $N_2^{2+}$ ) will always have the same magnitude of the momentum, they will be detected as separate only when their parallel components of momentum satisfy the condition  $(2P_{\parallel}/qE_s) > t_d$ . This means that for any value of KER in a two-body breakup, there will be a loss of detected ion pair coincidences. From this relationship, we find that for isotropic emission the loss fraction due to deadtime reduces with energy,  $\epsilon$  of the ions and being sampled as  $t_d q E_s / \sqrt{8m\epsilon}$ . A discussion on the loss because of the deadtime can be found in Ali *et. al.* [79].

In RIMS, operating at  $60 \text{ V cm}^{-1}$  extraction field and having a 20 ns estimated deadtime of the detection system, the loss due to deadtime of detection for the  $N^+$ ,  $N^+$  pair is calculated to be  $0.155/\sqrt{KER}$ .

In order to highlight the effect of the two losses that affects the kinematics of the fragmentation channels, namely the transmission loss and dead time loss, the KER spectrum of fragmentation of  $N_2^{++}$  into  $N^+, N^+$  is shown in the Figure 3.5. The observed KER spectrum from the RIMS setup is shown by dots. The KER spectrum is plotted with 300 meV bin size, which represents the energy resolution for the two-body breakup. The loss corrected KER is shown by vertical lines. Loss because of finite detector size starts from 9.70 eV in this case and increases with KER as discussed in the section 3.4.1, whereas loss because of the dead time is significant only in the lower KER range. The function of loss factors due to incomplete transmission and finite deadtime are also shown Figure 3.5 in the inset. It is very interesting to note that a peak appears at 10.5 eV in the corrected spectrum, which

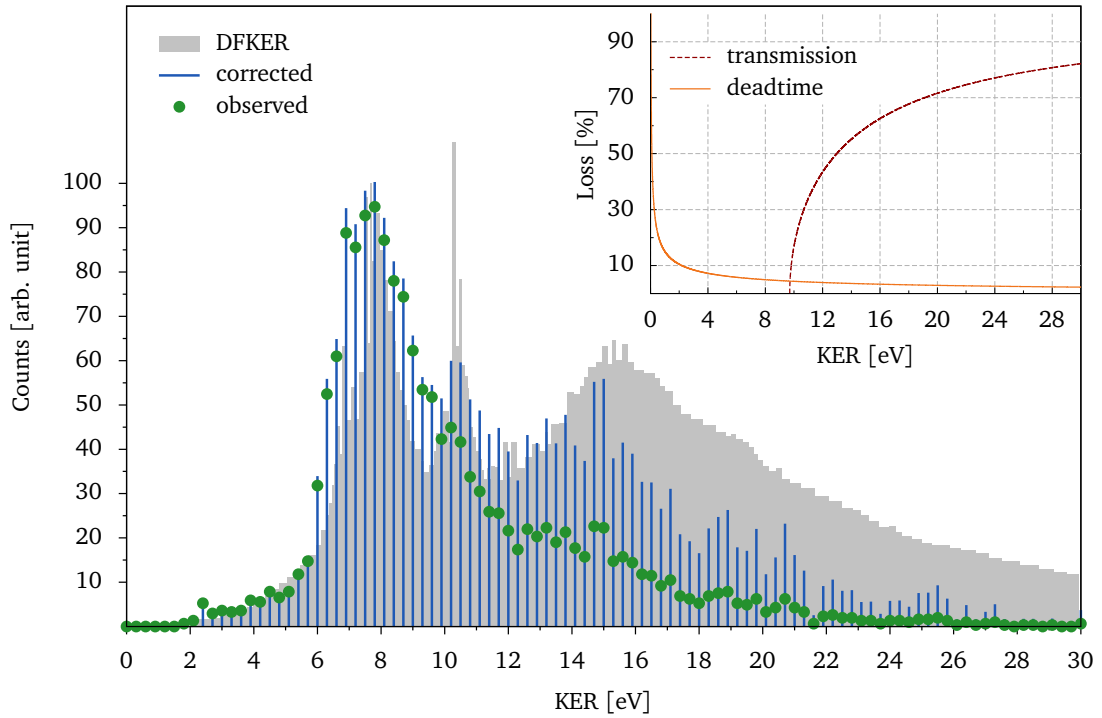


Figure 3.5: KER distribution for the fragmentation channel  $N_2^{++} \rightarrow N^+:N^+$  is shown. The observed KER from RIMS setup [72], operated in the condition described in the text, is shown by dots. The KER distribution corrected for the transmission loss and dead time loss is shown by vertical lines. Up to 9.70 eV, transmission loss because of finite detector size is zero, however the dead time loss decreases with KER and thus effective for the lower KER range. Loss factors due to incomplete transmission and finite deadtime are shown in the inset. Our spectrum is compared with the Doppler-free measurement of the KER distribution (DFKER) by Lundqvist *et al.* under 200 eV electron impact [47] (Reproduced with permission from Institute of Physics Publishing Limited)

was very weak in the raw spectrum. This is because the loss factor is a very rapid function of the KER initially. As shown in the Figure A.2, for an increase in KER by 50% above  $KER_{lim}$ , loss increases by 60 %. The peak at 10.5 eV has been observed in experiments in which transmission losses are negligible. One such spectrum, DFKER spectrum reported by Lundqvist *et al.*, is shown in the Figure 3.5 [47]. There is one more broad structure in the KER spectrum at 15 eV, which becomes prominent after applying the corrections. This analysis clearly shows the importance of loss corrections in obtaining an accurate KER distribution.

### 3.4.3 MCP detection efficiency

The upper limit of the detection efficiency of a MCP is defined by a geometrical parameter called open area ratio (OAR) which is the ratio of active area of all micro channels with the total face area of the MCP. For ion-MCP used in the RIMS, it is 0.6. The detection efficiency of the MCP also depend upon the charge state and mass of the detected ions, angle of incidence, bias voltage and physical parameters of MCP like micro channel length and diameter, bias angle and material properties [110]. From the experiments that have been performed to measure the MCP detection efficiency, it can be learned that the maximum average efficiency is about 0.5 [111, 112]. In case where absolute cross sections are determined or the branching ratios of the fragmentation channels are compared, the MCP detection efficiency probably the most influencing factor to obtain the accurate results from the observed data. For instance, the detection efficiency of MCP operated in saturation (or near saturation) gain voltage is about 0.5. As a result, the pair-coincidence events will be twice as much suppressed than the events of single coincidence and so on.

In this work, in estimation of the branching ratios of CSD with non dissociated dications of  $N_2$  and CO, the MCP detection efficiency, operated at  $-2800$  V, of each ion is considered to calculate the accurate cross sections.

### 3.4.4 Effect of transmission meshes

In the RIMS, transmission meshes are used to create homogeneous field in the extraction region ( see section 2.4). Because of their finite opaque area they inevitably affect the transmission of the particles. As a result, it affects the collision events depending upon the number of products (ions and electrons) that are being created [113]. In the RIMS, three very high transmission coefficient meshes are used, two in the ion extraction region and one before the e-MCP. For an event in which one ion and one electron is created (single ionization), the transmission probability would be  $p^3$ , where  $p$  ( $=0.95$ , for RIMS) represents the transmission probability of a single mesh. For an event producing one ion and two electron,

(double ionization) the transmission probability will be  $(2 - p)p^3$ . On the other hand, for events in which two electrons and two ions are created, (double ionization and fragmentation) the probability will be  $(2 - p)p^5$ . This shows that how the cross sections of different ionization and fragmentation channels are modified differently. However, since  $p$  is very large, the difference in the transmission probability is about 10 % for double ionization channels without fragmentation and with two-body fragmentation.

This chapter summarizes the calculation of the various kinematical properties from the recorded time of flight and position data set of the fragmented ions. Further, the ways to correct the kinematical parameters from the various detection inefficiencies and losses are reviewed. The account of the various corrections in order to achieve the accurate cross sections and KER in case of the dissociative ionization of the dications of  $N_2$  and CO will be seen in the chapter 5.



# Chapter 4

## Theory

The dynamical evolution of the unstable molecular systems involve the interaction of its constituent electrons and nuclei that can not be approximated by rudimentary models like coulomb explosion. The observed kinematical properties of dissociative ionization need comprehensive knowledge of the electronic structure of the involved molecular systems. On the other hand, calculation of the electronic structure properties of the molecular systems is not an easy task and need a systematic theoretical formulation. Because of the complexity of the problem, assumptions and approximations are employed. In the first part of this chapter, section 4.1, the basic formulation of the electronic structure of the molecular system is discussed. Also, the set of approximations that are used in the calculation as well as their consequences on the kinematical behaviour of the molecular system are reviewed. In the next section 4.2, the effect of the perturbation causing the electronic excitations is discussed. In the same section a discussion is provided on the various processes of dissociative ionization. Also, the link between the observed kinematics and the predictions of the theoretical calculation is established. The discussion on these processes are presented to explain the dissociative ionization of dications of  $N_2$  and CO. In the last section 4.3, a discussion on the theoretical methods, used in the calculation of molecular properties is provided.

## 4.1 The molecular system

In the context of ab initio theories, a molecular system can be viewed as a quantum mechanical system constituting  $M$  nuclei and  $N$  electrons interacting via Coulomb forces

$$\{Z_1, Z_2, Z_3 \dots Z_M, e_1, e_2, e_3 \dots e_N\} \quad (4.1)$$

Where  $Z$ 's represent nuclei and identify their charges and masses,  $e$ 's represent the electrons. In the ab initio theory, only the fundamental properties of particles are incorporated in the calculation of the system's properties. In the equation 4.1, sum of nuclei positive charges ( $\sum_{A=1}^M Z_A \times e$ ) and the negative charges because of electrons ( $\sum_{i=1}^N (-e) = -N \times e$ ) define the charge state of the molecular system. For a neutral molecule, the total sum of the charges would be zero.

The complete interaction between nuclei and electrons and their kinetic energies in a molecular system can be expressed by Hamiltonian,  $\hat{H}$ , written in eq 4.2. The eigen solutions of the Schrödinger equation for the molecular Hamiltonian provide the associated eigen wavefunctions, eq 4.3, which are used to derive the observable properties of the molecular system.

$$\begin{aligned} \hat{H} &= - \sum_{i=1}^N \frac{1}{2} \nabla_i^2 - \sum_{A=1}^M \frac{1}{2M_A} \nabla_A^2 \\ &\quad - \sum_{i=1}^N \sum_{A=1}^M \frac{Z_A}{r_{iA}} + \sum_{i=1}^N \sum_{j>i}^N \frac{1}{r_{ij}} + \sum_{A=1}^M \sum_{B>A}^M \frac{Z_A Z_B}{R_{AB}} \\ &= \hat{T}_N(\mathbf{R}) + \hat{T}_e(\mathbf{r}) + \hat{V}_{eN}(\mathbf{r}, \mathbf{R}) + \hat{V}_{ee}(\mathbf{r}) + \hat{V}_{NN}(\mathbf{R}) \end{aligned} \quad (4.2)$$

$$\hat{H}\Phi_n = E_n \Phi_n \quad n = 1, \dots, \infty \quad (4.3)$$

In the equation 4.2,  $R_{A/B}$  ( $A/B=1, 2, \dots, M$ ) and  $r_{i/j}$  ( $i/j=1, 2, \dots, N$ ) represent the coordinates of  $A/B$ <sup>th</sup> nuclei and  $i/j$ <sup>th</sup> electron. The distance between  $i$ <sup>th</sup>

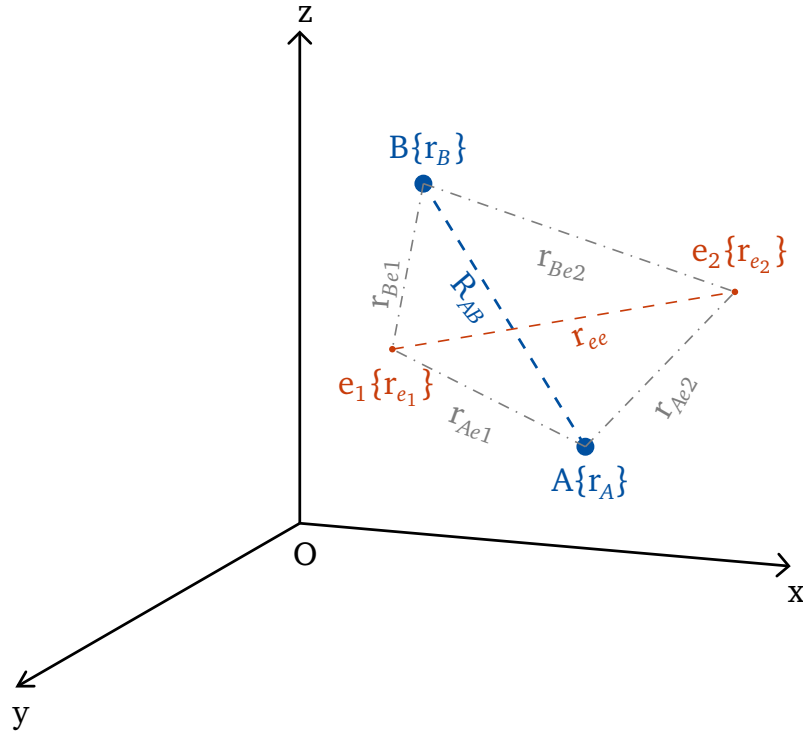


Figure 4.1: A schematic representation of the molecular coordinates is shown. A, B represent the nuclei and  $e_1, e_2$  are the electrons. Their coordinates with respect to the origin O is written in the associated curly brackets. The distance between these charge particles are shown explicitly to highlight their  $1/r$  Coulombic nature of the interaction.

electron and A<sup>th</sup> nuclei is  $r_{iA}$ . Similarly,  $r_{ij}$  and  $R_{AB}$  represent the distances between  $i^{\text{th}}$  -  $j^{\text{th}}$  electrons and A<sup>th</sup> - B<sup>th</sup> nuclei respectively.

The first two terms,  $\hat{T}_N(\mathbf{R})$  and  $\hat{T}_e(\mathbf{r})$ , involving the Laplacian operators  $\nabla_A^2$  and  $\nabla_i^2$  are the kinetic energy operators of M nuclei and N electrons respectively. The third term,  $\hat{V}_{eN}(\mathbf{r}, \mathbf{R})$ , constitutes the sum of all Coulomb attraction between nuclei and electrons of the system. The fourth and fifth terms,  $\hat{V}_{ee}(\mathbf{r})$  and  $\hat{V}_{NN}(\mathbf{R})$ , account the total Coulomb repulsion between electrons and nuclei respectively.

The terms of the equation 4.2 are written in atomic units. An account on atomic units can be found in [23]. In the equation,  $M_A$  represents the ratio of mass of nucleus A to the mass of an electron and  $Z_A$  stands for the atomic number of nucleus A.

The above equation defines a non-relativistic time independent Hamiltonian

operator. In this thesis only small molecules constituting low  $Z$ - atoms are considered. In addition, the properties of molecules that are central to this thesis do not involve core electrons only for them the relativistic corrections are significant. For this reason the non-relativistic theory is considered. Further, the Hamiltonian  $H$  in eq 4.2 does not consist any term involving electron or nuclear spin and thus its solution does not explicitly deal with any spin dependent energy terms, like spin-orbit coupling term. However, the spin of the particles are taken into account in defining the wave function of the molecular system. The energy corrections because of relativistic effect and spin-orbit coupling are very small as compared to the Bohr energy ( $\alpha^2$  times smaller, where  $\alpha \cong 1/(137.036)$  is the fine structure constant) and thus are neglected in the discussion of dissociative ionization. The relevant energy scale for dissociation of molecules, few 100 meV: vibrational energy scale, is about 100 times bigger than the fine structure corrections.

#### 4.1.1 Separation of nuclear and electronic motions

The solution of eq 4.3 provides the energy eigen functions and values of the molecular system. However, the relative dynamical time scales of the electrons and nuclei are significantly different. In the molecular Coulomb field that is written as sum of three terms,  $V_{eN}$ ,  $V_{ee}$  and  $V_{NN}$ , nuclei move much slower than the electrons because of the large differences in their masses. As a result, electrons in a molecular system can be regarded as particles that follow the nuclear motion adiabatically. These inherent nature of the particles of a molecular system allows to separate the nuclei and electronic motions. Consequently, at any point of time, because of adiabatic behaviour of the motion of electrons in the molecular system, the electronic properties will be completely determined by the present nuclear conformation. On the other hand, the same reason makes the nuclei to move in the average potential created by the electrons. These inherent differences in the dynamics of electrons and nuclei in the molecular system makes the basis of Born-Oppenheimer approximation [8].

Under BO approximation, the molecular Hamiltonian, eq 4.2 can be divided in

two parts commonly known as electronic Hamiltonian,  $H_{elec}$  and nuclei Hamiltonian  $H_{nucl}$ . The electronic Hamiltonian  $H_{elec}$  can be written as

$$\hat{H}_{elec} = \hat{T}_e(\mathbf{r}) + \hat{V}_{eN}(\mathbf{r}, \mathbf{R}) + \hat{V}_{ee}(\mathbf{r}) \quad (4.4)$$

The Schrödinger equation for  $H_{elec}$  provides the eigen wave function,  $\Phi_{elec}(\mathbf{r}, \mathbf{R})$ , and values,  $E_{elec}(\mathbf{R})$ , of electronic part of the molecular system.

$$\hat{H}_{elec} \Phi_{elec}(\mathbf{r}, \mathbf{R}) = E_{elec}(\mathbf{R}) \Phi_{elec}(\mathbf{r}, \mathbf{R}) \quad (4.5)$$

In the eq 4.5  $\Phi_{elec}(\mathbf{r}, \mathbf{R})$  that describes the motion of the electrons explicitly depends upon the electronic coordinates but also depends parametrically on the nuclear coordinates. The nuclear coordinates do not appear explicitly in the  $\Phi_{elec}$  however, for different nuclear conformation the  $\Phi_{elec}$  varies.

In explaining the nuclei motion, BO approximation ignores the coupling terms between different electronic states for a given nuclei conformation in the nuclei Hamiltonian. This is called adiabatic approximation and is justifiable for the cases where the electronic states are widely separated. On the other hand, for the cases where the energy separation of electronic states is not large (cases of degenerate and near-degenerate states), the non-BO dynamics may be observed [114]. BO approximation also ignores average kinetic energy and velocity terms of the nuclei calculated in the electronic wave functions basis that involves nuclei masses. This creates a picture of infinitely heavy nucleus and also makes the potential function independent of the masses of nuclei. After ignoring these terms, the nuclei Hamiltonian can be written as

$$\hat{H}_{nucl} = \hat{T}_N(\mathbf{R}) + E_{elec}(\mathbf{R}) + \hat{V}_{NN}(\mathbf{R}) \quad (4.6)$$

and the Schrödinger equation for nuclei will be

$$\hat{H}_{nucl} \Phi_{nucl}(\mathbf{R}) = E \Phi_{nucl}(\mathbf{R}) \quad (4.7)$$

In the equation 4.6, it can be noted that the sum of  $E_{elec}(\mathbf{R})$  and  $\hat{V}_{NN}(\mathbf{R})$  acts as a potential energy for the nuclei and when expressed as a function of nuclei coordinates  $\mathbf{R}$  it is termed as Potential Energy Curves/Surfaces on which the motion of nuclei occur. In equation 4.7,  $\Phi_{nucl}(\mathbf{R})$  depends only upon the nuclei coordinates and  $E$  denotes the total energy of the molecular system under BO approximation that includes electronic, vibrational, rotational and translational energy. The further division of nuclei Hamiltonian to separate the vibrational, rotational and translational energies requires the construction of Eckart vectors and Eckart frames [115]. However, for diatomic molecules, which is of concern in this thesis, the separation can be achieved in rather straight forward way. In order to calculate the vibrational structure for a given potential energy curve of a diatomic molecule, the Shrödinger equation is

$$\left[-\frac{1}{2\mu}\nabla^2 + U(\mathbf{R})\right]\xi(\mathbf{R}) = E_v \xi(\mathbf{R}) \quad (4.8)$$

In this equation, the first term is the kinetic energy of the particle of reduced mass  $\mu$  ( $= M_A M_B / (M_A + M_B)$ ), and the second term represents the potential energy function.  $\xi(\mathbf{R})$  and  $E_v$  represent the vibrational wavefunction and energy respectively. The rotational levels associated with vibrational levels can be calculated by solving the Hamiltonian equation 4.8 with an additional term  $J(J+1)/2\mu R^2$ .

Neglecting the kinetic energy terms of nuclei under the BO approximation in describing the nuclei Hamiltonian introduces very small error in the energy terms. The diagonal Born-Oppenheimer correction (DBOC)

$$\Delta E_{DBOC} = \sum_{a=1}^M -\frac{1}{2M_a} \langle \Phi_{elec} | \nabla_a^2 | \Phi_{elec} \rangle \quad (4.9)$$

turns out to be of the order of sub meV for the light nuclei and thus can be safely neglected [116]. However, the non-BO dynamics resulting from the coupling of PECs can be responsible for very significant changes in the results.

### 4.1.2 Electronic structure properties

The electronic properties of a molecular system is obtained by solving the  $H_{elec}$  given in eq 4.4. Under BO approximation, the electronic part of the molecular system can be viewed as a system of  $N$ - electrons in a Coulomb field created by the 'clamped nuclei'. The motion of each electron is also governed by the Coulomb interaction with nuclei and other electrons in the system. The wavefunction of  $N$ -electrons is represented in terms of  $N$ -single electron states. These single electron states are known as spin-orbitals  $\chi(x)$  and can be written as

$$\chi_i(\mathbf{x}) = \phi_i(\mathbf{r})\zeta(\omega) \quad (i = 1, \dots, n) \quad (4.10)$$

In the eq 4.10,  $\phi_i(\mathbf{r})$  represents the spatial orbital of an electron in the  $i$ th state and  $\zeta(\omega)$  represents its spin eigen state. For electron which is a spin half particle,  $\zeta(\omega)$  have two eigen states namely 'spin up',  $|\alpha\rangle$  and 'spin down',  $|\beta\rangle$ . Where as,  $\phi_i(r)$  space would ideally form a complete set, which in turn also means  $n \rightarrow \infty$ , to describe the motion of electrons in the molecules precisely. Both spatial and spin orbital spaces are constructed orthonormal that also make the spin-orbital basis an orthonormal basis set.

$$\langle \chi_i(\mathbf{x}) | \chi_j(\mathbf{x}) \rangle = \delta_{ij} \quad (i/j = 1, \dots, n) \quad (4.11)$$

The indistinguishability and antisymmetric properties of the electrons are taken into account in defining the  $N$ -electron wavefunction,  $\Phi_{elec}(\mathbf{r}, \mathbf{R})$  of  $H_{elec}$ . It is normally expressed in terms of Slater determinant and can be compactly written as

$$\Phi_{elec}(\mathbf{r}, \mathbf{R}) = \frac{1}{\sqrt{N!}} \left[ \sum_p (-1)^p \hat{\mathbf{P}} | \chi_1 \chi_2 \dots \chi_N \rangle \right] \quad (4.12)$$

where  $\hat{\mathbf{P}}$  represents the permutation operator.

It is important to mention that, however the electronic Hamiltonian does not include any spin dependent term, the inclusion of spin eigenfunctions in defining

the spin-orbitals of the Slater determinant makes the eigen solution of the electronic Hamiltonian a dependent of the spin configuration of the electrons. This is termed as exchange correlation. The probability density of the electronic wavefunction contains cross terms between different spin-orbitals that correlates the parallel spin electrons and thus modifies the electronic properties of the molecular system. Also, since the  $H_{elec}$  commutes with the total spin operator  $\hat{S}^2$  of the electrons, it is used to define the electronic states.

Because of the BO approximation and the view that electrons move in the Coulomb field created by the 'static' nuclei, the electronic wavefunction inherits the symmetry of the nuclear conformation. Consequently, the eigen solution of the electronic Hamiltonian depends upon the symmetry of the Coulomb field.

In case of molecules, because of the absence of spherical symmetry of the Coulomb potential as it exist in case of atoms, the total angular momentum of the electrons do not commute with  $H_{elec}$ , thus do not contribute in their eigen states. However, for linear molecules, where there exist an axial symmetry in the Coulomb field, axial component of momentum does commute and result the different energy eigen values for states having different axial angular momentum. The total spin of the electronic wavefunction and the axial momentum component in case of linear molecules are used in specifying the electronic eigen functions  $\Phi_{elec}$ .

In addition to the axial symmetry, the nuclei conformation of the molecular system can possess other symmetries. The eigen basis sets of these operators affect the eigen values of  $H_{elec}$  and thus are designated in specifying the electronic eigen functions  $\Phi_{elec}$ . The symmetry properties of a given conformation of the nuclei is expressed by point groups which represent the set of all distinct classes of symmetry operations that are possessed by the nuclei coulomb field of the molecule. The common classes used to define the symmetries are inversion  $i$ , reflections  $\sigma_v$  and  $\sigma_h$ , proper rotations  $c_n$  and improper rotations  $s_n$ . The electronic eigenfunction must commute with each of these symmetry operations that are present in the point group. As a result, for a given point group the simultaneous existence of these symmetries create a restrictive set of eigen values of these symmetries that an electronic wave function may take. These are called irreducible representations

and are equal in number of the symmetry classes of the point group. Any electronic wave function of the  $H_{elec}$  must follow one of these irreducible representations of the point group. An account of the group theoretical treatment of the molecular symmetry and the properties of the electronic wave functions can be found in [117].

For instance, the linear molecules fall in either  $C_{\infty v}$  or  $D_{\infty h}$  point group. The ' $\infty$ ' in their label represent the existence infinite proper rotations along the molecular axis; responsible for the conservation of axial momentum. The point group of linear molecules which have no inversion symmetry is  $C_{\infty v}$ , whereas molecules having inversion symmetry fall in  $D_{\infty h}$ . The  $C_{\infty v}$  and  $D_{\infty h}$  point groups are used for specifying the electronic states of CO and  $N_2$  respectively. However methods, discussed in the section 4.3, that used to calculate the electronic structure are based on the symmetry adapted linear combinations basis sets for the finite point groups. The finite point groups  $C_{2v}$  and  $D_{2h}$ , which are the subset of their corresponding  $\infty$  point groups are used in the calculation. A correspondence which establish equivalence relations between the irreducible representations of the infinite point group with their finite subgroup is used to obtain the electronic states of the molecular system in their infinite point group irreducible representation [118].

### 4.1.3 Properties of the PECs

As discussed in the previous section, the total spin, axial angular momentum, and eigen states of symmetry operators are used to define the electronic wavefunction. Under BO approximation, since the coupling between electronic states are neglected, the symmetry properties of the electronic wavefunction will be same on the entire potential energy curve. Each of the PECs are designated by a set of values of the properties discussed that can be written as  $\{ |s|, |L_z|, \sigma_n, i, \dots \}$ , where  $\sigma_n$  represents the planer symmetry and can take one of the two eigen states, symmetric and antisymmetric, represented by '+' and '-' respectively.  $i$  represents the inversion symmetry and their two eigen states, even and odd parity are shown by 'g' and 'u' respectively. The electronic states are normally written as  $\mathbf{n}^{2s+1}\Lambda_{g/u}^{+/-}$ , where  $\mathbf{n}$

represents the  $n$ th state in the designated symmetry. For larger molecules, the Schönflies notations are generally used in defining the electronic eigenfunctions, potential energy curves and surfaces.

In case of diatomic molecules, the PECs in general can be categorised on the basis of their nature with respect to the internuclear distance. For polyatomic molecules where more than one ( $3M - 5$  for linear, otherwise  $3M - 6$ ) variables are involved to define the complete potential function for nuclei, additional parameters like saddle point etc, are used to describe the nature of the potential surfaces. If the PEC:  $V(\mathbf{R})$  is entirely repulsive possessing no minima, it will not support any bound state. On the other hand, if the PEC have some minima, it will support the bound states and the solution of eq 4.8 will provide the discrete eigen energy states associated with the PEC. These are the vibrational states of the PEC because they manifest the nuclei motion in the molecular system. In case of dissociation ionization of diatoms of  $N_2$  and CO, as it will be discussed in section 5.3, there are few low-lying states which support vibrational structure. It is thus necessary to know the properties of the vibrational states that are crucial in the dissociative ionization processes. In the section 4.1.4, the relevant properties of vibrational states are discussed.

The one other important aspect of the PECs for the diatomic molecules is that the PECs of same symmetry, in general, do not intersect. This is called Neumann-Wigner non-crossing rule [119]. It is based on the fact that the PEC:  $V(\mathbf{R})$  as function of only one variable  $\mathbf{R}$  does not allow eigenfunctions of same symmetry to have same value eigen value at a given  $\mathbf{R}$ [120]. However, accidental crossing may occur. On the other hand, non crossing rule does not impose any restriction for the PECs of different symmetry. Non-crossing rule also establishes that the molecular orbitals (MOs) of diatomic molecules of same symmetry can not cross on the MO correlation diagram. MO correlation diagram relates the MO with AOs and are very useful in identifying the symmetry relations and their energy ordering. It is important to mention that BO approximation ignores the coupling between different PECs and at the crossing points of the PECs, non-BO dynamics may occur. It will be seen in the Chapter 5, the signature of non-BO processes because of

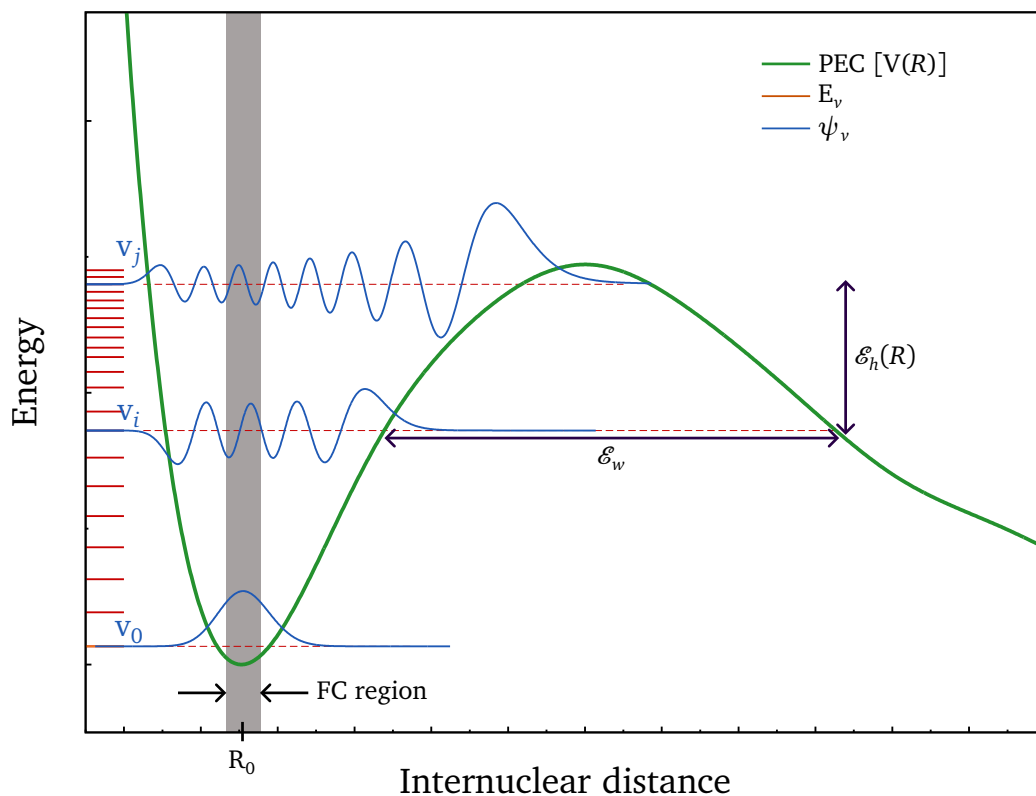


Figure 4.2: A schematic diagram of a PEC  $[V(\mathbf{R})]$  supporting the vibrational structures are shown. A set of vibrational states associated with the PEC is shown by continuous lines near the energy axis. The vibrational wave functions for three levels  $v_0, v_i, v_j$  are shown at their reference energies. The parameters; tunneling width  $\mathcal{E}_w$  and tunneling barrier height  $\mathcal{E}_h(R)$  that decide the probability of tunneling from a vibrational level are shown for  $v_i$ . The vertical shaded region centered at the zeroth vibrational level  $v_0$  represents the FC region (for details see the text).

coupling of the PECs at the crossing are found in the dissociative ionization of the dications of  $\text{N}_2$  and  $\text{CO}$ .

#### 4.1.4 Vibrational structures of the PECs

In the vicinity of the minimum on the PEC, at  $\mathbf{R} = \mathbf{R}_0$  in the Figure 4.2, the nature of the curve can be approximated by a Harmonic oscillator that gives the approximate wavefunction and energy of the associated vibrational states  $\{\psi_{v,n}, E_{v,n} : n = 0 \dots \infty\}$ . However, the nature of the PECs can not be accounted by this approximation because PECs have finite dissociation energy which Harmonic oscillator model does not predict. Further, unlike the Harmonic oscillator potentials, the PECs are not

symmetrical with respect to the  $\mathbf{R}_0$ . The PECs in general grow very steep for  $\mathbf{R} < \mathbf{R}_0$  and reach to the asymptotic limit energy rather gradually in the region  $\mathbf{R} > \mathbf{R}_0$ . Many other analytical functions viz. Morse potential, Lennard-Jones potential are used as an approximation of the PECs. On the other hand, eq 4.8 can be solved for the PECs using numerical methods. A set of vibrational levels associated with the PEC are shown as continuous lines near the energy axis in the Figure 4.2.  $v_0$  represents the zeroth vibrational level. It should be noted that the difference between vibrational energies decreases for higher vibrational states. Also, for higher vibrational states the wave function gets distorted more and consequently their probability density increases for larger  $\mathbf{R}$  (see nature of  $\psi_{v_j}$  in comparison of  $\psi_{v_0}$  and  $\psi_{v_i}$  in the Figure 4.2).

The other crucial aspect of the vibrational states associated with the PECs of the molecules is that they may have finite tunneling life time for dissociation (though it may be very large in some cases and can be considered infinite for any practical purpose). For a given PECs, the associated vibrational states that have very large tunneling life time will be considered as stable (mostly the levels in the vicinity of the PEC minima). On the other hand, vibrational states having small tunnelling life time will dissociate (top-most levels). This is the reason that makes it extremely important to calculate the properties of the vibrational states in the study of dissociative ionization. The energy of the vibrational states, their tunneling life time, width of the states are calculated using WKB approximation. In the classically allowed region ( $E_v > V(\mathbf{R})$ ) on the PEC, the solution of the eq 4.8 will be

$$\psi_v(\mathbf{R}) \cong \frac{C}{\sqrt{p(\mathbf{R})}} \exp \left[ \pm \frac{i}{\hbar} \int^r p(r) dr \right] \quad : E > V(\mathbf{R}) \quad (4.13)$$

where  $p(\mathbf{R})$  is  $\sqrt{2\mu[E - V(\mathbf{R})]}$ . For the region, ( $E_v < V(\mathbf{R})$ ) outside the classical range, the WKB solution will be

$$\psi_v(\mathbf{R}) \cong \frac{A}{\sqrt{|p(\mathbf{R})|}} \exp \left[ \pm \frac{1}{\hbar} \int^r |p(r)| dr \right] \quad : E < V(\mathbf{R}) \quad (4.14)$$

In equation 4.13 and 4.14,  $C$  and  $A$  are normalization constants. It can be seen that the vibrational wavefunctions depend upon the nature of PECs in the entire range of  $\mathbf{R}$ . In addition, properties like the tunneling life time are extremely sensitive to the nature of the PEC because of exponential dependence on the tunneling width,  $\mathcal{E}_w$  and height,  $\mathcal{E}_h(R)$  and thus very precise calculation of the PEC is prerequisite. The tunneling transmission probability in this case is

$$T \cong \exp \left[ - \frac{2}{\hbar} \int^{\mathcal{E}_w} |p_b(r)| dr \right] \quad (4.15)$$

In the eq 4.15,  $p_b(r)$  uses the information of the barrier heights in the tunneling range, ( $E_v < V(\mathbf{R})$ ). In the section 4.3.6, calculation details are given.

## 4.2 Dissociative ionization processes in molecules

As discussed in the section 4.1.1, the general conception that the electronic motions are much faster than the motion of nuclei in the molecular system based on the large differences in their masses but comparable interaction via coulomb forces forms the basis of BO approximation and consequently allow to understand separately the dynamics electronic and nuclei motions. In a collision process involving various excitations, it sets the order for the processes in general. Electronic excitation and rearrangement is the first to happen as an effect of any perturbation to the molecular system. This establishes two very crucial concepts in understanding the kinematics resulting from the processes involving electronic excitation, the first is the vertical transition and the other is the notion of Franck Condon region [121]. Vertical excitation is the manifestation of the dynamical time scale differences of the electronic and nuclei motion on the potential energy diagram. It suggests that the excitation in the molecular system would be vertical displaying the change in the energy but no change in the molecular conformation. In the Figure 4.2, the vertical excitation is shown by the shaded region around  $\mathbf{R}_0$ . Since the electronic excitation is vertical on the potential energy diagram, the probability distribution of the initial state gets mapped on the excited states. This is represented by the

Franck Condon region, showing the extent of the probability distribution of the initial state. In the Figure 4.2, the width of the shaded region shows the probability distribution of the zeroth vibrational state. It plays a crucial role in the kinematics resulting from the various excited states. Their importance will be emphasised in the discussion of the Figure 4.3 in concern of the KER obtained from the excited PECs.

As introduced in the section 1.4, in the dissociative ionization process, the ionization and dissociation of the molecular system occur upon the collision with some ionizing element. Ionization of the molecular system mark the formation of the molecular ion. The further evolution of the molecular ion depends upon its dynamical evolution that can be completely understood on the PECs in the BO picture. The molecular ion may remain as stable system or dissociate into its fragments. The dissociation of the molecular ion can be categorised into two classes namely direct processes and indirect processes. These categories are based on the underlying nature of interaction that govern the dynamics of the molecular ion after ionization.

### 4.2.1 Direct processes of dissociation

When the dynamical evolution of the molecular ion occurs on a single PEC, leading to dissociation, it is termed as direct process. Evidently such processes follows the adiabatic assumption employed in the BO approximation that ignores the coupling of the PECs. Direct dissociation can be observed from the repulsive PECs as well as PECs having local minima. The formation of molecular ions on an entirely repulsive PEC, such as in PEC-a; Figure 4.3, inevitably result in dissociation. The KER from such curves will have modal value equal to the difference of the potential energy at  $\mathbf{R} = \mathbf{R}_0$  and  $\mathbf{R} = \infty$  (asymptotic limit). The distribution in the KER is the manifestation of the probability distribution of the initial state mapped on the PEC. It is clear that the more steep PEC in the vicinity  $\mathbf{R}_0$  will produce the more broad KER distribution [width of the KER-a]. In chapter 5, KER distributions resulting from the many low-lying repulsive states of  $\text{N}_2^{++}$  and  $\text{CO}^{++}$  are shown by Gaussian

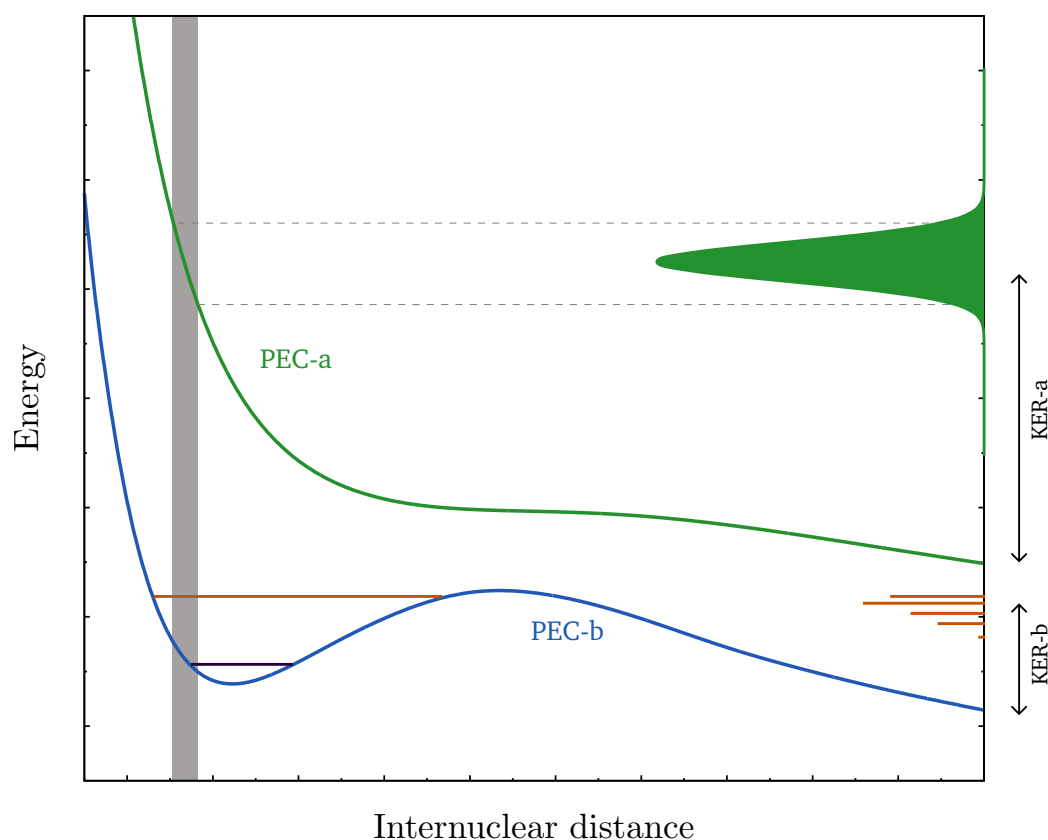


Figure 4.3: A schematic of the KER resulting from the direct dissociation from a repulsive PEC-a and via tunnelling from the vibrational levels of a PEC supporting minima, PEC-b are shown. In the PEC-b, two representative vibrational levels are shown to highlight two classes, namely dissociating and non-dissociating vibrational levels via tunneling. However, the lines in the KER-b are arising from the separate dissociating vibrational levels. The vertical shaded region represent the FC region. The height of the lines in the KER-b represent the FC factor of the dissociating vibrational levels. KER-a represents the KER distribution arising from PEC-a.

distributions in the upper panel of the Figure 5.8 and 5.9 respectively.

The direct dissociation can also occur from the PECs supporting vibrational structures via tunnelling. As discussed in the section 4.1.4 the tunneling life time of the vibrational state will decide whether the molecular ion will be observed as a stable system or will dissociate into its fragments. The KER energy for the vibrational level is the difference in the energy of the vibrational state PEC-b:  $E_v$ , and the energy of the asymptotic limit of the PEC. The relative excitation in the vibrational levels that eventually observed as intensity of their KER peak and is given by the Franck Condon (FC) factor. FC factor is proportional to the overlap

integral of the initial state,  $\psi_0$  of the molecule with the final state,  $\psi_v$ ". It is calculated assuming the vertical transition and can be written as

$$FC(v', v'') = \int \psi_{v'}' \psi_{v''}'' dr \quad (4.16)$$

In the Figure 4.3, the height of the KER peak resulting from the vibrational states represent their FC factors [KER-b]. In chapter 5, the contributions from the decaying vibrational states of  $N_2^{++}$  and  $CO^{++}$  are shown by vertical bars in the Figure 5.8 and 5.9 respectively.

### 4.2.2 Indirect processes of dissociation

Indirect dissociation processes of molecular system involve coupling of PECs in the course of dissociation and thus are signature of the non-BO dynamics. The two major indirect processes that can be observed in the dissociative ionization are autoionization and predissociation. These processes are discussed in the view of exploring the nature of non-BO dynamics in many cases [122, 123]. In this section these processes are explained for the dissociation of dications of diatomic molecular ion (say  $AB^{++}$ ).

In the predissociation, because of the coupling of the PECs, transition from one PEC to the other opens up the possibility of dissociation from the "stable" vibrational levels that are otherwise can not decay. The process of predissociation can be understood using Figure 4.4. The two PECs, PEC-p and PEC-q are shown with their asymptotic limit energies  $E_p$  and  $E_q$  respectively. The predissociation can also happen between two repulsive or two states having a local minima. For the PEC-q, the bound state region have two parts. Up to  $E_{v_1}$ , the vibrational states are stable against tunneling. On the other hand, only the vibrational levels lying in the energy region  $E_{v_2}$  will dissociate. The coupling with PEC-p provides a way other than tunneling for dissociation of the "stable" vibrational levels (levels in the  $E_{v_1}$  region). As a result of predissociation, the vibrational levels of the PEC-q acquire finite life time for dissociation. The signature of these vibration levels that dissociate via PEC-p will emerge in the KER spectrum of the dissociation. The KER

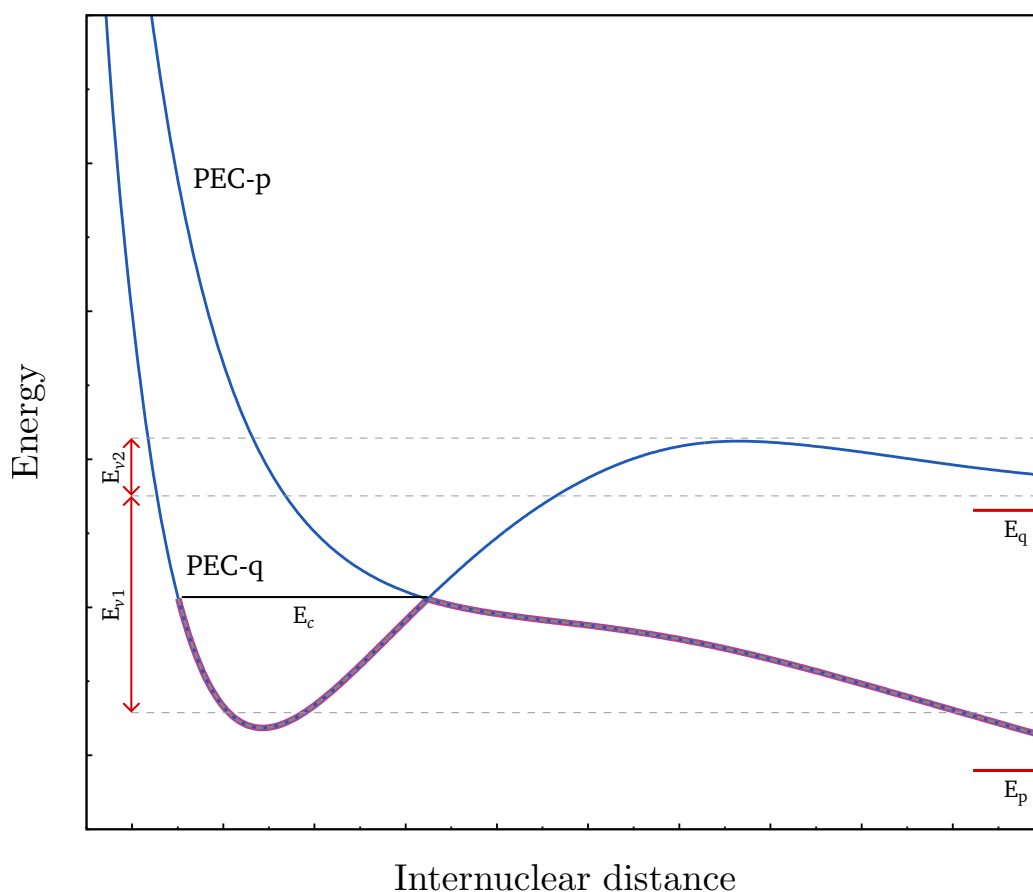


Figure 4.4: A schematic of the predissociation of the vibrational states of PEC-q via a repulsive PEC, PEC-p is shown.  $E_{v1}$  and  $E_{v2}$  represent the energy range for the stable and dissociating vibrational levels via tunneling.  $E_p$  and  $E_q$  are the asymptotic limits of PEC-p and PEC-q respectively.  $E_c$  is the vibrational level for which the crossing between the PECs will be most effective.

value of these states will appear with a shift in energy equal to the difference in the asymptotic limits  $E_p - E_q$ .

Predissociation occurs efficiently at the crossing of the PECs. This is because of the fact that the motion of nuclei, because of their large masses on the PECs is quasi-classical. For such systems, the transition probability (from one state to other) is chiefly determined by the point at which the transition could occur classically. The condition for classically possible transition for a diatomic molecular system assuming the conservation of total energy and angular momentum is satisfied at the crossing point of the PECs ( in Figure 4.4  $PEC-p(r) = PEC-q(r)$  that can be rewritten in terms of the relative position and the linear momentum of nuclei of the

diatomic molecule as  $r_p = r_q, p_p = p_q$ ). This relation is in accord with the Franck Condon principle, which allows the change in the electronic configuration for the transition from the one PEC to the other while preserving the distance between nuclei and their relative momentum constant.

The requirement that there should be an intersection of the PECs means that predissociation can occur only in states of the different symmetry (non-crossing rule). In addition, there are constraints based on the symmetry properties of the electronic terms that control the transition probabilities. For any transition between electronic terms, total angular momentum and inversion symmetry must be conserved. Also, the transition is possible between PECs for which  $\Delta S$  and  $\Delta \Lambda$  change by  $0, \pm 1$ .

Autoionization process occurs because of the coupling of PECs of different ionised state of the molecular system. As a result, it involves ionization of the molecular system at the point of transition. In context of dissociative ionization of doubly ionized molecular ions  $AB^{++}$ , autoionization happens from the highly excited states of singly ionized ions  $AB^{+*}$ . The highly excited singly ionized molecular ions are often repulsive and after formation of molecular ion, it starts dissociating. The coupling of such states with the PECs of dications in the course of dissociation result in autoionization. The process of autoionization is generally understood by viewing the autoionization state of  $AB^{+*}$  as a compound state of an ionic core  $AB^{++}$  and a weakly bound electron by its Coulomb field. In such systems, when the internal energy of the ionic core happens to be greater than the binding energy of the excited electron, autoionization may occur [124]. To explain such transitions, the non-adiabatic terms of the exact Schrödinger equation for the motion of nuclei (that are ignored in the Eq 4.6) must be considered. They are used as a coupling terms between the core vibrations and the states of the excited electron.

It is important to mention here that the autoionization rate increases for heteronuclear diatomic molecules because of the non-zero interaction of excited electron with vibrating dipole of the core. On the other hand, for homonuclear molecule, the transition governing the autoionization arises from the interaction of the excited electron with the vibrating quadrupole of the core [125].

The signatures of these non-BO processes are seen in the kinematics of the dissociative ionization of the molecules. In chapter 5, these indirect processes are identified in the dissociation channels of the dications of N<sub>2</sub> and CO.

### 4.3 Methods of calculation

In the first part of this section, a discussion on the methods to calculate the  $\Phi_{elec}$  for a given  $H_{elec}$  is provided. The eigen equation given in the eq 4.5 has infinite eigen solutions that represent the electronic states of the molecular system {M,N} for a certain conformation {R}. The functional form of the  $\Phi_{elec}$  is the Slater determinant and has been considered in the section 4.1.2. The methods discussed in this section are based on the linear variation procedure to obtain the electronic wavefunction. Numerically, the method of linear variation iteratively improves upon the trial wavefunction of the system and procure the best possible electronic wavefunction for the system which is called the self consistent field solution. These methods are different from each other on the basis of the size and the way their wavefunction spaces are defined. In the section 4.3.3, the need for very accurate calculation is highlighted. In the last section, a brief discussion on the methods to calculate the electronic energy and the vibrational energies, their life time and Franck Condon factors is provided.

#### 4.3.1 Linear variational procedure

The complete set of eigen solutions of the Hamiltonian  $H_{elec}$  can be written as (this equation is identical to the eq 4.5, except the (r,R) dependence is dropped from the expression of electronic eigenfunction and eigen energy)

$$\hat{H}_{elec}|\Phi_{\alpha}^{\circ}\rangle = \mathcal{E}_{\alpha}^{\circ}|\Phi_{\alpha}^{\circ}\rangle \quad \alpha = 0, 1, \dots, \infty$$

where

$$\mathcal{E}_0^{\circ} \leq \mathcal{E}_1^{\circ} \leq \mathcal{E}_2^{\circ} \leq \dots \mathcal{E}_{\alpha}^{\circ} \leq \dots \quad (4.17)$$

The eigen (exact) solutions  $\{|\Phi_\alpha^\circ\rangle\}$  are orthonormal and form a complete set. Since, the exact functional form of  $\{|\Phi_\alpha^\circ\rangle\}$  are not known, only the approximate solutions of the eq 4.17 can be found.

The premise of linear variation method in order to find the solution of the eq 4.17 is the fundamental property that any function can be expressed in terms of the linear combination of the basis functions of a complete set. Ideally, any known complete orthonormal basis set, say  $\{|\Psi_k\rangle; k = 0, \dots, \infty\}$  in the same Hilbert space of  $H_{elec}$  can be used to express the eigen solutions,  $|\Phi_\alpha^\circ\rangle$ . The general form of the linear expansion in terms of  $\{|\Psi_k\rangle\}$  can be written as

$$|\tilde{\Phi}_\alpha\rangle = \sum_{k=1}^K c_{\alpha k} |\Psi_k\rangle \quad (4.18)$$

Where  $\{|\Psi_k\rangle; k = 0, \dots, K\}$  is a known orthonormal and normalised basis set. When  $K \rightarrow \infty$ , the set of basis function forms a complete set. In order to achieve the explicit form of  $|\tilde{\Phi}_\alpha\rangle$ ,  $\{c_{\alpha k}\}$  are obtained by minimising the expectation value  $\langle \tilde{\Phi}_\alpha | \hat{H}_{elec} | \tilde{\Phi}_\alpha \rangle$ . The procedure uses the variation principle which assures that the expectation value of  $H_{elec}$  in the approximated electronic states  $|\tilde{\Phi}_\alpha\rangle$  will always be the upper bound of the eigenvalues of  $H_{elec}$ . After performing linear variation, we find  $K$  solutions which can be written as follows

$$\mathbf{H}\mathbf{c}^\alpha = \tilde{E}_\alpha \mathbf{c}^\alpha$$

$$\mathcal{E}_0^\circ \leq \tilde{E}_0, \quad \mathcal{E}_1^\circ \leq \tilde{E}_1, \quad \mathcal{E}_2^\circ \leq \tilde{E}_2, \dots, \quad \mathcal{E}_\alpha^\circ \leq \tilde{E}_\alpha \quad (4.19)$$

In the above equation,  $\mathbf{H}$  represents a square matrix of dimension  $K \times K$  where its  $ij^{th}$  element is  $\langle \Psi_i | \hat{H}_{elec} | \Psi_j \rangle$ .  $\mathbf{c}^\alpha$  represents a column vector with elements  $c_{\alpha i}$ ;  $i = 1, K$  and equivalent to  $|\tilde{\Phi}_\alpha\rangle = \sum_{k=1}^K c_{\alpha k} |\Psi_k\rangle$ .  $\tilde{E}_\alpha$  are the  $K$  eigen solutions of the equation 4.19. In the limits when  $K \rightarrow \infty$ , the  $\{|\tilde{\Phi}_\alpha\rangle\}$  will become the exact solution of the  $H_{elec}$  and  $\tilde{E}_\alpha$  will become equal to the  $\mathcal{E}_\alpha^\circ$ . It is important to mention that the linear variational procedure constrain the calculated  $\{|\tilde{\Phi}_k\rangle\}$  basis set to be normalised and orthonormal (as the primary basis set  $\{|\Psi_k\rangle\}$  are).

Since only a finite basis set ( $K \neq \infty$ ) can be used, it introduces an error in the calculated properties of the electronic Hamiltonian. The accuracy of the calculation can be always improved by using the bigger basis sets. In addition, accuracy of the calculation also depends crucially on the way the primary basis set is build. This point will be clear in the next section in the discussion of basis sets.

### 4.3.2 Building the N-electron basis functions for SCF method

The simplest N-electron wavefunction is the the Slater determinant, eq 4.12, which satisfies the antisymmetric properties and constituted by the N single-electron orbitals. For a given Slater determinant  $|\Psi_0\rangle = |\chi_1\chi_2\chi_3 \dots \chi_N\rangle$ , the variation of the molecular orbitals  $\chi_i; i = 1, \dots, N$  in order to minimise the expectation value of  $\langle \Psi_0 | H_{elec} | \Psi_0 \rangle$  will result in what is known as Hartree-Fock equation.

$$f_i |\chi_i\rangle = e_i |\chi_i\rangle \quad ; i = 1, \dots, N \quad (4.20)$$

The equation 4.20 is a canonical form of the Hartee-Fock equation. In the above equation  $f_i$  is an effective one-electron operator and is termed as Fock operator. The set of  $e_i$ s represent the orbital energies of the electronic Hamiltonian,  $H_{elec}$ . The Fock operator can be written as

$$f_i = -\frac{1}{2}\nabla_i^2 - \sum_{A=1}^M \frac{Z_A}{r_{iA}} + v^{HF}(i) \quad (4.21)$$

In the above equation, the first and second term in the Fock operator,  $h(1)$ , are kinetic and potential operators of the single electron in the coulomb field of the nuclei of the molecular system. It is normally called the bare nuclei Hamiltonian. The Fock operator includes the sum of the two terms namely exchange and coulomb integral which depends upon the spin orbitals of the other electrons and is collectively written as  $v^{HF}(i)$  in eq 4.21. These terms make the Hartree-Fock equation non-linear and thus it must be solved iteratively. The procedure for solving the Hartree-Fock equation is called the self-consistent-field (SCF) method. In the SCF

method, a trial wavefunction constituting  $N$  spin-orbitals are first used to calculate the effective potential  $v^{HF}(i)$ . This potential is further used to calculate the new  $N$  molecular orbitals that are variationally better solution of the  $H_{elec}$ . The iteration continues until a self consistent solution is achieved.

In order to introduce the variationally appropriate molecular orbitals, the spatial molecular orbitals can be written as sum of atomic orbitals.

$$\Psi_i = \sum_{\mu=1}^K C_{\mu i} \Phi_{\mu} \quad \mu = 1, 2, \dots, K \quad (4.22)$$

In the above equation, the spatial molecular orbital  $\Psi_i$  are created orthonormal. With this condition we will have  $K$  such orbitals. The solution of the Hartree-Fock equation, eq 4.20, can be given as

$$\mathbf{FC} = \mathbf{SC}\epsilon \quad (4.23)$$

The equation 4.23 is known as Roothaan equation. In the equation  $\mathbf{F}$ , the Fock matrix, is a  $K \times K$  Hermitian matrix with elements  $F_{\mu\nu} = \langle \Phi_{\mu} | f(1) | \Phi_{\nu} \rangle$ .  $\mathbf{S}$ , the overlap matrix with elements  $S_{\mu\nu} = \langle \Phi_{\mu} | \Phi_{\nu} \rangle$  is a square matrix of dimension  $K$ .  $\epsilon$  is a  $K \times K$  diagonal matrix and their diagonal elements represent the molecular orbital energies.  $\mathbf{C}$  is a  $K \times K$  matrix and provide coefficients of expansion for the  $K$  molecular orbitals. The Roothaan equation provides  $K$  ( $\mu = 1, \dots, K$ ) molecular orbitals  $\{C_{\mu i}; i = 1, \dots, K\}$  and their energies  $\epsilon_{\mu}$  ( $\mu = 1, \dots, K$ ). When  $K$  is equal to  $N$ , the molecular basis set is called minimal basis set. However, when  $K \rightarrow \infty$  the  $\{\Psi_i\}$  will form a complete set.

Using the orbital energies  $\epsilon_i$ s, the molecular spin orbitals  $\{\chi_i\}$ s can be arranged in the order of increasing energy. The determinant formed by the  $N$  lowest energy molecular orbitals provides the ground state Hartree-Fock wave function,  $|\Psi_0\rangle$  (will be discussed in the next section). There are many other  $N$ -electron Slater determinant that can be formed employing the various combination of spin orbitals from the  $\{\chi_i\}$  space. These Slater determinants can be expressed in reference to

the Hartree-Fock determinant,  $\Psi_0$ . The exact wave function for any state of the N-electron system can be written as

$$|\Phi\rangle = c_0|\Psi_0\rangle + \sum_{ra} c_a^r |\Psi_a^r\rangle + \sum_{a<b, r<s} c_{ab}^{rs} |\Psi_{ab}^{rs}\rangle + \sum_{a<b<c, r<s<t} c_{abc}^{rst} |\Psi_{abc}^{rst}\rangle + \dots \quad (4.24)$$

In the above equation,  $a, b, c \dots$  represent the N lowest energy molecular orbitals and are commonly known as occupied orbitals.  $r, s, t \dots$  represent molecular orbitals of energy greater than any of the N occupied orbitals, and are termed as unoccupied orbitals.  $|\Psi_a^r\rangle$ ,  $|\Psi_{ab}^{rs}\rangle$  and  $|\Psi_{abc}^{rst}\rangle$  represent the single-, double-, triple-excited configurations respectively. The set of infinite N-electron determinants  $\{|\Psi_0\rangle\} = \{|\Psi_a^r\rangle, |\Psi_{ab}^{rs}\rangle, |\Psi_{abc}^{rst}\rangle, \dots\}$  in the  $K \rightarrow \infty$  forms a complete set.

### 4.3.3 Hartree-Fock SCF method

In the Hartree-Fock method, the N-electron wavefunctions are represented by single Slater determinants. The best variational energy for the ground state,  $E_0$  of the system of Hamiltonian  $H_{elec}$ , will arise from the Slater determinant formed by N lowest occupied orbitals.

$$E_0 = \sum_a \langle a|h|a\rangle + \frac{1}{2} \sum_{ab} [aa|bb] - [ab|ba] \quad (4.25)$$

In the eq 4.25, the first term represents the sum of the expectation energy of the  $h(1)$  in the occupied orbitals. The second and third terms are the two-electron terms and are known as coulomb and exchange integrals respectively. The derivation and discussion on the HF theory can be found in [23].

It is important to mention that in the limit  $K \rightarrow \infty$ , the Hartree-Fock energies will reach its minimum. This is called Hartree-Fock limit. However, since the single determinants do not represent the exact eigenstates of N-electron system, even if the single electron basis set is taken from a complete set, the Hartree-Fock energies will not be the eigen energies of  $H_{elec}$  and will appear as the upper limit. The difference between the Hartree-Fock limit and the eigen energy of the

Hamiltonian is normally termed as the correlation energy. The correlation energies are recovered using the methods, known as post HF methods, that employ the multi-determinantal N-electron wave functions. The post-HF theories, CI, MCSCF and CASSCF and MRCI theories that has been used in the work will be accounted in the section 4.3.5.

Using a large basis set, the Hartree-Fock model can yield energies that are greater than the exact values only by 0.5%. But the energies involved in the molecular processes (bond breaking, bond rearrangement, dissociation) are very small fraction of the total energy. For instance, in case of  $N_2$  (or CO) molecule, the bond energies are of the order of 0.2%, which is too small to be accounted by the HF theory. In addition, the HF method does not describe the behaviour of the dissociation correctly except for the closed-shell systems. In order to understand the kinematics of the dissociative ionization of even the simple diatomic molecules, one needs to invoke the post-HF methods in the calculation. A good account on the comparison of the various computation methods on the basis of their predictions of the chemical behaviour in molecular processes can be found in [126, 127].

#### 4.3.4 Configuration interaction SCF methods

As mentioned in the section 4.3.2, the solution of Roothaan equation in the limit  $K \rightarrow \infty$  generates a complete set of one-electron function space  $\{\chi_i\}$ . The Slater determinants formed by the  $\{\chi_i\}$  create a complete space for the N-electron wave function. In the equation 4.24, the expansion of any N-electron wavefunction is expressed as linear combination of the Slater determinants. Configuration Interaction method is a linear variational method that optimises the coefficients of the determinants (CSFs) of the expansion to achieve the minimum total energy of  $H_{elec}$ . Since, computationally only the finite one-electron basis set can be used, for a basis set of dimension  $2K$ , the number of possible N-electron determinants is  $\binom{2K}{N}$ . The variational optimization of the expansion created by all the CSFs is known as full CI. The error introduced because of the expansion of the electronic wave function in the finite N-basis is known as finite basis set approximation.

However, even for small systems and minimal basis set the number of determinants in the N-electron basis is extremely large. As a result it becomes computationally impractical to embrace the full CI. The truncated CI are used in the calculation to achieve the reasonable accurate results with the realizable computational expense. The selection of the determinants from the full CI is done on the basis of the properties of the electronic state. For example, in the calculation of ground state wavefunction, the single excitations are neglected as a consequence of Brillouin's theorem [23]. Also the fact that no coupling term arises between the determinants different by two spin orbitals is used extensively in selecting the proper determinants in the calculation of states. On the other hand, the rejected determinants contribute to the electronic states indirectly by interacting with the determinants included in the expansion, but they offer negligible improvement in the properties of the electronic state.

Using the Brillouin's theorem and ignoring the indirect mixing of the triple and higher excitations in the calculation of the CI ground state, the correlation energy  $E_{corr}$  which is a measure of the improvement upon the Hartree-Fock energy can be written as (in the intermediate normalised CI)

$$E_{corr} = \sum_{a<b,r<s} c_{ab}^{rs} \langle \Psi_0 | H_{elec} | \Psi_0 \rangle \quad (4.26)$$

The full CI and the other CI methods recover almost the entire correlation energy and thus are able to capture the features of the molecular processes in dissociation. For instance, in case of  $H_2$ , using a considerably large basis set and the full CI/ DCI recovers 80% of the total correlation energy [Kolos and Wolneiwicz]. In case of  $N_2$ , SDCI calculation of the ionization potential of the two outer most occupied orbitals,  $3\sigma_g$  and  $1\pi_u$  using a very large Slater-type function (6s,4p,3d,2f) result in significantly accurate values that differ only in meV with experimental results. More accurate results have been obtained using more accurate basis sets. In this work correlation consistent atomic basis sets developed by Dunning and coworkers are used [128]. Also, in the calculation instead of using the separate determinants, linear combination of determinants known as symmetric-adopted

configurations are used, which are the eigen functions of the total spin operator of the electronic state. This reduces the size of the expansion quite extensively by removing the determinants of different total spin.

However, in order to achieve accurate results, CI calculations typically use  $10^3$  to  $10^8$  CSFs for small molecules. For large molecules, one needs to include even more CSFs. The resulting computational costs emerge as the limitation of the full or truncated CI methods in the calculation of the molecular properties.

### 4.3.5 MCSCF, CASSCF and MRCI methods

In the full and truncated CI methods, the linear variation is performed only of the determinantal coefficients of the CSFs that are created from the molecular orbitals of the Roothaan equations. In the Multi Configuration SCF (MCSCF) method, both the determinantal coefficients,  $c_I$ , as well as the expansion coefficients of the orbitals  $\{\chi_i\}$ s are variationally optimized simultaneously [129]. The MCSCF wavefunction can be written as, where  $|\Psi_I\rangle$ s are the CSFs.

$$|\Psi_{MCSCF}\rangle = \sum_I c_I |\Psi_I\rangle \quad (4.27)$$

In this method, the orthogonality condition between CSFs are maintained during the optimization by means of exponential transformations [130]. Efficient quadratically convergent Newton-Raphson type procedures are employed to determine the optimum values of the variational coefficients [131]. In the MCSCF calculations, because of the larger variational space, the computational effort is relatively huge. At the same time, development of the efficient methods have allowed to use the MCSCF calculations. M W. Schmidt and M S. Gordon provide a good review on the MCSCF method and its interpretation [21].

The most efficient MCSCF method is the complete active space SCF (CASSCF) method, developed by Ruedenberg and Sundbarg [132, 133]. CASSCF classifies the orbitals in two classes, inactive and active orbitals. The inactive orbitals are always doubly occupied in all the CSFs. Normally, the core orbitals of the participating

nuclei are taken as inactive. The reason is the insignificant variation in these orbitals because of the other nuclei and electrons. Consequently, they do not contribute in the molecular processes unless it is a core-specific phenomenon. The relative improvement in the total electronic wave function property is negligible if they are also considered active. In the multi-determinantal theories, the active orbitals are further seen in two parts, namely valence and external (virtual) orbitals. Valence orbitals are those which are occupied in the reference function, whereas external orbitals represent the unoccupied excited orbitals. The core and valence orbitals are jointly referred as internal orbitals. Using CASSCF spaces, which include only CSFs that involves only active orbitals, reduce the computational cost very effectively.

The further improvement in the electronic structure can be achieved using the Multi Reference CI (MRCI) method which uses a combination of the MCSCF and CI. The MRCI method uses the CSFs of the CASSCF space to write a linear expansion for the variation. The variational optimization of the coefficient of the reference function provide the MRCI solution. Because of the complexity and computational cost, MRCI uses only single and double excitations relative to the CASSCF reference function [134]. This is normally referred as MRCI-SD. A MRCI-SD wavefunction can be written as

$$|\Psi_{MRCI}\rangle = |\Psi_0\rangle + \sum_I d_I |\Psi_I\rangle + \sum_S \sum_a d_S^a |\Psi_S^a\rangle + \sum_P \sum_{ab} d_P^{ab} |\Psi_P^{ab}\rangle \quad (4.28)$$

where

$$|\Psi_0\rangle = \sum_k a_k \Psi_k^{ref} \quad (4.29)$$

is the reference state function which is composed of many CSFs using the optimized CASSCF/MCSCF coefficients  $a_k$ .  $|\Psi_I\rangle$ ,  $|\Psi_S^a\rangle$  and  $|\Psi_P^{ab}\rangle$  represent the internally excited, singly excited and doubly excited configurations respectively. The  $d$ s represent their variational coefficients.

The MRCI method results almost accurate result as one will achieve from the CI methods using a large atomic basis set. The reason for achieving highly precise results from the MRCI-SD calculations is that it effectively includes the

most important CSFs up to quadruple excitations. For example, for 10-electron system, MRCI-SD using correlation consistent basis set recovers almost 97% of the total correlation energy. Whereas, CI-SD would give about 90-95 % of the basis set correlation energy. In the CI methods, only when triple and quadruple excitations are included will provide up to 99% of the correlation energy [135].

### 4.3.6 Calculation performed

In this work, the CASSCF and MRCI methods are used to calculate the electronic states of the molecular systems in question. The calculations are performed using Molpro program [136] package at the level of cc-pV5Z correlation consistent atomic basis sets. A brief information of these basis sets can be found in [137]. Molpro uses CASSCF by specifying the core and valence orbitals. It uses quadratically convergent MCSCF method for the optimization of the state [130, 138–140]. The CASSCF function is used as a reference function for MRCI calculation. The implemented method for MRCI calculation is internally contracted multiconfiguration-reference configuration interaction method, developed by Werner and Knowles [141]. The MRCI-SD program uses the contraction for the doubly excitation, whereas, internal and single external configurations will be usual uncontracted orthogonal eigen functions. The performed calculation involve about 2000 CSFs in CASSCF and MRCI calculation in case of diatomic molecules (for N<sub>2</sub> and CO). In context of the accuracy of the calculation, the total ground state energies of N<sub>2</sub>,  $^1\Sigma_g^+$  and CO,  $^1\Sigma^+$  are  $-109.398$  and  $-113.181$  H, which differs only 0.070 – 0.075% from the most accurate calculations of the ground states available for these molecules [using CCSD(T) method at the level of FULL/cc-pCVTZ] [142].

The vibrational structure of the PECs are calculated using the LEVEL program [143]. It solves the radial one dimensional Schrödinger equation 4.8 for the nuclear motion using the calculated PECs. The resulting solutions represent the vibrational and rotational structure of the molecular system. However, we have only computed the vibrational structure of the PECs. The vibrational states and its properties like tunneling life time, associated width etc are calculated using the

WKB approximation, discussed in the section 4.1.4. The FC factor of the vibrational states are also calculated using the zeroth vibrational state of the ground state of the molecules as reference. Using the calculated PECs, the zero point energy for  $1^1\Sigma_g^+$ ;  $v=0$  level of  $N_2$ , is calculated to be  $1172.9\text{ cm}^{-1}$ , whereas for the ground state of CO,  $1^1\Sigma^+$ ;  $v=0$ , it is  $1079.06\text{ cm}^{-1}$ . These values are only  $1.0\text{-}5.0\text{ cm}^{-1}$  different from the other accurate calculations reported in the literature [142].



# Chapter 5

## Results

This chapter contains the results of a comparative study of the features in dissociative ionization of the dications of  $N_2$  and CO. In the first section 5.1, in order to highlight the motivation of such comparative study, the similarities and differences in the static electronic properties of these diatomic molecules are examined. In section 5.2, the experimental results for these molecules obtained in a high energy electron impact collision are discussed. The effect of considering various transmission losses to calculate the accurate KER spectrum and double ionization cross sections from the observed kinematics are also discussed. Calculation of the PECs, asymptotic limits of the dissociation and the vibrational structures of these dications are provided in the next section 5.3. On the basis of the computed KER from the PECs of these dications, identification of the KER features is discussed in the section 5.4. The participation of the indirect processes like auto-ionization and predissociation in the dissociative ionization is observed. The comparison of the partial cross sections of the direct and indirect processes that are involved in the dissociative ionization of these dications is given in the section 5.5. This is done by defining a new parameter, the ratio of the cross-section of charge symmetric dissociative ionization to non-dissociative ionization (CSD-to-ND ratio). The scope of such comparison of the cross section ratios is justified on the basis of the similarities in their static electronic properties, double ionization cross sections and calculated Franck Condon factors of the stable vibrational levels for their

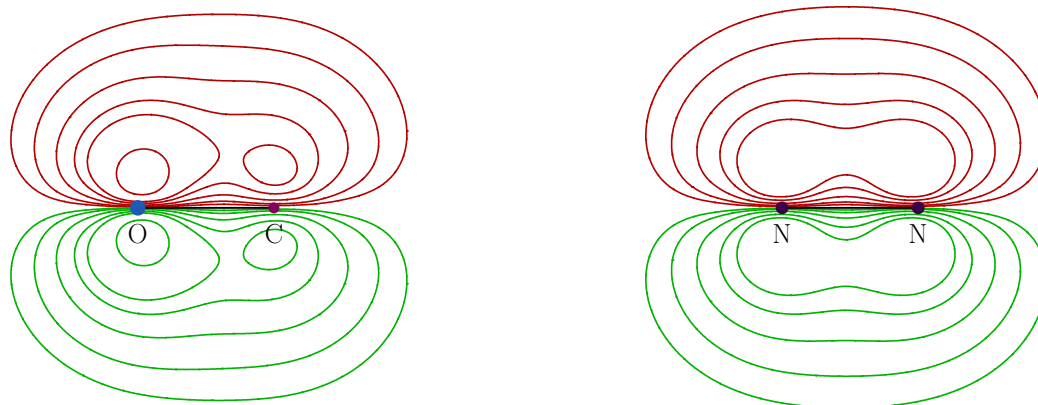


Figure 5.1: The contour plots of the highest occupied MOs of the ground state of  $\text{N}_2:1^1\Sigma_g^+$  ( $1\pi_u$ ) and  $\text{CO}:1^1\Sigma^+$  ( $1\pi$ ) are shown to illustrate their symmetries. In case of CO molecule, the inversion symmetry with respect to the center of mass of the molecule is not present, however  $\text{N}_2$  MOs do possess inversion symmetry. The isovalue contours are plotted for the range of 0.02 – 0.2 in the molecular plane. The upper half represent the '+' and the lower half represent the '-' part of the MOs.

doubly-ionized PECs. In the last section, results are concluded in the context of the relevance to quantify the various contributions of the BO and non-BO processes in the dissociative ionization of these dications.

## 5.1 The basis of a comparative study

$\text{N}_2$  and CO are iso-electronic molecular systems each having 14 electrons in their neutral state. Because of the similarity in the electronic properties, CO is normally categorized as near-homonuclear molecule. The total energy of the  $\text{N}_2$  and CO in their ground state is  $-109.398$  and  $-113.181$  H respectively, which is a difference of only about 3%. The Coulomb repulsion term between the nuclei of the CO at the equilibrium internuclear distance,  $R_0 = 1.13$  Å in its ground state is only about 4.75% smaller than for the  $\text{N}_2$  in its equilibrium configuration,  $R_0 = 1.10$  Å. The electronic configuration and the molecular orbitals for these molecules are also very similar with the notable difference of the inversion symmetry. The two valence orbitals of the  $\text{N}_2$  and CO are given in the Figure 5.1 for comparison.

In context of electronic excitation, the similarities extend to their ionization properties also. For example, the first ionization cross section, calculated with BEB model of  $N_2$  and CO differ by less than 1% for electron impact in the energy range 250-2000 eV [108]. Their ionization potentials are also very similar. In addition, the FC region which controls the excitation probabilities for the ionized molecular states are also nearly equal (see Figure 5.6 and Figure 5.7). Since the dissociative ionization process can be seen as a two step process of ionization followed by dissociation, the above arguments suggest that they can be compared separately for these dications. The similarities in the parent molecular systems as well as in their ionization properties assure that the transient molecular ions of  $N_2$  and CO would be akin to each other. The further evolution of the transient molecular ion is governed by the nature of their PECs and will decide the final state of the system. In this work, the comparative study is performed on the dissociation aspect of these dications. At this point, in order to examine the nature of the transient molecular ions, two categories can be addressed to compare; the one in which molecular ions remain stable after ionization and the other in which it dissociate. A comparative study on the basis of these two categories can be used to understand the nature of the dynamical evolution of the molecular ions of  $N_2$  and CO.

Most molecular ions with charge higher than two, due to strong Coulomb repulsion between the nuclei, generally possess purely repulsive potential energy surfaces with little structure. As a result, such ions are generally unstable and dissociate quickly into two or more fragment ions [95]. For such highly ionized molecular ions, because of the dominant involvement of purely repulsive curves, the simple coulomb explosion models are often able to produce a convincing picture of the evolution during the dissociation of the molecular ion.

On the other hand, the PES of singly and doubly ionized molecules exhibit interesting features arising due to competition between bonding and repulsive forces. In addition to purely repulsive states, there are several states having a minimum followed by a potential barrier connected to a dissociation asymptote which generally lies below the minimum. This leads to meta-stable vibrational states whose life-time is governed by tunneling through the potential barrier. Dications

are of special interest as they contain relatively smaller number of electronic states which support vibrational structure and hence are better candidates for probing various dissociation processes.

The dications of  $N_2$  and CO formed by charged particle collision or photoabsorption have been studied extensively with a view to understand the dynamics and evolution of multiply-charged molecular ions employing a variety of experimental methods [47, 91, 95–97, 144–149]. Their electron-spectra has also been analysed extensively to probe the properties of vibrational states [150–153]. The life time of the dications has also been studied in great detail and it is known that these dications have states with life times ranging from a few nano-seconds up to several seconds [87, 88, 154]. Also several investigations have shown the significance of indirect processes in dissociation of these dications [155–158].

In general, when a dication dissociates it may undergo either charge symmetric dissociation (CSD) in which the net positive charge on the molecular ion is equally shared by fragments, or charge asymmetric dissociation (CAD) in which charge sharing is unequal. The CSD and CAD of  $N_2^{++}$  and  $CO^{++}$  has been analyzed in many experiments. CSD is the energetically favored channel for these dications. This is because of the fact that the second ionization potential is much larger than the first one for all the dissociation fragment atoms. As a result, CSD is easily accessed in experiments and has been extensively discussed.

In the past, KER spectra of CSD of  $N_2^{++}$  and  $CO^{++}$  have been recorded experimentally with sufficient accuracy, resolving the contribution from many vibrational levels of low-lying states [47, 145]. There are many theoretical works involving computation of PECs of these dications [96, 144, 146, 159–163] to explain the experimental observations of different types of experiments, and some of the features in KER spectrum have been discussed in these studies [47, 96, 97]. Given the previously outlined similarities, it would be interesting to compare the kinematics of the dissociative ionization of these dications that has not been performed before.

Comparative study on these molecular ions is performed by analysing their CSD-KER spectrum. The analysis of the KER spectrum provides the identification of the different dissociation mechanisms in these cases. It is important to mention

that the identification of the features in the KER spectrum is solely based on the calculated energetics from the various dissociation pathways. Up till now, in the study of the dissociative ionization there is no way to distinguish the contribution arising from the two (or many) probable candidates that result in the similar energetics (i.e. KER). The comparative studies between similar molecular ions, however, enable further quantification of the underlying sources of dissociation without having unique identification of the observed features.

## 5.2 The experimental results

The experiments on the  $N_2$  and CO were performed on the RIMS set up, described in the Chapter 2. In this section, the observed TOF distributions of the product ions, time correlation maps of the fragments and the KER spectrum of the CSD break up of the dications  $N_2^{++}$  and  $CO^{++}$  is discussed.

### 5.2.1 The TOF spectrum

First-Hit TOF spectrum of  $N_2$  and CO observed in a high energy electron impact collision experiment are shown in Figure 5.2. The TOF spectrum of CO is shown with a vertical shift of 25 unit with respect to the base line of  $N_2$  TOF spectrum. Both spectra are normalized to the peak value of their singly-ionized molecular ion species. In both spectrum the identical  $m/q$  species can be easily noticed; one at  $6.57 \mu s$  mean TOF where the singly ionized parent ions of  $N_2$  and CO appear, the other appear around  $4.63 \mu s$  due to their doubly ionized stable molecular ions. The first hit TOF spectrum shows the ions that reach the detector first after their production in the ionization region. As a result, all dications which have not dissociated within the flight time will contribute to the first hit TOF spectrum along with the lightest of the fragment ions formed by dissociation. Since  $N_2$  and CO have nearly equal masses and consequently their singly- and doubly- ionized molecular ion peaks appear at nearly the same TOF, it is essential to ensure that there is no cross-contamination across the two experimental runs. By allowing a few days

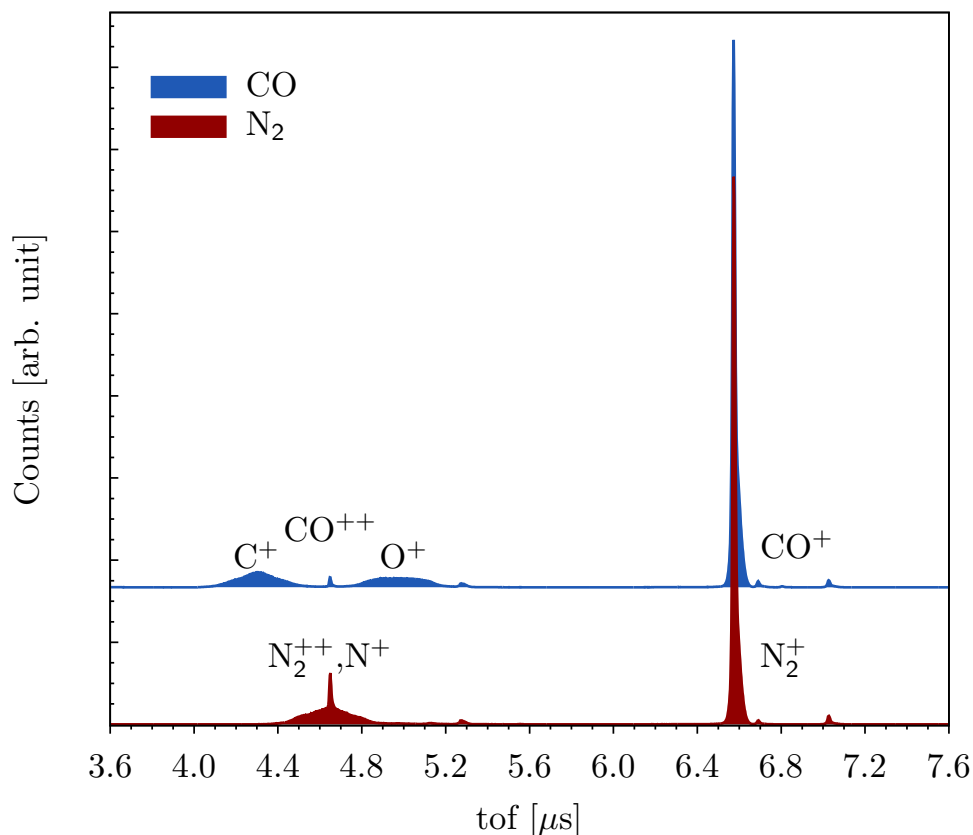


Figure 5.2: First-Hit ToF spectrum of N<sub>2</sub> and CO, observed in a high energy electron impact collision experiment is shown. The ToF spectrum of CO is shown with a vertical shift of 25 unit with respect to the base line of N<sub>2</sub> ToF spectrum. Both spectra are normalized to the peak value of their singly-ionized molecular ion species. The identical  $m/q$  species in both spectrum can be easily observed.

of pumping out time between runs, cross-contamination was nearly eliminated. This can be confirmed by examining the peak shape of the N<sub>2</sub><sup>++</sup> and CO<sup>++</sup>. The range that covers the fragmentation of doubly ionized molecular ions are shown in Figure 5.3. It can be observed that the CO<sup>++</sup> peak is very sharp, whereas N<sub>2</sub> contamination would have broadened the peak to the shape of N<sup>+</sup>. Further in case of N<sub>2</sub> spectrum, there is no peak around the positions where C<sup>+</sup> and O<sup>+</sup> would appear. The estimated contamination error is less than 1% for both spectra.

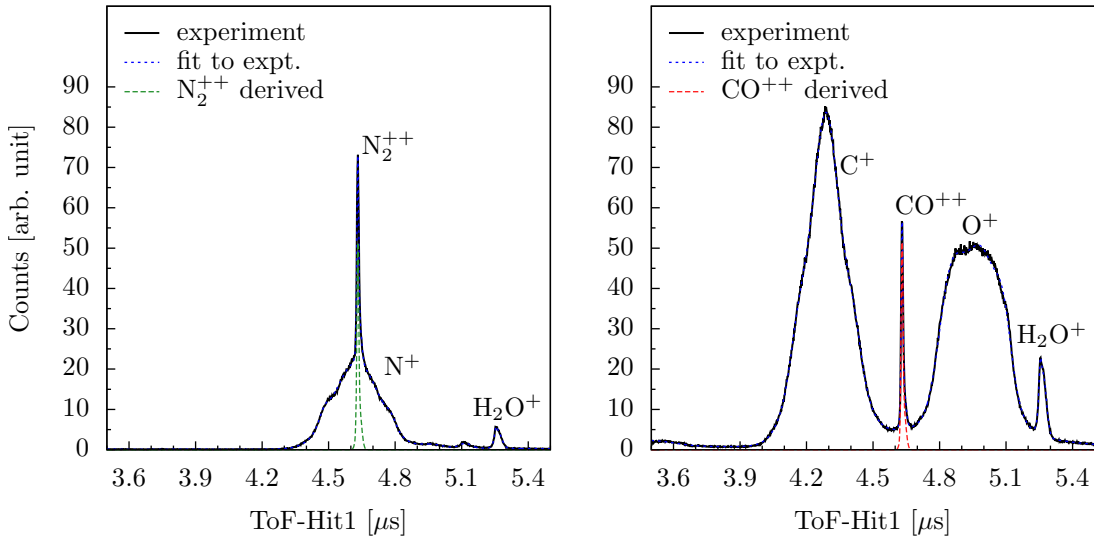


Figure 5.3: Partial first hit ToF spectra of  $N_2$  and  $CO$ , covering the range of doubly ionized molecular ions and the ions arising from their dissociation. Spectra are normalized to make the non-dissociated doubly-ionized molecular ion counts (of  $N_2^{++}$  and  $CO^{++}$ ) equal. The broken line (dots) is the cumulative fit using multiple Gaussian functions, as described in the text. It overlaps almost entirely with the raw data. The long dashed line shows peak of the undissociated dication derived from the fit.

### 5.2.2 The T1-T2 correlation maps

The time correlation maps between Hit1 and Hit2 of the CSD breakup of  $N_2^{++}$  and  $CO^{++}$  are shown in the Figure 5.4. In the T1–T2 correlation map of  $CO^{++}$ ,  $C^+$  ions appear as Hit1 and  $O^+$  appear as Hit2 with the centroid at ( $C^+ : 4.3 \mu s, O^+ : 4.95 \mu s$ ) of the island. For  $N_2$ , since fragmented ions are identical, their mean-TOF is same. Consequently, the  $z$ -momentum component of these ions will create the difference in their TOF values and decides which ion has larger TOF than the other and thus their appearance as Hit1 or Hit2. The additional effect in the correlation map of the  $N_2^{++}$  can be observed due to the identical mean-TOF of the fragmented ions is that the total extent of the island in the T1-T2 correlation map gets folded in half because of the nature of the plot where  $T1 \leq T2$  prevents the correlated events to appear in the lower diagonal.

As it has been discussed in the section 3.2 that the intensity of the island relates to the propensity of dissociation and the extent of the island reflects the distribution of the component of momentum of the ions along the spectrometer axis. (The

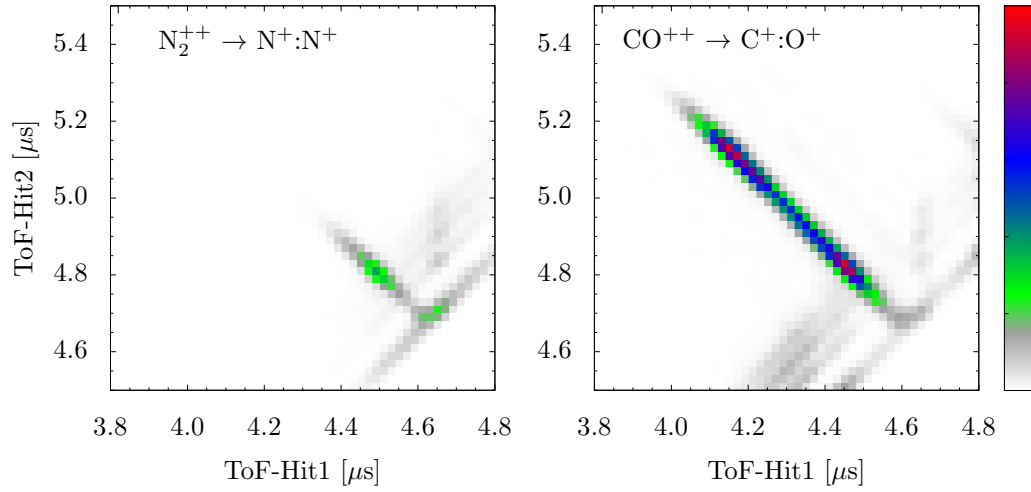


Figure 5.4: ToF Hit1–Hit2 correlation maps of the CSD channels  $N_2^{++} \rightarrow N^+:N^+$  and  $CO^{++} \rightarrow C^+:O^+$ . The intensity in the correlation maps are normalized to the respective counts of undissociated doubly-ionized molecular ions. The colour (intensity) scale is common to the two maps.

other components of momentum would be similarly distributed in the case of isotropic emission, and would show up in the  $x, y$  image on the detector.) In Figure 5.4, the correlation maps are normalized to the counts under the peaks of the non-dissociated dications, obtained from the fits in the TOF-Hit1 spectrum. The normalization is carried out after applying all corrections as discussed in section 5.2.3. It can be observed that the relative intensities in the correlation maps show that  $N_2^{++}$  is less likely to dissociate than  $CO^{++}$ .

### 5.2.3 Estimation of CSD-to-ND ratios

In order to estimate the CSD-to-ND ratio precisely, it is necessary to make accurate measurements of the counts of undissociated doubly ionized molecular ions (ND) of  $N_2^{++}$  and  $CO^{++}$  and of dications that dissociate via the CSD channel. The total counts of doubly ionized molecular ions (ND) is obtained from the first hit TOF spectrum shown in Figure 5.3. Because the peaks for both dications in TOF spectrum are mixed with broader peaks from fragment ions, accurate estimates are not easy. The  $CO^{++}$  peak lies on the overlapping tails of the  $C^+$  and  $O^+$  peaks, while the  $N_2^{++}$  peak lies over the broad  $N^+$  peak. To separate the contribution

of the undissociated dication from the peak, we note that the fragment ion peak results from a mixture of ions arising from a multitude of several precursor states, the width of the peak reflecting the kinetic energy distribution of the ions. The contribution from each state is approximated by a Gaussian function centered at the mean TOF, determined from the experiment. We carry out unconstrained fitting of each TOF spectrum in the region 3.0–6.0  $\mu\text{s}$  with Gaussian functions. Twelve Gaussian functions are used for the  $\text{N}_2$  spectrum and 18 for the CO spectrum. The residual error between fitted and experimental spectra in both spectrum is less than 4% at any point in the entire range considered. The fitted curves are shown by dotted lines in Figure 5.3. Amongst all Gaussian functions needed to fit the entire range of TOF under consideration, two very narrow Gaussians centered around the peak of the dications ( $\mu = 4.631 \mu\text{s}, \sigma = 0.0047 \mu\text{s}$ ) and ( $\mu = 4.637 \mu\text{s}, \sigma = 0.0122 \mu\text{s}$ ) with relative amplitudes 1:0.2 are common to both cases and their sum accounts for the undissociated molecular dications. (The TOF distributions of undissociated species would be very narrow, as the only kinetic energy they have is thermal.) The rest of the Gaussian functions correspond to the broader features due to dissociation. The sum of the two narrow Gaussians is taken to be the intensity of the undissociated dications. The robustness of the fit is established by the fact, that the TOF distributions of the *monocations*  $\text{N}_2^+$  and  $\text{CO}^+$  are similarly well-fitted by a pair of narrow Gaussian functions, ( $\mu = 6.556 \mu\text{s}, \sigma = 0.0072 \mu\text{s}$ ) and ( $\mu = 6.569, \sigma = 0.0243 \mu\text{s}$ ) also in the proportion 1:0.2, and this is common to the two species. Furthermore, the standard deviation of the fit for the monocations (comprising the sum of the two narrow Gaussians) is  $\sqrt{2}$  times the standard deviation of the fit for the dications (also comprising the sum of two narrow Gaussians). This is consistent with the fact that the TOF of singly-charged ions would be  $\sqrt{2}$  times the TOF of doubly-charged ions. In Figure 5.3, the TOF spectra are normalized in such a manner that the counts under the fitted  $\text{N}_2^{++}$  and  $\text{CO}^{++}$  peaks, representing ND counts, are equal. In unnormalized spectra, the common peak for  $\text{H}_2\text{O}^+$  would appear identical.

The CSD counts are obtained from the time correlation maps of CSD of  $\text{N}_2^{++}$  and  $\text{CO}^{++}$  shown in Figure 5.4. The CSD counts normalized by their corresponding

ND counts provide the CSD-to-ND ratios for the dications.

Further, to obtain the correct CSD-to-ND ratio, we need to correct the recorded experimental cross sections for the intrinsic detection efficiency of the detector as has been discussed in the section 3.4.3. At the applied front plate bias of  $-2800$  V, the detection efficiency for  $N_2^{++}$  and  $CO^{++}$  is 0.52, while for the singly charged ions  $C^+$ ,  $N^+$  and  $O^+$ , it is 0.50. These values have been taken from the report by Lienard *et. al.* [111]. The corrected counts of  $N_2^{++}$  and  $CO^{++}$  are thus obtained by dividing the observed counts by the corresponding efficiency. The observed counts from CSD need a correction for the detection efficiency for pair coincidence measurement. We take this factor to be the square of the singles counting efficiency, i.e. 0.25.

The observed number of ion pair counts requires further correction due to loss in transmitting the ions. Transmission loss arises due to two factors – finite size of the detector and finite strength of the extraction field. The nature of these loss factors and their properties for the RIMS has been discussed in the section 3.4.1 and 3.4.2. In case of CSD of  $N_2^{++}$ , loss starts from 9.70 eV KER and from 8.50 eV for  $CO^{++}$ . For CSD of  $CO^{++}$ , loss starts from relatively less KER value because although the momentum is shared equally in a two-body break-up process, the kinetic energy of  $C^+$  is higher than that of  $O^+$ , for a given KER. At 8.50 eV KER for dissociation of  $CO^{++}$ ,  $C^+$  ions attain 4.85 eV (the limiting energy for a single ion in the RIMS) energy and thus loss starts. The correction of the transmission loss can be implemented in the observed KER spectrum of the dications. The observed and transmission loss corrected KER spectrum of CSD of  $N_2^{++}$  and  $CO^{++}$  are shown in Figure 5.5 with dotted and continuous lines respectively. The counts of the CSD are taken from the corrected KER spectrum in the calculation of CSD-to-ND ratios. The consideration of the transmission loss increases the CSD cross section by about 30%. The loss because of the dead time (20 ns) of the multi-hit detection turns out to be very small and thus has been ignored. The loss is 0.5 % at 1 eV KER for CSD of  $N_2^{++}$ , and it decreases as square root of the energy (shown in the Figure 3.5).

After including all the corrections discussed above, the CSD-to-ND ratio for  $N_2^{++}$  is 0.07 and for  $CO^{++}$  it is 0.56. If the loss in transmission is not accounted for, the CSD-to-ND ratios would be incorrectly taken to be 0.04 and 0.38, respectively.

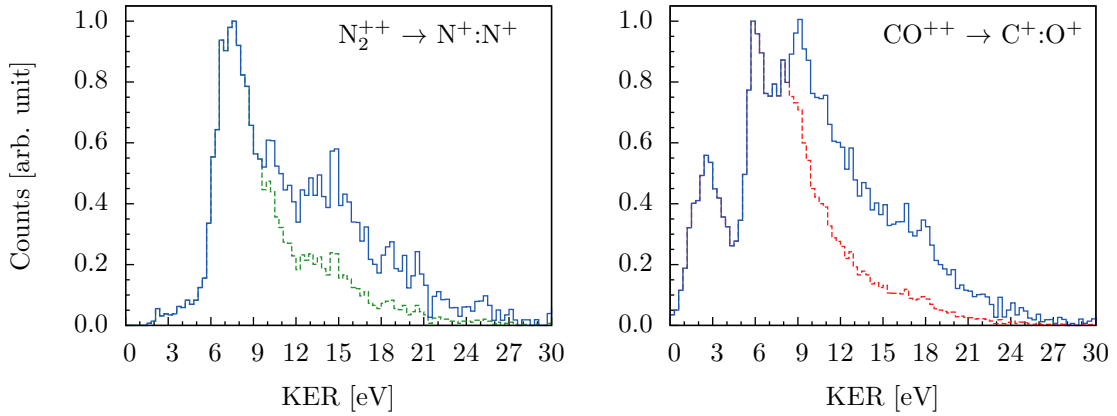


Figure 5.5: KER spectra of the CSD channel of  $N_2^{++}$  and  $CO^{++}$ . In both plots, the histogram shown with a broken line is the observed spectrum, whereas the KER spectrum after correction for losses is shown by the continuous line. Correction is applicable to the  $N_2^{++}$  spectrum from 9.70 eV onwards, and to the  $CO^{++}$  spectrum from 8.50 eV onwards.

#### 5.2.4 CSD-KER spectrum of $N_2$ and CO dications

The observed and the transmission loss corrected KER spectrum of the CSD of the  $N_2$  and CO dications are shown in the Figure 5.5. It can be observed that the transmission loss correction not only changes the CSD cross section significantly but also modifies the KER distribution itself, particularly at larger KER values. The details of the transmission loss has been discussed in the section 3.4.1. It is clear that the raw KER data can be quite misleading because of various inefficiencies and losses in the spectrometer. The KER spectra are plotted with bin size of 300 meV, that is the resolution of the RIMS for the two body break up channels. The estimation of the momentum and KER resolution of the RIMS has been derived in the section 2.8.

### 5.3 The computational results

The ab initio calculations are performed on the ground electronic state of neutral molecules and the PECs of the dications of  $N_2$  and CO. The computation of the vibrational levels, their tunneling life-times, their Franck-Condon (FC) factors and

the resulting KER values are also performed for the states supporting vibrational structures. The KER values arising from the repulsive states are also calculated. Details of the calculation are given in the following sections.

### 5.3.1 Calculation of Potential Energy Curves

The electronic states of  $N_2$  and CO and their singly- and doubly-charged molecular ions have been calculated under the BO approximation. All states are calculated using MOLPRO program package [136]. The complete active space self-consistent field (CASSCF) method and the multi-reference configuration interaction (MRCI) method have been used for the calculations using the standard correlation-consistent cc-pV5Z basis set. The CASSCF wave functions have been chosen to be of full-valence type, and have been used as the reference function in the subsequent MRCI calculation. These methods have been discussed in the section 4.3.5.

The electronic states of  $N_2$  and its molecular ions are calculated in the finite point group  $D_{2h}$ , while for CO the  $C_{2v}$  group is used. State-averaging has been employed in CASSCF calculations in order to allow for a balanced description of several electronic states of dications. The symmetry of the computed electronic states have been reassigned to the corresponding symmetry of full symmetry group, i.e.  $D_{\infty h}$  and  $C_{\infty v}$  for  $N_2$  and CO respectively. The atomic states of N,  $N^+$ , C,  $C^+$  and O,  $O^+$  have also calculated using same method and their relative energy levels has been cross-checked values reported with NIST database [142] and other ionization data[164].

Few potential energy curves (PECs) of doubly ionized molecular ions of  $N_2$  and CO are shown in Figures 5.6 and 5.7 respectively. These PECs are plotted relative to the lowest ground state vibrational level of their neutral parents,  $N_2[{}^1\Sigma_g^+, v=0]$  and CO [ ${}^1\Sigma^+, v=0$ ]. For the vertical excitation, the excitation energy for the ground state  ${}^1\Sigma_g^+$  of  $N_2^{++}$  is 42.49 eV. For  $CO^{++}$  ground state  ${}^1\Sigma^+$  it is 40.97 eV. These results are in agreement with the results of other theoretical and experimental investigations [151, 153].

In order to explain the dissociative ionization properties of these dications, their

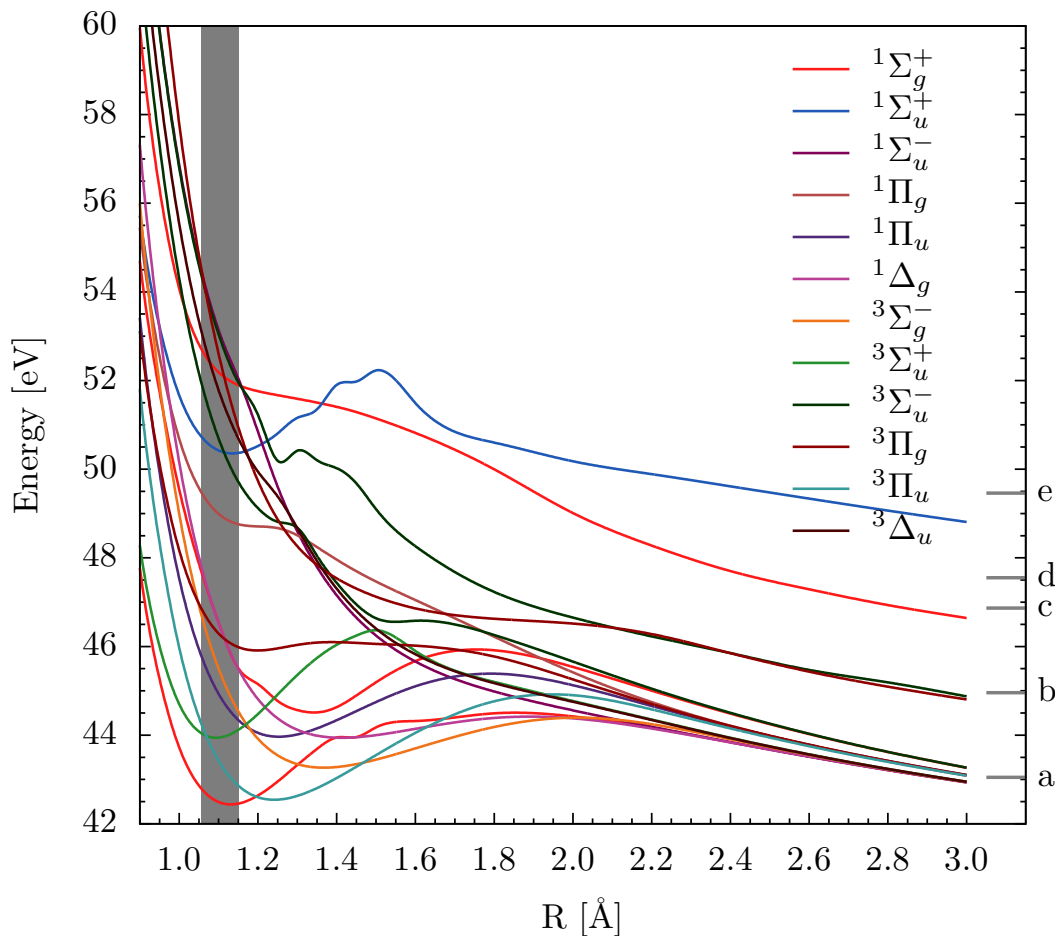


Figure 5.6: A few low-lying PECs of  $N_2^{++}$ , plotted with respect to the ground state of  $N_2$ ;  $1^1\Sigma_g^+, \nu = 0$ . FC region centered at  $1.103 \text{ \AA}$  is shown by vertical line. The values of the potential energy in the separated ion limit at  $3 \text{ \AA}$  for different CSD pathways of  $N_2^{++}$  are shown at the right edge: a( $^3P:^3P$ ) at  $43.05 \text{ eV}$ , b( $^3P:^1D$ ) at  $44.96 \text{ eV}$ , c( $^1D:^1D$ ) at  $46.86 \text{ eV}$ , d( $^3P:^1S$ ) at  $47.55 \text{ eV}$ , e( $^1D:^1S$ ) at  $49.46 \text{ eV}$ .

electronic Hamiltonian  $H_{elec}$  is solved for a set of internuclear distances  $\mathbf{R}$ , covering the range  $[0.80 \leq R \leq 3.00] \text{ \AA}$  at increment of  $0.20 \text{ \AA}$ . In order to capture the behaviour of PECs very precisely near the Franck Condon region centered around  $1.00 \text{ \AA}$ , electronic states in the range  $[0.90 \leq R \leq 1.50] \text{ \AA}$  are calculated with much smaller increment of  $0.05 \text{ \AA}$ . The PECs for the entire range are interpolated using cubic spline fitting. The largest internuclear separation  $R$  at which the calculation is performed is  $3 \text{ \AA}$ , since at this distance, the nature of PECs is almost entirely Coulombic and is appropriate for the identification of asymptotic limit. To identify the states of the separate atom (ion) limits of these dications, we match

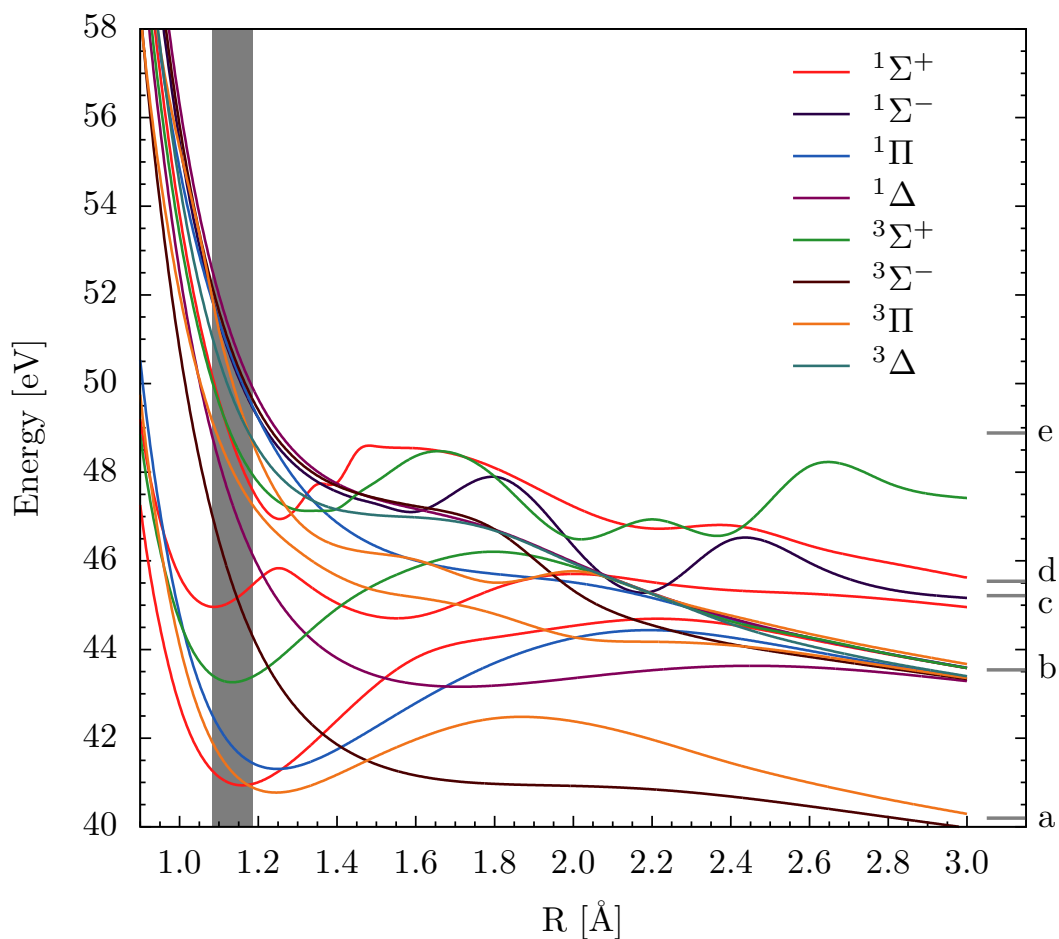


Figure 5.7: A few low-lying PECs of  $\text{CO}^{++}$ , plotted with respect to the ground state of  $\text{CO}$ ;  $1^1\Sigma^+, v = 0$ . FC region centered at  $1.135 \text{ \AA}$  is shown by vertical line. The values of the potential energy in the separated ion limit at  $3 \text{ \AA}$  for different CSD pathways of  $\text{CO}^{++}$  are shown at the right edge: a( $^2\text{P};^4\text{S}$ ) at  $40.20 \text{ eV}$ , b( $^2\text{P};^2\text{D}$ ) at  $43.54 \text{ eV}$ , c( $^2\text{P};^2\text{P}$ ) at  $45.21 \text{ eV}$ , d( $^4\text{P};^4\text{S}$ ) at  $45.54 \text{ eV}$ , e( $^4\text{P};^2\text{D}$ ) at  $48.88 \text{ eV}$ .

the potential energy given by the above curves to the value at the same  $R$  of a Coulombic energy function of two singly charged ions. The asymptotic function is taken to be  $E_a(i, j, R) = E_1^i + E_2^j + k/R$ , where  $E_1^i$  and  $E_2^j$  are the electronic energies of the separated fragments that are calculated separately. The value of the constant  $k$  is  $14.40$ , when energies are in  $\text{eV}$  and  $R$  in  $\text{\AA}$ .

### 5.3.2 Need of precise calculations

Although reasonably accurate PECs of some of the low-lying states of these molecules are available in literature, our work requires that we calculate more

number of states (atleast two for each symmetry). The high accuracy calculations of  $N_2^{++}$  are by Bennett [161] and Wu *et. al.* [144]. Bennett have used MRCI wavefunctions with cc-pV5Z basis sets, but report only five PECs that support vibrational states. Recently, Wu *et. al.* have calculated fifteen states (nine states supporting vibrational structure and six repulsive states) using MRCI calculations at the level of the cc-pV5Z basis set. However, since their calculation does not take into account the vibrational distribution, their reported KER values are not vibrationally resolved. Further, they have considered only one dissociation limit of  $N^+(^3P) + N^+(^3P)$ . The maximum KER in their calculation is from the repulsive  $1^1\Sigma_u^-$  state at 14.41 eV, which is inadequate to explain the source of the broad peak observed at 15 eV. In this study, we have calculated a larger number of states (40) going up to 20 eV above the double ionisation threshold.

For  $CO^{++}$ , most accurate calculations are by Sedivcova *et.al.* [163] and Eland *et.al.* [146] with similar accuracy. In order to understand life-times of meta-stable states, Sedivcova *et.al.*, provide nine low lying PECs of  $CO^{++}$ , seven of them supporting vibrational structure and two repulsive ones, calculated at MRCI level with cc-pVXZ [ $X = 5, 6$ ] atomic basis sets. Eland *et.al.* have reported calculation of seven low-lying states supporting vibrational levels using MRCI wavefunction and cc-pV5Z basis set. Among other works [96, 97, 162], Lablanquie *et.al.* have reported all  $CO^{++}$  states lying in the excitation range 35-60 eV. However, these calculations are only at CASSCF level with much smaller basis sets. Further, Lablanquie *et.al.* report  $^3\Pi$  state as ground state of  $CO^{++}$  as well as the lowest state for vertical excitation, whereas accurate calculations show  $^1\Sigma^+$  to be the lowest state for vertical excitation. High accuracy calculations are necessary for obtaining accurate KER values, since PECs are very steep in the FC region. In this work, we have calculated about 30 states, which is a more comprehensive calculation on  $CO^{++}$  compared to that available in the literature.

### 5.3.3 Calculation of FC Factors and tunneling life times

The FC region is calculated from the probability density distribution of the  $\nu = 0$  ground state of the neutrals. The FC region covering the  $3\sigma$  of the probability density distribution of the  $\nu = 0$  ground state for the ionizing transitions is shown by a shaded vertical region in Figures 5.6, 5.7. Vibrational states supported in the PECs of the dications of  $N_2$  and CO, their FC factors and tunneling life time has been computed using LEVEL8.0 codes [143]. A discussion about the computational details of the FC factors and tunneling life time has been covered in the section 4.1.4 and 4.3.6.

The vibrational levels having FC factor greater than  $10^{-3}$  of  $N_2^{++}$  and  $CO^{++}$  are shown in Figure 5.10. The details of vibrational levels of  $N_2^{++}$  and  $CO^{++}$  are given in the Appendix B.

### 5.3.4 Calculation of KER

The KER values for  $N_2^{++}$  and  $CO^{++}$  arising from the direct dissociation viz. from the repulsive PECs and vibrational levels of the PECs possessing minima are calculated employing the method discussed in the section 4.2.1. The calculation of KER resulting from the indirect processes are also calculated ( a discussion is provided in the section 4.2.2). The contribution arising because of the direct processes are plotted in the upper panel of the Figures 5.8 and 5.9. Also the various contributions in the KER distributions are discussed in the next section 5.4.

In addition to the calculation of specific KER values, the one more crucial point that has been taken into account while calculating the KER distribution is to account the probability of the states being accessed, which is specific to the perturbing agent. In the case of high energy electron impact, where there are no selection rules, the probability of excitation to a state at an energy  $\epsilon$  above the ground state is known to be [165] proportional to  $1/\epsilon^2$ . Hence, the amplitude of a particular transition contributing to the KER distribution is corrected by a factor proportional to  $1/\epsilon^2$ , the proportionality factor being different for the two dications. However, we have not attempted to fit a combination of the excitation functions at different

excitation energies to match the experimental KER distribution. The reason for not performing such exercise is that the exact excitation probabilities in the various transient states are not known. In addition, the observed intensities of the features in the KER, unless it has been confirmed to arise from a unique transient state, would not be proportional to the excitation probabilities of the states. In this work, we have focused on explaining the features in the distribution.

It can be seen in the Figures 5.8 and 5.9 that the computed KER values cover almost the entire range of KER observed in the experiment. The computed PECs cover up to 20 eV excitation above the double ionization threshold. We expect the contribution from even higher lying states to be less important based on two reasons. The first reason is that the excitation probability for the present collision system, as has been discussed above, decreases as an inverse square function of the excitation energy. So the higher lying states will be less populated in the collision with respect to lower lying states for a given charged species. The second reason is that, higher lying states will be mostly of repulsive nature and thus they will always lead to larger KER values, and contribute mainly to the tail of the KER distribution. It should be noted that the major features in the  $N_2^{++}$  as well as  $CO^{++}$  KER spectrum are below 22 eV, which we have been able to explain with the states we have computed.

## 5.4 Identification of the KER features

We first consider the features in the KER spectrum that can be achieved by assuming the direct dissociation. The remaining features in the KER spectrum can be understood only by considering the indirect dissociation channels and are discussed in the subsequent sections.

### 5.4.1 Direct dissociation channels

As it has been discussed in the section 4.2.1, the KER distribution for CSD via repulsive states of doubly-ionized molecular ions is obtained by reflecting the probability

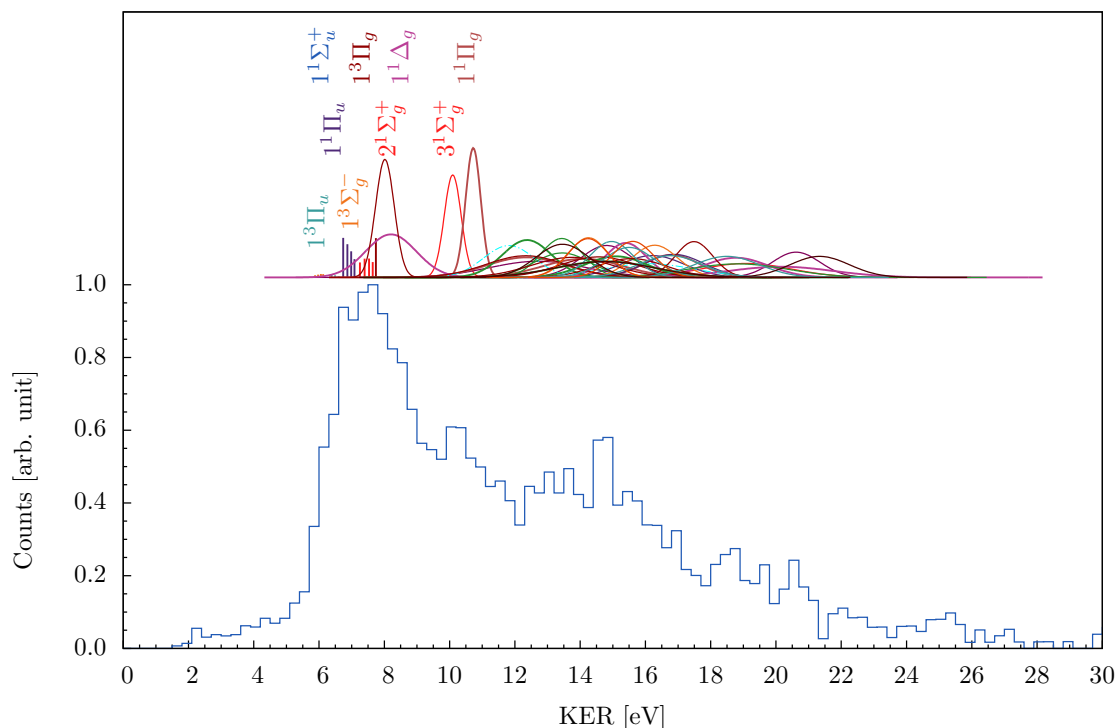


Figure 5.8: Experimental and theoretical KER distributions for the channel  $N_2^{++} \rightarrow N^+:N^+$ . Corrected experimental KER distribution shown by histogram in lower panel. Upper panel (offset by 1.05) shows the KER distribution arising from repulsive states of  $N_2^{++}$  (Gaussian curves) and the contribution from tunneling of vibrational levels (bars).

distribution of ground vibrational level of ground electronic state of neutral parent across the PEC in the FC region. The KER distribution corresponding to that PEC is then a Gaussian function whose area is proportional to the magnitude of the transition function which as described earlier varies as  $1/\epsilon^2$ . The experimental KER spectra and the computed contributions from different states (via direct channels) for the two dications appear in Figures 5.8 and 5.9.

Three categories of PECs are considered to explain the observed KER distributions by the direct processes of dissociation. The first category is of states that support vibrational levels and are relatively stable against tunneling. States of this category will not contribute to dissociation if only tunneling is responsible. The second category is of states that support some vibrational levels and have a propensity to tunneling. The third category is of states that are either purely

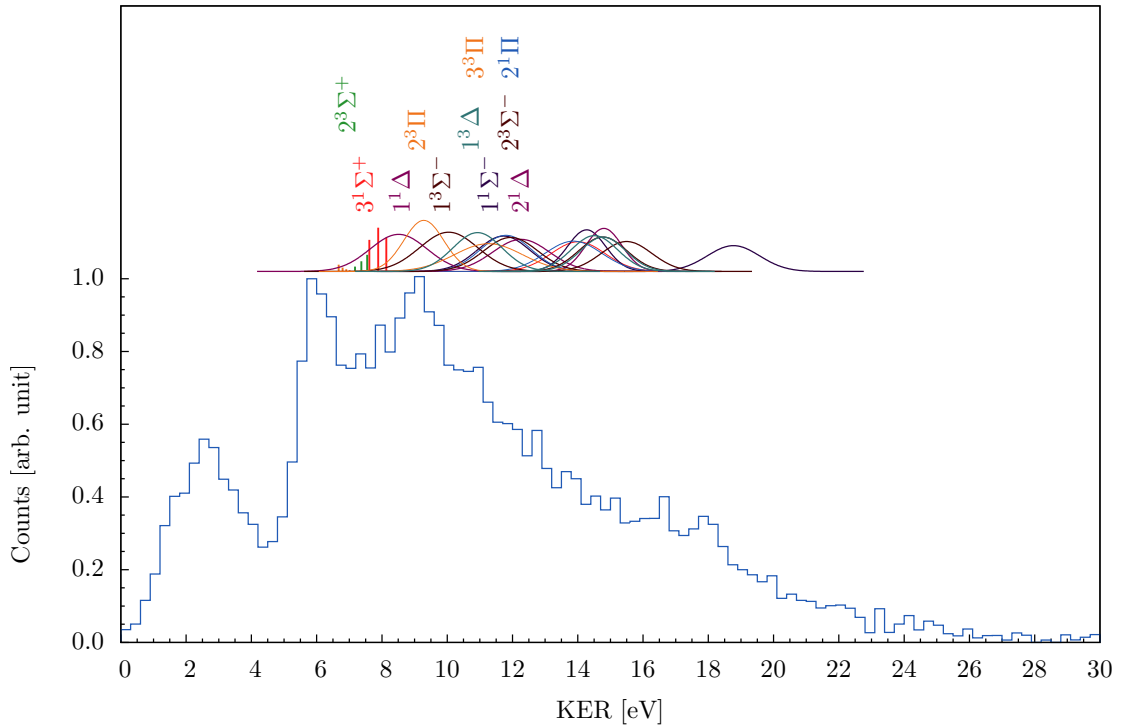


Figure 5.9: Experimental and theoretical KER distributions for the channel  $\text{CO}^{++} \rightarrow \text{C}^+:\text{O}^+$ . Corrected experimental KER distribution shown by histogram in lower panel. Upper panel (offset by 1.05) shows the KER distribution arising from repulsive states of  $\text{CO}^{++}$  (Gaussian curves) and the contribution from tunneling of vibrational levels (bars).

repulsive or support a few vibrational levels with relatively small FC factors ( $< 10^{-3}$ ) and decaying from the FC overlap region.

We first consider the case of  $\text{N}_2^{++}$ , referring to Figures 5.6 and 5.10 and Table 1 given in the Appendix B. The states  $1^1\Sigma_g^+$  and  $1^3\Sigma_u^+$  can be placed in the first category as their tunneling contributions are from higher vibrational levels with small FC factors. The states  $1^3\Pi_u$ ,  $1^1\Pi_u$ ,  $1^3\Sigma_g^-$ ,  $1^3\Pi_g$ ,  $2^1\Sigma_g^+$ ,  $1^1\Sigma_u^+$  fall in the second category. From Figure 5.10, it can be seen that the KER from tunneling vibrational levels of these electronic states ranges from about 6.0 eV (for  $1^3\Sigma_g^-$  state) up to 8.0 eV (for the  $1^3\Pi_g$  state). In fact, all meta-stable vibrational levels of these states have very small FC factors, the largest value being 0.1. These vibrational levels have life times of up to few milliseconds. If tunneling were the only decay mechanism, then only these states levels would contribute to the CSD channel.

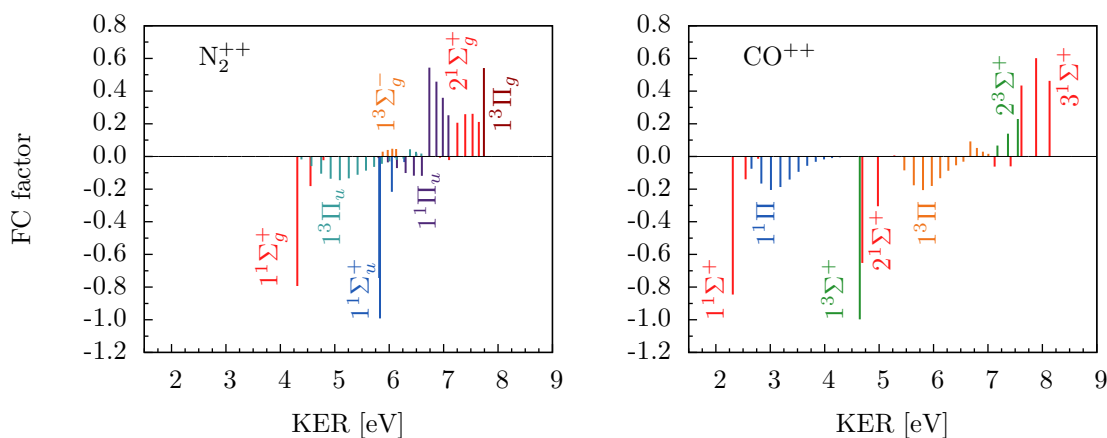


Figure 5.10: Vibrational levels of  $N_2^{++}$  and  $CO^{++}$  having FC factor greater than  $10^{-3}$  are shown with respect to the KER that would be obtained upon dissociation from this state. Each vibrational level is shown by a bar of height equal to the FC factor. The FC factors for vibrational levels which are found to be stable against tunneling are shown with negative sign. The positive FC factors have been multiplied by 5.0 to enhance their visibility.

Although the  $1^1\Delta_g$  state is deep enough to support five vibrational states, all of them have very small FC factors (because the minimum of that state is far from the FC region). This state crosses to several other electronic states having stable vibrational states and hence may indirectly contribute to KER.

The experimental KER distribution shows distinctive peaks around 6.5 eV, 7.5 eV, 10.0 eV and 15.0 eV. The electronic states responsible for the first two peaks are clearly the meta-stable states identified above. The peak around 10.0 eV can be attributed clearly to the repulsive states  $3^1\Sigma_g^+$  and  $1^1\Pi_g$ , giving rise to KER values centred at 10.01 eV and 10.72 eV. This is to be contrasted with the report of Lundqvist *et. al.* [47], who had tentatively assigned the broader KER structure at 10 eV to the purely repulsive  $1^1\Pi_g$  state. Lundqvist *et. al.* have observed the feature at 15 eV but have provided explanation for features only up to 12 eV, based on the calculations by Senekowitsch *et. al.* [160] and Olsson *et. al.* [159], the latter being limited in the number of PECs calculated. As shown in Figure 5.8, a large number of higher lying states which are purely repulsive in the FC region contribute to the KER distribution at higher energies. Since the state density in this range is very high, it is not possible to make an exact correspondence between

the state and the structures in the KER distribution beyond 11 eV. However, our calculations do predict a large number of states around a KER value of 15.0 eV, where the experimental spectrum also shows a prominent feature. It is interesting to note that this feature is hardly seen in the raw KER spectrum, emphasizing the importance of correcting the raw KER spectra for losses and inefficiencies of the spectrometer; this will be seen once again in the KER spectrum of CSD of  $\text{CO}^{++}$ .

Now, we consider CO and referring to Figures 5.7 and 5.10 and Table 2 given in the Appendix B. The states  $1^1\Sigma^+$ ,  $1^1\Pi$  and  $1^3\Sigma^+$  can be identified to belong to the first category. These have several stable vibrational levels and tunneling occurs only for levels that are very high. The FC factors for these high vibrational levels are very small. On the other hand,  $1^3\Pi$ ,  $2^1\Sigma^+$ ,  $3^1\Sigma^+$  and  $2^3\Sigma^+$  are in the second category. These states support vibrational levels which have modest FC factors (about 0.02 to 0.1) and dissociate through tunneling.

In contrast to  $\text{N}_2^{++}$ , the KER distribution for CSD of  $\text{CO}^{++}$  has a much richer structure. It has a relatively broad low-intensity peak at 2.8 eV which is well-separated from two narrower peaks at 6.0 eV and 9.5 eV. From Figure 5.10, it can be seen that the vibrational states with significant tunneling contribute to KER starting from 6.7 eV (for  $1^3\Pi$  state) up to 8.0 eV (for  $3^1\Sigma^+$  state). If only tunneling were the sole mechanism for dissociation, there would be no contribution from vibrational levels to KER values less than 6.7 eV. Therefore, the KER peaks at 2.8 and 6.0 eV cannot be explained without invoking indirect dissociation mechanisms. As shown in upper panel of Figure 5.9, at higher KER values beyond 8.6 eV only repulsive states contribute, starting with states  $1^1\Delta$  and  $2^3\Pi$ , readily explaining the KER peak at 9.5 eV.

### 5.4.2 Indirect dissociation channels

Apart from the direct dissociation pathways, two other dissociation mechanisms namely predissociation and autoionization which are termed as indirect processes need to be taken in to account in order to explain the rest of the features of the observed KER. These processes are discussed in the section 4.2.2. Since, in case of

$N_2$ , all the KER features can be explained with the KER distributions arising from the direct dissociation, we will not invoke the possibilities of indirect processes in this case. Only in case of CO, the two KER features at 2.8 and 6.0 eV are examined for the various possible indirect dissociation pathways. Finally, we present reasons for appearing the indirect processes in the CSD of  $CO^{++}$ .

From Figure 5.7, the states  $1^3\Sigma^-$ ,  $1^1\Delta$  and  $2^3\Pi$  are the possible candidates through which the low lying electronic states that also cross them ( belonging to first and second category) may undergo predissociation. Assuming weak coupling of crossing states, the vibrational levels closest to the crossing point will contribute significantly to predissociation. The FC factors of such vibrational levels pre-dissociating through  $1^1\Delta$  and  $2^3\Pi$  states are found to be insignificant (less than 0.005) and these levels are unlikely to be populated. The KER values for predissociation through different states are as follows.  $1^3\Sigma^-$ :  $1^1\Sigma^+$  6.56 eV and 6.78 eV,  $2^1\Sigma^+$ : 9.76 eV,  $1^1\Pi$ : 6.35 eV,  $1^3\Sigma^+$ : 8.24 eV,  $1^3\Pi$ : 6.12 eV. The FC factors are significant ( $> 0.1$ ) only for  $1^1\Pi$  and  $1^3\Pi$  states. Therefore, the KER peak at 6.0 eV will receive significant contributions from both of these states. Tarisien *et.al.* [97] have identified the origin of this peak to be the vibrational levels of  $1^3\Pi$  state; our calculated PECs enable us to clarify that this happens through strong predissociation of  $3\Pi$  and  $1\Pi$  states via repulsive  $3\Sigma^-$  state and not via tunneling.

Although predissociation from lower vibrational levels may contribute to KER below 6.0 eV (estimated lower limit is 2.3 eV), the couplings are not expected to be significant as these levels are far from the relevant crossing-points. Therefore, it is not possible to explain the KER peak at 2.8 eV on the basis of predissociation. A possible mechanism is dissociation from a highly-excited electronic state of singly-ionized  $CO^{+*}$  lying between the lowest CSD asymptote of  $CO^{++}$  and the double-ionization threshold of CO (the latter is about 5.5 eV above the former). Such a state, if accessed during electron-impact ionization, will be autoionizing and undergoes dissociation to the lowest CSD asymptote of  $CO^{++}$ . This possibility has been established by Hsieh and Eland [156] who report that the KER distribution arising purely from autoionization of  $CO^{+*}$  extends up to 4.7 eV KER. Their reported distribution is very similar to ours. This channel has been further investigated by

Osipov *et al.* [158], who have proposed that  $\text{CO}^{+*}$  first dissociates to  $\text{C}^+$  and  $\text{O}^*$ , followed by  $\text{O}^*$  autoionizing to  $\text{O}^+$ .

The main reasons for differences in the KER spectra of the two species can be understood qualitatively with the aid of the PECs shown in Figures 5.6 and 5.7. The crossing of the meta-stable states with repulsive states occurs at a much larger bond-distance from the FC region in  $\text{N}_2^{++}$  as compared to  $\text{CO}^{++}$ . In  $\text{N}_2^{++}$ , these crossings occur only beyond 1.5 Å, whereas in  $\text{CO}^{++}$ , several such crossings (with  $1^3\Sigma^-$  and  $1^1\Delta$  repulsive states) occur within 1.5 Å. Further, in  $\text{N}_2^{++}$ , most of the repulsive states involved in crossings are not effective because they dissociate to the same asymptote as the meta-stable states they cross with. In contrast, in  $\text{CO}^{++}$ , most meta-stable states (except  $1^3\Pi$ ) dissociate to a higher asymptote ( $\text{C}^+ : ^2\text{P}$  and  $\text{O}^+ : ^2\text{D}$ ), whereas the repulsive state  $1^3\Sigma^-$  which crosses with most of them dissociates to the lowest asymptote ( $\text{C}^+ : ^2\text{P}$  and  $\text{O}^+ : ^4\text{S}$ ). Since only triplet and quintet states are possible for the lowest asymptote in  $\text{CO}^{++}$ , all the singlet states necessarily dissociate into a higher asymptote. The calculations of spin-orbit interaction by Sedivcova *et al.* [163] show that in  $\text{CO}^{++}$ ,  $1^3\Sigma^-$  has strong coupling with  $1^1\Sigma^+$  and  $1^1\Pi$  states which are facile pre-dissociation channels.

## 5.5 Calculation of the partial cross sections

The experimental values of the CSD-to-ND ratios for  $\text{N}_2^{++}$  and  $\text{CO}^{++}$ , after applying all corrections, are 0.07 and 0.56, respectively. In the case of  $\text{CO}^{++}$ , both predissociation and autoionization contribute to CSD, which is evidently not the case for  $\text{N}_2^{++}$ . The contribution of the indirect processes in the CSD of  $\text{CO}^{++}$  can be realised by calculating the modified CSD-to-ND ratios and comparing with the observed CSD-to-ND ratio for  $\text{N}_2^{++}$ . The partial cross sections of the identified indirect processes of the  $\text{CO}^{++}$  is used to calculate the modified CSD-to-ND ratios. The estimated partial cross sections of the  $\text{CO}^{++}$  and  $\text{N}_2^{++}$  is plotted in the Figure 5.11.

If we exclude the contribution to CSD arising from autoionization by removing the counts in KER distribution up to 4.7 eV (region  $r_1$ ) and instead include those

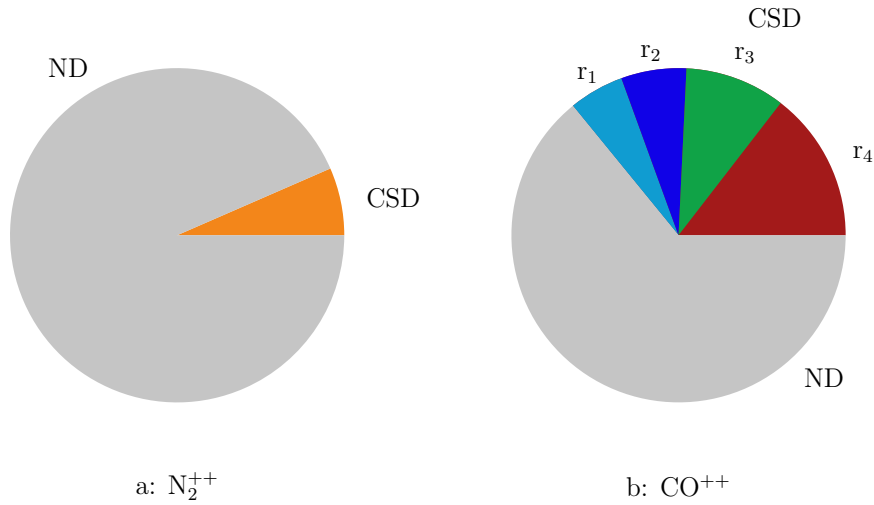


Figure 5.11: CSD and ND fractions of [a]  $N_2^{++}$  and [b]  $CO^{++}$  are shown in the figure. In case of  $CO^{++}$ , CSD yield is shown in four parts as discussed in the text. Region  $r_1$  represents CSD fraction corresponding to KER values below 4.7 eV. This region covers autoionization of high lying states of  $CO^{++}$ . CSD corresponding to the KER range from 4.7 to 7.2 eV largely arises from predissociation of  $1^1\Pi$  and  $1^3\Pi$  through  $1^3\Sigma^-$  and is shown as region  $r_2$ . Region  $r_3$  covers counts in the KER spectrum up to 10.8 eV, that can arise from all known possible predissociation and autoionization channels (for details, see text). Region  $r_4$  represents counts corresponding to KER value greater than 10.8 eV.

counts in the ND channel, the modified CSD-to-ND ratio becomes 0.44. Further, if predissociation of  $1^1\Pi$  and  $1^3\Pi$  through  $1^3\Sigma^-$  are separated collectively with the autoionization contribution by removing all counts from the KER distribution up to 7.2 eV (region  $r_1$  and  $r_2$ ) and instead considering them as non-dissociative, the CSD-to-ND ratio will become 0.32, that is again more than four times larger than  $N_2^{++}$  case. As seen earlier in the previous section, predissociation through  $1^3\Sigma^-$  can in fact contribute up to 9.8 eV and beyond. Even if we make the drastic assumption that all counts in KER distribution of  $CO^{++}$  up to 10.8 eV arise from predissociation and autoionization (region  $r_1$ ,  $r_2$  and  $r_3$ ) and exclude them from the CSD yield, though there will be a significant contribution in that KER range from repulsive curves, the CSD-to-ND ratio is 0.17. Even after accounting for the contributions of indirect dissociation process that could be identified in this study, the CSD-to-ND is higher in CO by a factor of 2. This shows that predissociation from higher lying states that will contribute in the KER spectrum above 9.8 eV are still significant.

Though, in the range above 9.8 eV, identification of KER features are not possible, the underlying mechanism is profoundly non-adiabatic, as in the lower KER range.

Since the total FC factors for these molecules are quite similar, we can assume that total number of dication molecules produced are roughly equal. Moreover, the total double ionization cross section for these molecules are nearly identical [108]. We can therefore estimate the ratio of total non-dissociative cross-sections of both dication as well as the ratio of their CSD cross-sections based on the observed CSD-to-ND ratios. The non-dissociative cross-section of  $N_2^{++}$  thus turns out to be 1.46 times that of  $CO^{++}$ , while the CSD cross-section of  $CO^{++}$  turns out to be more than 5 times that of  $N_2^{++}$ , which is also seen in Figure 5.11.

## 5.6 Conclusions

It can be observed from the analysis of CSD of  $N_2^{++}$  and  $CO^{++}$  that the KER spectrum of  $N_2^{++}$  can be readily explained in terms of repulsive or tunneling states, however in the case of  $CO^{++}$ , recourse has to be taken to indirect dissociation channels, namely predissociation and autoionization. In addition, the comparative study based on the CSD-to-ND ratios for these dications also suggests the significance of the indirect processes in the dissociation of  $CO^{++}$  dications.

By exploiting the information about the sources of the features in the KER spectra of the two species, we have been able to separate out the autoionization and predissociation contributions in the lower range of KER values to the overall dissociative yield. These indirect processes do not contribute as much to CSD in the case of  $N_2^{++}$  as they do in the case of  $CO^{++}$ , and this partially explains the higher CSD-to-ND ratio for  $CO^{++}$ . Since autoionization and curve-crossing predissociation processes fall under non-BO dynamics [123], our work shows that these processes play a significant role in the CSD of  $CO^{++}$ , but not much in the case of  $N_2^{++}$ , indicating the effect of asymmetry (presence of a non-zero dipole moment term) in non-BO dynamics [125].



# Chapter 6

## Summary and discussions

This thesis comprises a study on the small molecular systems focusing on their dissociation properties. The observed properties of dissociation are used as a tool to understand the dynamical nature of a molecular system that involves coupling of nuclear and electronic motions. In such studies, the major challenge arises because of the fact that dissociation processes generally involves many complex mechanisms that preclude any general understanding. In the absence of the possibility of a generalised understanding, we have taken an approach of comparative study of dissociative ionization of two (or more) molecular systems. In this thesis, we have presented a comparative study of the dissociative ionization of the dications of  $N_2$  and CO molecules.

Very extensive studies performed on molecular systems to investigate the dissociative ionization mechanisms have been reported in the literature. Processes that can be broadly categorized as following BO and non-BO dynamics have been investigated for many molecular systems under the influence of many ionizing elements. There has been an interest to quantify the participation of the various pathways of dissociation, however exact quantification is not possible in general. This is because of the fact that identification of the underlying causes is only possible on the basis of the energetics in the asymptotic limit of the dissociation and thus sources resulting in similar energetics can not be resolved. Recent advances in time resolved investigation of the dissociation mechanism are step towards separating

the multitude of dissociation pathways with similar energetics in the final states.

In this work, since the stress is on a comparative study, careful efforts have been taken in the experiments. In order to make direct comparison between the observed quantities, experiments on the molecules were performed in the identical conditions. In addition, we have accounted various loss factors and inefficiencies in the detection process in order to obtain the accurate cross sections. To the best of our knowledge, systematic analysis of the effect of transmission loss of the ions on the KER distributions of the CSD is being considered for the first time. We provide a way to calculate the accurate KER differential cross sections by recompensing the losses for two-body fragmentation. We have also noticed the effect of the losses on the anisotropy measurements and found that it is not possible to achieve accurate angular distribution of the fragmented ions in the presence of transmission loss. For the processes involving more than two-body fragmentation, difficulties in calculation of the losses have also been analyzed and reviewed.

Concurrently, to understand the features of the kinematics of dissociative ionization, we have performed theoretical calculations of the PECs of these dications and of their vibrational structures to determine their contribution in the dissociation. In this work, we provide the most exhaustive calculations for both dications that is also possibly the most accurate calculation reported in the literature for so many states. Because of the accurate calculation of the PECs, the sources of many features of the dissociation of these dications which were previously misidentified or uncertain are now resolved.

The most subtle aspect of the thesis which has been brought out is that it is possible to further identify and infer the contribution of various processes by a comparative study. Using the identified partial cross sections of the dissociation pathways, comparative study between the kinematics of two distinct molecular systems (or cases) enables us to make further quantification in the broad categories viz BO and non-BO mechanisms even though the identification of the sources of dissociation is elusive. The performed study also provides a way to see the effect of the inherent similarities and differences of the molecular systems on the properties of dissociative ionization.

After recognizing the importance, the comparative studies can be performed on the other molecular systems that share common features in their electronic structure with few differences. It is also necessary to perform comparative studies between molecules for different ionizing agents. It will provide the insight as to whether the dissociation process retains a memory of the excitation process that lead to the formation of the transient molecular ion. Studies monitoring the changes in the signatures of the dissociation for different ionizing elements have been performed for many small and large molecules, in many cases. Comparative study between molecules will provide more insight about the dynamical evolution of the dissociation.



# Appendix A

## Calculation of transmission loss

In order to estimate the transmission loss in the momentum spectrometer, a schematic diagram of the spectrometer and the Newton spheres representing the angular distribution of ions having different momentum, centred at the ideal point source (taken as the origin) are shown in Fig. A.1. The  $+z$ -axis is the spectrometer axis, along which extraction fields are applied. The detector plane is at  $z = s$ . The region between the source and the detector represent the extraction region.

Ions on a given Newton sphere of radius  $P$ , will have a range of flight times distributed around a value  $t_0$  corresponding to the flight time of ions created in  $z = 0$  plane on the Newton sphere. We have seen in the section 2.7, the TOF of ion gives the longitudinal momentum  $P_{||}$  and the position information,  $(X, Y)$  on the detector plane provides the two transverse momentum components  $(P_x, P_y)$  that defines the transverse momentum  $P_{\perp}$ . The distribution of the intensity on the detector plane, shown in the Figure A.1 by shaded the area, is for an isotropic Newton sphere and has been discussed by Amitay *et. al.* [166]. Nature of the transmission loss with ion's energy (or momentum) can be prevised by noticing the fact that the projection of the Newton sphere on the detector plane has its maximum at  $\theta = \pi/2$  and decreases rapidly for smaller  $\theta$ .

An ion formed in the ionization region will be detected only when  $P_{\perp} \leq R \times m/t$ , where  $R$  is the active radius of the detector. Corresponding to the limiting value  $P_{\perp lim}$  beyond which loss starts, is an angle  $\alpha = \cos^{-1}(P_{\perp lim}/P)$ , Figure A.1, which

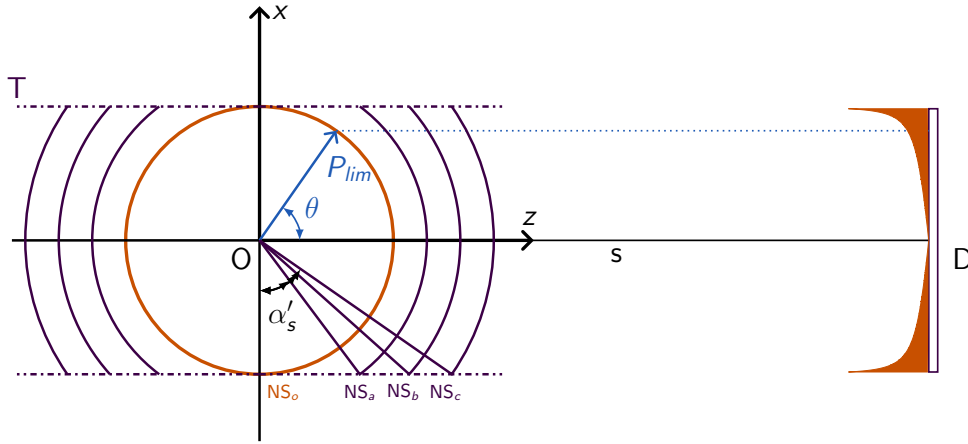


Figure A.1: A cross sectional view of Newton sphere,  $NS_o$  of radius  $P_{lim}$ , centered at  $O$  is shown in the  $y$ -plane. Three other Newton spheres,  $NS_a, NS_b, NS_c$  corresponding to momentum greater than  $P_{lim}$  are shown truncated. Only the part of the Newton spheres shown here will be within detector size upon transportation, the remaining part will not be detected. The lost part of the Newton spheres is parametrized by  $\alpha$ , the complement of the polar angle made by the radius vector at the point of intersection of the Newton sphere with the tangent (T)  $x = P_{\perp lim}$ .  $s$  is the distance between the ionization region and the detector D.  $\theta$  is the polar angle defined with respect to spectrometer ( $z$ -)axis. The projection of the Newton sphere,  $NS_o$  is shown by the shaded area on the detector. For simplicity, the conversion factor from momentum space to the distance is taken to be unity, and thus the range of the projection on the detector plane is shown having same radius as of the Newton sphere.

parametrizes the lost part of the Newton sphere. The solid angle corresponding to the portion of the Newton sphere that will fall outside the detector is  $4\pi \sin(\alpha)$ . So the loss factor for isotropic emission of particles is

$$LF(P) = \sin(\cos^{-1}(P_{\perp lim}/P)) \quad (A.1)$$

For the anisotropic case, if function  $f(\theta, P) : 0 < \theta < \pi$  represents the anisotropy of Newton sphere of radius  $P$ , then the loss factor for the momentum  $P$  will be given by

$$LF(P) = \frac{\int_{\pi/2-\alpha}^{\pi/2+\alpha} f(\theta, P) \sin(\theta) d\theta}{\int_0^{\pi} f(\theta, P) \sin(\theta) d\theta}. \quad (A.2)$$

Note that in Eq. A.2  $\theta$  is defined with respect to the spectrometer axis to simplify the expressions. If the Newton sphere has anisotropy about some axis (e.g. the projectile beam), the function  $f(\theta, P)$  must be defined accordingly.

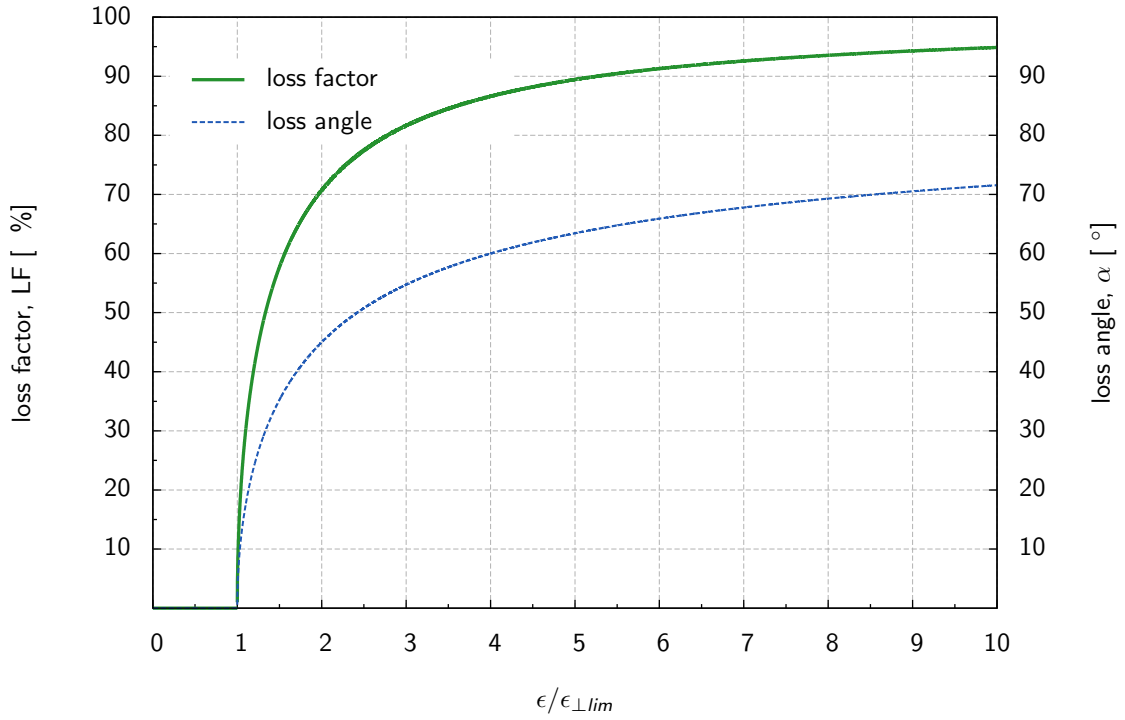


Figure A.2: Loss angle and loss factor for an ion are shown as a function of multiples of  $\epsilon_{\perp lim}$ . There will be no transmission loss for Newton spheres having radius less than  $\epsilon_{\perp lim}$ .

In terms of particle's kinetic energy  $\epsilon$ , if  $\epsilon_{\perp lim}$  ( $= P_{\perp lim}^2/2m$ ) represent the limiting kinetic energy of the ion, the loss factor for isotropic distribution will be

$$LF(\epsilon) = (1 - \epsilon_{\perp lim}/\epsilon)^{1/2} \quad (\text{A.3})$$

The loss angle and loss factor as a function of the particle's energy are plotted in the Figure A.2.

For RIMS setup, discussed in the section 2.5.4, the active area of the ion-MCP is 76 mm. Since in the transverse direction, there is no applied field, the limiting kinetic energy [or momentum]  $\epsilon_{\perp lim}$  [ or  $P_{\perp lim}$ ] depends only on the TOF of the ions for a given diameter of the ion detector. For singly-, doubly- ionized ions the  $\epsilon_{\perp lim}$  for the RIMS setup operated at 60 V/cm turns out to be 4.85 eV, 9.70 eV respectively.



## Appendix B

### Vibrational levels of $\text{N}_2^{++}$ and $\text{CO}^{++}$

Few PECs of dications of  $\text{N}_2$  and  $\text{CO}$  are listed in the tables B.1 and B.2. Only the states supporting vibrational structure and few low-lying states are provided. The total number of states calculated for these dications is very large covering about 20 eV above the double ionisation threshold, their resulting KER distributions are shown in the upper panel of the Figures 5.8 and 5.9.

In the context of the properties of dissociation, few points can be noted using the states shown in the tables B.1 and B.2. It can be observed that the states of  $\text{N}_2^{++}$  which support vibrational structures are predominantly decaying to the first asymptotic limit. In case of  $\text{CO}^{++}$ , the second asymptotic limit is the dominant to receive products of the dissociation. In addition, for states of  $\text{N}_2^{++}$  which support vibrational structures, crossing of the state happens largely with the other states that having a local minima. On the other hand, for  $\text{CO}^{++}$ , crossing of the stable states also happen to be with the purely repulsive states. It is also important to mention that the tunneling from the vibrational levels of these dications yield KER below 8 eV. However, the repulsive states will result mean KER values above 8 eV. Predissociation of the states can only increase the KER value from their direct dissociation values, and thus below the 8 eV there will no appearance of predissociation in the KER spectrum. The details of the identification of the features in KER spectrum of CSD of  $\text{N}_2^{++}$  and  $\text{CO}^{++}$  are given in the section 5.4.

Label	Electronic states	$T_{R_e}$ [eV]	$T_{0^v}$ [eV]	Asymptotic limit	$R_e^v$ [Å]	Crosses to	$N_{vib}$	Levels having FC > $10^{-3}$	tunneling starts from	KER [eV]
S <sub>1</sub>	$1^1\Sigma_g^+$	42.49	42.56	a	1.131	S <sub>2</sub> ,S <sub>5</sub> ,S <sub>7</sub>	13	$\nu = 0 \dots 3$	$\nu = 9$	6.04–6.25
S <sub>2</sub>	$1^3\Pi_u$	43.42	42.64	a	1.241	S <sub>1</sub> ,S <sub>5</sub> ,S <sub>7</sub>	16	$\nu = 0 \dots 15$	$\nu = 13$	6.38–6.59
S <sub>3</sub>	$1^3\Sigma_u^+$	43.94	44.08	a	1.093	S <sub>2</sub> ,S <sub>4</sub> ,S <sub>5</sub> , S <sub>7</sub> ,S <sub>8</sub> ,S <sub>6</sub>	11	$\nu = 0 \dots 1$	$\nu = 6$	7.34–8.08
S <sub>4</sub>	$1^1\Pi_u$	44.93	44.05	a	1.253	S <sub>3</sub> ,S <sub>5</sub> ,S <sub>7</sub>	10	$\nu = 0 \dots 9$	$\nu = 6$	6.74–7.09
S <sub>5</sub>	$1^3\Sigma_g^-$	45.49	43.33	a	1.368	S <sub>4</sub> ,S <sub>3</sub> ,S <sub>1</sub> , S <sub>2</sub>	11	$\nu = 4 \dots 10$	$\nu = 7$	5.88–6.13
S <sub>6</sub>	$1^3\Pi_g$	46.29	45.99	a	1.200	S <sub>7</sub> ,S <sub>8</sub> ,S <sub>3</sub>	1	$\nu = 0$	$\nu = 0$	7.74
S <sub>7</sub>	$1^1\Delta_g$	46.52	43.99	a	1.413	S <sub>6</sub> ,S <sub>8</sub> ,S <sub>3</sub> ,S <sub>4</sub> ,S <sub>1</sub> ,S <sub>2</sub>	5	none	$\nu = 2$	5.95–6.11
S <sub>8</sub>	$2^1\Sigma_g^+$	46.53	44.61	a	1.342	S <sub>6</sub> ,S <sub>7</sub> ,S <sub>3</sub>	9	$\nu = 2 \dots 8$	$\nu = 5$	7.25–7.65
S <sub>9</sub>	$1^1\Sigma_u^+$	50.42	50.48	e	1.135	many	9	$\nu = 0 \dots 3$	$\nu = 3$	6.50–7.44
R <sub>1</sub>	$1^1\Pi_g$	48.99		a			none			10.72±0.23
R <sub>2</sub>	$2^3\Sigma_u^+$	50.68		a			none			12.37±0.75
R <sub>3</sub>	$1^3\Delta_u$	51.78		a			none			13.46±0.81
R <sub>4</sub>	$3^1\Sigma_g^+$	52.18		c			none			10.01±0.26
R <sub>5</sub>	$2^3\Pi_g$	52.59		b			none			12.33±1.21
R <sub>6</sub>	$1^3\Sigma_u^-$	53.04		b			none			12.81±0.82
R <sub>7</sub>	$1^1\Sigma_u^-$	53.13		a			none			14.81±0.80

Table B.1: Electronic states of  $N_2^{++}$  (all states supporting vibrational structure,  $S_n$ , and few low lying repulsive states,  $R_n$ ) and their properties in the order of their excitation energy.  $T_{R_e}$  is the excitation energy for the vertical transition at  $R_e = 1.103\text{Å}$  with respect to ground state of  $N_2$ ,  $1^1\Sigma_g^+$ ,  $\nu = 0$ .  $T_{0^v}$  is the energy difference between  $N_2$   $1^1\Sigma_g^+$ ,  $\nu = 0$  level and the ground vibrational level of an upper PEC. Asymptotic limits: a( $^3P$ : $^3P$ ) at 38.25 eV, b( $^3P$ : $^1D$ ) at 40.16 eV, c( $^1D$ : $^1D$ ) at 42.07 eV, d( $^3P$ : $^1S$ ) at 42.75 eV, e( $^1D$ : $^1S$ ) at 44.66 eV, are calculated at infinite separation of the nuclei  $N^+$  and  $N^+$ . Crossing with other stable and repulsive states are shown in ‘Crosses to’ column in ascending order of internuclear separation. Total number of vibrational levels ( $N_{vib}$ ) for the PEC is given in the next column. Only vibrational levels having FC factor >  $10^{-3}$  are assumed to have any contribution to excitation, as the largest FC factors are of the order of 1. Tunneling is taken to be effective for a vibrational level having tunneling lifetime less than a few ms. For electronic states supporting vibrational levels, KER values are given for the vibrational level from which tunneling starts and for the highest vibrational level. For repulsive states, the KER is shown as the mean KER corresponding to the difference of  $T_{R_e}$  and the asymptotic limit and the width corresponding to the mapping of the ground state vibrational probability distribution through the repulsive PEC.

Label	Electronic states	$T_{R_e}$ [eV]	$T_{0^r}$ [eV]	Asymptotic limit	$R_e^r$ [Å]	Crosses to	$N_{vib}$	Levels having FC > $10^{-3}$	tunneling starts from	KER [eV]
S <sub>1</sub>	1 <sup>1</sup> Σ <sup>+</sup>	40.97	41.05	b	1.160	S <sub>2</sub> ,S <sub>3</sub> ,R <sub>1</sub> ,S <sub>6</sub> ,R <sub>2</sub>	24	$v = 0 \dots 3$	$v = 19$	5.66–5.93
S <sub>2</sub>	1 <sup>3</sup> Π	41.26	40.86	a	1.246	S <sub>1</sub> ,R <sub>1</sub>	12	$v = 0 \dots 11$	$v = 8$	6.68–7.01
S <sub>3</sub>	1 <sup>1</sup> Π	41.84	41.40	b	1.249	S <sub>1</sub> ,R <sub>1</sub> ,S <sub>6</sub> ,R <sub>2</sub>	23	$v = 0 \dots 12$	$v = 19$	5.37–5.63
S <sub>4</sub>	1 <sup>3</sup> Σ <sup>+</sup>	43.26	43.39	b	1.133	R <sub>1</sub> ,S <sub>6</sub> ,S <sub>5</sub> ,R <sub>2</sub>	16	$v = 0 \dots 1$	$v = 12$	7.06–7.41
S <sub>5</sub>	2 <sup>1</sup> Σ <sup>+</sup>	45.08	44.77	c	1.087	R <sub>1</sub> ,S <sub>6</sub> ,S <sub>4</sub> ,R <sub>2</sub>	11	$v = 3, 6, 10$	$v = 7$	4.99–5.19
S <sub>6</sub>	1 <sup>1</sup> Δ	47.35	43.19	b	1.714	S <sub>5</sub> ,S <sub>4</sub> ,S <sub>1</sub> ,S <sub>3</sub>	8	none	$v = 4$	4.70–4.86
S <sub>7</sub>	3 <sup>1</sup> Σ <sup>+</sup>	48.74	46.77	c	1.254	many	6	$v = 1 \dots 5$	$v = 3$	7.61–8.13
S <sub>8</sub>	2 <sup>3</sup> Σ <sup>+</sup>	48.84	46.59	c	1.369	many	22	$v = 10 \dots 18$	$v = 12$	7.15–7.81
S <sub>9</sub>	3 <sup>3</sup> Π	50.12	45.58	b	1.808	many	2	none	$v = 0$	6.84–6.97
S <sub>10</sub>	1 <sup>1</sup> Σ <sup>-</sup>	50.55	45.40	b	1.587	many	6	none	$v = 2$	7.09–7.66
R <sub>1</sub>	1 <sup>3</sup> Σ <sup>-</sup>	45.54		a			none			10.05±0.89
R <sub>2</sub>	2 <sup>3</sup> Π	48.09		b			none			9.28±0.61
R <sub>3</sub>	1 <sup>3</sup> Δ	49.75		b			none			10.93±0.75
R <sub>4</sub>	2 <sup>1</sup> Π	50.63		b			none			11.80±0.78
R <sub>5</sub>	2 <sup>3</sup> Σ <sup>-</sup>	50.78		b			none			11.95±0.83
R <sub>6</sub>	2 <sup>1</sup> Δ	51.10		b			none			12.26±0.86

Table B.2: Electronic states of CO<sup>++</sup> (all states supporting vibrational structure, S<sub>n</sub>, and few low lying repulsive states, R<sub>n</sub>) and their properties in the order of their excitation energy. The nomenclature for parameters is same as in Table B.1. Parameters specific to CO<sup>++</sup> are  $R_e = 1.135$  Å and the asymptotic limits: a(<sup>2</sup>P:<sup>4</sup>S) at 35.40 eV, b(<sup>2</sup>P:<sup>2</sup>D) at 38.74 eV, c(<sup>2</sup>P:<sup>2</sup>P) at 40.41 eV, d(<sup>4</sup>P:<sup>4</sup>S) at 40.74 eV, e(<sup>4</sup>P:<sup>2</sup>D) at 44.08 eV. Asymptotic limits,  $T_{R_e}$ ,  $T_{0^r}$  and KER are calculated with respect to the ground state of CO 1<sup>1</sup>Σ<sup>+</sup>,  $v = 0$ .



# Bibliography

- [1] M. Jammer, *The conceptual development of quantum mechanics* (McGraw-Hill New York, 1966).
- [2] G. Gamow, *Thirty years that shook physics: The story of quantum theory* (Courier Dover Publications, 1966).
- [3] B. L. Waerden, *Sources of quantum mechanics*, Vol. 5 (Courier Dover Publications, 1968).
- [4] H. Kragh, *Quantum generations: a history of physics in the twentieth century* (Princeton University Press, 2002).
- [5] J. Schwinger, *Quantum Kinematics And Dynamic* (Westview Press, 2000, 1970).
- [6] W. R. Johnson, *Atomic Structure Theory* (Springer, 2007).
- [7] I. Lindgren and J. Morrison, *Atomic many-body theory; 2nd ed.*, Springer Series on Atoms+Plasmas (Springer, Berlin, 1986).
- [8] M. Born and R. Oppenheimer, *Annalen der Physik* **389**, 457 (1927).
- [9] M. Baer, *Beyond Born-Oppenheimer: electronic nonadiabatic coupling terms and conical intersections* (John Wiley & Sons, 2006).
- [10] G. A. Worth and L. S. Cederbaum, *Annu. Rev. Phys. Chem.* **55**, 127 (2004).
- [11] R. L. Whetten, G. S. Ezra, and E. R. Grant, *Annual Review of Physical Chemistry* **36**, 277 (1985).

- [12] M. H. Alexander, G. Capecchi, and H.-J. Werner, *Science* **296**, 715 (2002).
- [13] A. W. Jasper, S. Nangia, C. Zhu, and D. G. Truhlar, *Accounts of chemical research* **39**, 101 (2006).
- [14] E. A. Hylleraas, *Zeitschrift für Physik* **48**, 469 (1928).
- [15] D. R. Hartree, in *Mathematical Proceedings of the Cambridge Philosophical Society*, Vol. 24 (Cambridge Univ Press, 1928) pp. 89–110.
- [16] D. R. Hartree, in *Mathematical Proceedings of the Cambridge Philosophical Society*, Vol. 24 (Cambridge Univ Press, 1928) pp. 111–132.
- [17] D. Hartree, in *Mathematical Proceedings of the Cambridge Philosophical Society*, Vol. 24 (Cambridge Univ Press, 1928) pp. 426–437.
- [18] W. Heitler and F. London, *Zeitschrift für Physik* **44**, 455 (1927).
- [19] C. C. J. Roothaan, *Rev. Mod. Phys.* **23**, 69 (1951).
- [20] V. Staemmler, *Computational Nanoscience: Do It Yourself* **31**, 1 (2006).
- [21] M. W. Schmidt and M. S. Gordon, *Annual review of physical chemistry* **49**, 233 (1998).
- [22] R. J. Bartlett and M. Musiał, *Rev. Mod. Phys.* **79**, 291 (2007).
- [23] A. Szabo and N. S. Ostlund, *Modern quantum chemistry: introduction to advanced electronic structure theory* (Courier Dover Publications, 2012).
- [24] I. N. Levine, *Quantum chemistry*, Vol. 5 (Prentice Hall Upper Saddle River, NJ, 2000).
- [25] H. D. Hagstrum, *Rev. Mod. Phys.* **23**, 185 (1951).
- [26] L. J. Kieffer and G. H. Dunn, *Rev. Mod. Phys.* **38**, 1 (1966).
- [27] C. J. Powell, *Rev. Mod. Phys.* **48**, 33 (1976).

- [28] V. Abrosimov, Y. Gordeev, M. Panov, and N. Fedorenko, *Sov. Phys. Tech* **9**, 1248 (1965).
- [29] E. Everhart and Q. C. Kessel, *Phys. Rev. Lett.* **14**, 247 (1965).
- [30] Q. C. Kessel and E. Everhart, *Phys. Rev.* **146**, 16 (1966).
- [31] J. W. McConkey, A. Crowe, and M. A. Hender, *Phys. Rev. Lett.* **29**, 1 (1972).
- [32] H. Ehrhardt, M. Schulz, T. Tekaas, and K. Willmann, *Phys. Rev. Lett.* **22**, 89 (1969).
- [33] M. A. Coplan, J. H. Moore, and J. P. Doering, *Rev. Mod. Phys.* **66**, 985 (1994).
- [34] A. Lahmam-Bennani, C. Dupré, and A. Duguet, *Phys. Rev. Lett.* **63**, 1582 (1989).
- [35] O. Schwarzkopf, B. Krässig, J. Elmiger, and V. Schmidt, *Phys. Rev. Lett.* **70**, 3008 (1993).
- [36] K. E. McCulloh, T. E. Sharp, and H. M. Rosenstock, *The Journal of Chemical Physics* **42**, 3501 (1965).
- [37] J. Eland, F. Wort, P. Lablanquie, and I. Nenner, *Zeitschrift für Physik D Atoms, Molecules and Clusters* **4**, 31 (1986).
- [38] J. Eland and C. Ng, "Vacuum ultraviolet photoionization and photodissociation of molecules and clusters," (1991).
- [39] D. Curtis and J. Eland, *International journal of mass spectrometry and ion processes* **63**, 241 (1985).
- [40] L. Frasinski, M. Stankiewicz, K. Randall, P. Hatherly, and K. Codling, *Journal of Physics B: Atomic and Molecular Physics* **19**, L819 (1986).
- [41] M. Stankiewicz, P. Hatherly, L. Frasinski, K. Codling, and D. Holland, *Journal of Physics B: Atomic, Molecular and Optical Physics* **22**, 21 (1989).

- [42] J. Eland, D. Mathur, and A. Brenton, *Rapid communications in mass spectrometry* **5**, 475 (1991).
- [43] B. Brehm and G. De Frenes, *International Journal of Mass Spectrometry and Ion Physics* **26**, 251 (1978).
- [44] A. K. Edwards and R. M. Wood, *The Journal of Chemical Physics* **76**, 2938 (1982).
- [45] F. Feldmeier, H. Durchholz, and A. Hofmann, *The Journal of Chemical Physics* **79**, 3789 (1983).
- [46] H. Cho and S. H. Lee, *Phys. Rev. A* **48**, 2468 (1993).
- [47] M. Lundqvist, D. Edvardsson, P. Baltzer, and B. Wannberg, *Journal of Physics B: Atomic, Molecular and Optical Physics* **29**, 1489 (1996).
- [48] J. Ullrich and H. Schmidt-Böcking, *Physics Letters A* **125**, 193 (1987).
- [49] J. Ullrich, H. Schmidt-Böcking, and C. Kelbch, *Nuclear Instruments and Methods in Physics Research Section A: Accelerators, Spectrometers, Detectors and Associated Equipment* **268**, 216 (1988).
- [50] R. Ali, V. Frohne, C. L. Cocke, M. Stockli, S. Cheng, and M. L. A. Raphaelian, *Phys. Rev. Lett.* **69**, 2491 (1992).
- [51] V. Frohne, S. Cheng, R. Ali, M. Raphaelian, C. L. Cocke, and R. E. Olson, *Phys. Rev. Lett.* **71**, 696 (1993).
- [52] R. Dörner, J. Ullrich, R. E. Olson, O. Jagutzki, and H. Schmidt-Böcking, *Phys. Rev. A* **47**, 3845 (1993).
- [53] R. Moshhammer, M. Unverzagt, W. Schmitt, J. Ullrich, and H. Schmidt-Böcking, *Nuclear Instruments and Methods in Physics Research Section B: Beam Interactions with Materials and Atoms* **108**, 425 (1996).

- [54] R. Moshhammer, J. Ullrich, H. Kollmus, W. Schmitt, M. Unverzagt, O. Jagutzki, V. Mergel, H. Schmidt-Böcking, R. Mann, C. J. Woods, and R. E. Olson, *Phys. Rev. Lett.* **77**, 1242 (1996).
- [55] R. Moshhammer, J. Ullrich, H. Kollmus, W. Schmitt, M. Unverzagt, H. Schmidt-Böcking, C. J. Wood, and R. E. Olson, *Phys. Rev. A* **56**, 1351 (1997).
- [56] B. Bapat, R. Moshhammer, S. Keller, W. Schmitt, A. Cassimi, L. Adoui, H. Kollmus, R. Dörner, T. Weber, K. Khayyat, *et al.*, *Journal of Physics B: Atomic, Molecular and Optical Physics* **32**, 1859 (1999).
- [57] L. Spielberger, O. Jagutzki, R. Dörner, J. Ullrich, U. Meyer, V. Mergel, M. Unverzagt, M. Damrau, T. Vogt, I. Ali, K. Khayyat, D. Bahr, H. G. Schmidt, R. Frahm, and H. Schmidt-Böcking, *Phys. Rev. Lett.* **74**, 4615 (1995).
- [58] R. Dörner, J. M. Feagin, C. L. Cocke, H. Bräuning, O. Jagutzki, M. Jung, E. P. Kanter, H. Khemliche, S. Kravis, V. Mergel, M. H. Prior, H. Schmidt-Böcking, L. Spielberger, J. Ullrich, M. Unverzagt, and T. Vogt, *Phys. Rev. Lett.* **77**, 1024 (1996).
- [59] B. Siegmann, U. Werner, Z. Kaliman, Z. Roller-Lutz, N. M. Kabachnik, and H. O. Lutz, *Phys. Rev. A* **66**, 052701 (2002).
- [60] M. Takahashi, N. Watanabe, Y. Khajuria, Y. Udagawa, and J. H. D. Eland, *Phys. Rev. Lett.* **94**, 213202 (2005).
- [61] J. Ullrich and V. Shevelko (Springer, 2003).
- [62] B. J. Whitaker, *Imaging in molecular dynamics: technology and applications* (Cambridge University Press, 2003) p. §2.4.1.
- [63] M. Uiberacker, T. Uphues, M. Schultze, A. J. Verhoef, V. Yakovlev, M. F. Kling, J. Rauschenberger, N. M. Kabachnik, H. Schröder, M. Lezius, *et al.*, *Nature* **446**, 627 (2007).
- [64] P. Corkum and F. Krausz, *Nature Physics* **3**, 381 (2007).

- [65] S. Haessler, J. Caillat, W. Boutu, C. Giovanetti-Teixeira, T. Ruchon, T. Auguste, Z. Diveki, P. Breger, A. Maquet, B. Carré, *et al.*, *Nature Physics* **6**, 200 (2010).
- [66] C. T. Whelan, *Fragmentation Processes: Topics in Atomic and Molecular Physics* (Cambridge University Press, 2012).
- [67] M. Guilhaus, *Journal of Mass Spectrometry* **30**, 1519 (1995).
- [68] E. W. Schlag, *Time-of-flight mass spectrometry and its applications* (Newnes, 2012).
- [69] J. Ullrich, R. Moshhammer, A. Dorn, R. Dörner, L. P. H. Schmidt, and H. Schmidt-Böcking, *Reports on Progress in Physics* **66**, 1463 (2003).
- [70] H. Schmidt-Böcking, R. Dörner, O. Jagutzki, T. Jahnke, V. Mergel, L. P. H. Schmidt, T. Weber, A. Czasch, C. Wimmer, M. Hattass, *et al.*, *Nuclear Physics A* **737**, 306 (2004).
- [71] R. Dörner, V. Mergel, O. Jagutzki, L. Spielberger, J. Ullrich, R. Moshhammer, and H. Schmidt-Böcking, *Physics Reports* **330**, 95 (2000).
- [72] V. Sharma and B. Bapat, *The European Physical Journal D-Atomic, Molecular, Optical and Plasma Physics* **37**, 223 (2006).
- [73] G. A. Bird, *Molecular gas dynamics and the direct simulation of gas flows* (Clarendon, 1994).
- [74] W. Wiley and I. McLaren, *Review of Scientific Instruments* **26**, 1150 (1955).
- [75] J. Ladislav Wiza, *Nuclear Instruments and Methods* **162**, 587 (1979).
- [76] O. Jagutzki, V. Mergel, K. Ullmann-Pfleger, L. Spielberger, U. Spillmann, R. Dörner, and H. Schmidt-Böcking, *Nuclear Instruments and Methods in Physics Research Section A: Accelerators, Spectrometers, Detectors and Associated Equipment* **477**, 244 (2002).
- [77] V. Sharma, *Momentum Spectroscopic Studies of Atomic and Molecular Ionisation*, Ph.D. thesis, Mohanlal Sukhadia University, Udaipur (2007).

- [78] I. Ben-Itzhak, S. Ginther, and K. Carnes, *Nuclear Instruments and Methods in Physics Research Section B: Beam Interactions with Materials and Atoms* **66**, 401 (1992).
- [79] I. Ali, R. Dörner, O. Jagutzki, S. Nüttgens, V. Mergel, L. Spielberger, K. Khayyat, T. Vogt, H. Bräuning, K. Ullmann, *et al.*, *Nuclear Instruments and Methods in Physics Research Section B: Beam Interactions with Materials and Atoms* **149**, 490 (1999).
- [80] <http://www.roentdek.com>.
- [81] D. Seccombe and T. Reddish, *Review of Scientific Instruments* **72**, 1330 (2001).
- [82] M. Vestal, P. Juhasz, and S. Martin, *Rapid Communications in Mass Spectrometry* **9**, 1044 (1995).
- [83] J. Eland, *Laser. Chem* **11**, 259 (1991).
- [84] C. Maul and K.-H. Gericke, *International Reviews in Physical Chemistry* **16**, 1 (1997).
- [85] S. Hsieh and J. H. Eland, *Journal of Physics B: Atomic, Molecular and Optical Physics* **30**, 4515 (1997).
- [86] F. Légaré, K. F. Lee, I. V. Litvinyuk, P. W. Dooley, A. D. Bandrauk, D. M. Villeneuve, and P. B. Corkum, *Phys. Rev. A* **72**, 052717 (2005).
- [87] D. Mathur, L. Andersen, P. Hvelplund, D. Kella, and C. Safvan, *Journal of Physics B: Atomic, Molecular and Optical Physics* **28**, 3415 (1995).
- [88] L. Andersen, J. Posthumus, O. Vahtras, H. Ågren, N. Elander, A. Nunez, A. Scrinzi, M. Natiello, and M. Larsson, *Physical review letters* **71**, 1812 (1993).
- [89] T. A. Field and J. H. Eland, *Chemical physics letters* **211**, 436 (1993).

- [90] V. Sharma, B. Bapat, J. Mondal, M. Hochlaf, K. Giri, and N. Sathyamurthy, *The Journal of Physical Chemistry A* **111**, 10205 (2007).
- [91] I. Ben-Itzhak, S. G. Ginther, V. Krishnamurthi, and K. D. Carnes, *Phys. Rev. A* **51**, 391 (1995).
- [92] B. Siegmann, U. Werner, R. Mann, N. M. Kabachnik, and H. O. Lutz, *Phys. Rev. A* **62**, 022718 (2000).
- [93] U. Werner, K. Beckord, J. Becker, and H. O. Lutz, *Phys. Rev. Lett.* **74**, 1962 (1995).
- [94] J. Laskin and C. Lifshitz, *Journal of mass spectrometry* **36**, 459 (2001).
- [95] D. Mathur, *Physics reports* **391**, 1 (2004).
- [96] P. Lablanquie, J. Delwiche, M.-J. Hubin-Franskin, I. Nenner, P. Morin, K. Ito, J. H. D. Eland, J.-M. Robbe, G. Gandara, J. Fournier, and P. G. Fournier, *Phys. Rev. A* **40**, 5673 (1989).
- [97] M. Tarisien, L. Adoui, F. Frémont, D. Lelièvre, L. Guillaume, J.-Y. Chesnel, H. Zhang, A. Dubois, D. Mathur, S. Kumar, M. Krishnamurthy, and A. Cas-simi, *Journal of Physics B: Atomic, Molecular and Optical Physics* **33**, L11 (2000).
- [98] N. Neumann, D. Hant, L. P. H. Schmidt, J. Titze, T. Jahnke, A. Czasch, M. S. Schöffler, K. Kreidi, O. Jagutzki, H. Schmidt-Böcking, and R. Dörner, *Phys. Rev. Lett.* **104**, 103201 (2010).
- [99] T. Osipov, C. Cocke, M. Prior, A. Landers, T. Weber, O. Jagutzki, L. Schmidt, H. Schmidt-Böcking, and R. Dörner, *Physical review letters* **90**, 233002 (2003).
- [100] B. Bapat and V. Sharma, *Journal of Physics B: Atomic, Molecular and Optical Physics* **40**, 13 (2007).
- [101] V. Sharma and B. Bapat, *Phys. Rev. A* **75**, 040503 (2007).

- [102] U. Werner, N. Kabachnik, V. Kondratyev, and H. O. Lutz, *Physical review letters* **79**, 1662 (1997).
- [103] C. Caraby, A. Cassimi, L. Adoui, and J. Grandin, *Physical Review A* **55**, 2450 (1997).
- [104] J. D. Bozek, N. Saito, and I. H. Suzuki, *The Journal of chemical physics* **100**, 393 (1994).
- [105] N. Saito and I. H. Suzuki, *Phys. Rev. Lett.* **61**, 2740 (1988).
- [106] J. D. Bozek, N. Saito, and I. H. Suzuki, *Physical Review A* **51**, 4563 (1995).
- [107] T. P. Rakitzis, A. J. van den Brom, and M. H. Janssen, *Science* **303**, 1852 (2004).
- [108] Y.-K. Kim, K. K. Irikura, and M. Ali, National Institute of Standards and Technology, *Journal of Research* **105**, 285 (2000).
- [109] A. Pandey and B. Bapat, *International Journal of Mass Spectrometry* **361**, 23 (2014).
- [110] G. Fraser, *International Journal of Mass Spectrometry* **215**, 13 (2002).
- [111] E. Liénard, M. Herbane, G. Ban, G. Darius, P. Delahaye, D. Durand, X. Flechard, M. Labalme, F. Mauger, A. Mery, *et al.*, *Nuclear Instruments and Methods in Physics Research Section A: Accelerators, Spectrometers, Detectors and Associated Equipment* **551**, 375 (2005).
- [112] B. Gaire, A. Sayler, P. Wang, N. G. Johnson, M. Leonard, E. Parke, K. Carnes, and I. Ben-Itzhak, *Review of scientific instruments* **78**, 024503 (2007).
- [113] C. Ma, M. R. Bruce, and R. A. Bonham, *Phys. Rev. A* **44**, 2921 (1991).
- [114] L. J. Butler, *Annual review of physical chemistry* **49**, 125 (1998).
- [115] C. Eckart, *Phys. Rev.* **47**, 552 (1935).

- [116] E. F. Valeev and C. D. Sherrill, *The Journal of Chemical Physics* **118**, 3921 (2003).
- [117] Y. Öhrn, *Elements of molecular symmetry* (Wiley-Interscience New York:, 2000).
- [118] R. Carter, *Molecular Symmetry and Group Theory* (Wiley, 1998).
- [119] J. von Neumann and E. Wigner, *Phys. Z* **30**, 467 (1929).
- [120] K. R. Naqvi and W. B. Brown, *International Journal of Quantum Chemistry* **6**, 271 (1972).
- [121] E. U. Condon, *Physical Review* **32**, 858 (1928).
- [122] R. S. Berry and S. E. Nielsen, *Physical Review A* **1**, 395 (1970).
- [123] J. Bardsley, *Chemical Physics Letters* **1**, 229 (1967).
- [124] A. Russek, M. Patterson, and R. Becker, *Physical Review* **167**, 17 (1968).
- [125] R. S. Berry, *The Journal of Chemical Physics* **45**, 1228 (1966).
- [126] P. Knowles, M. Schütz, and H.-J. Werner, *Modern methods and algorithms of quantum chemistry* **3**, 97 (2000).
- [127] K. Raghavachari and J. B. Anderson, *The Journal of Physical Chemistry* **100**, 12960 (1996).
- [128] T. H. Dunning Jr, *The Journal of Chemical Physics* **90**, 1007 (1989).
- [129] A. Wahl, G. Das, and H. Schaefer III, *Methods of Electronic Structure Theory* **3**, 51 (1977).
- [130] H. Werner and W. Meyer, *The Journal of Chemical Physics* **73**, 2342 (1980).
- [131] B. Roos, G. Dierksen, and S. Wilson, *Reidel, Dordrecht* , 161 (1983).
- [132] B. O. Roos, P. R. Taylor, *et al.*, *Chemical Physics* **48**, 157 (1980).

- [133] B. O. Roos, *Advances in Chemical Physics: Ab Initio Methods in Quantum Chemistry Part 2, Volume 69*, 399 (1987).
- [134] H. Werner and E. Reinsch, *The Journal of Chemical Physics* **76**, 3144 (1982).
- [135] R. Harrison and N. Handy, *Chemical Physics Letters* **95**, 386 (1983).
- [136] H.-J. Werner, P. J. Knowles, G. Knizia, F. R. Manby, and M. Schütz, *WIREs Comput Mol Sci* **2**, 242 (2012).
- [137] <https://bse.pnl.gov/bse/portal> .
- [138] H. Werner and W. Meyer, *The Journal of Chemical Physics* **74**, 5794 (1981).
- [139] H. Werner and P. J. Knowles, *The Journal of Chemical Physics* **82**, 5053 (1985).
- [140] P. J. Knowles and H.-J. Werner, *Chemical physics letters* **115**, 259 (1985).
- [141] H.-J. Werner and P. J. Knowles, *The Journal of chemical physics* **89**, 5803 (1988).
- [142] <http://cccbdb.nist.gov> (Release 16a, August 2013).
- [143] R. J. Le Roy, <http://leroy.uwaterloo.ca/programs/>, 2007. .
- [144] Z. Wu, C. Wu, X. Liu, Y. Deng, Q. Gong, D. Song, and H. Su, *The Journal of Physical Chemistry A* **114**, 6751 (2010).
- [145] M. Lundqvist, P. Baltzer, D. Edvardsson, L. Karlsson, and B. Wannberg, *Phys. Rev. Lett.* **75**, 1058 (1995).
- [146] J. H. D. Eland, M. Hochlaf, G. C. King, P. S. Kreyenin, R. J. LeRoy, I. R. McNab, and J.-M. Robbe, *Journal of Physics B: Atomic, Molecular and Optical Physics* **37**, 3197 (2004).
- [147] F. Penent, R. Hall, R. Panajotović, J. Eland, G. Chaplier, and P. Lablanquie, *Physical review letters* **81**, 3619 (1998).

- [148] J. Rajput, S. De, A. Roy, and C. P. Safvan, *Phys. Rev. A* **74**, 032701 (2006).
- [149] T. Mizuno, T. Yamada, H. Tsuchida, Y. Nakai, and A. Itoh, *Phys. Rev. A* **81**, 012704 (2010).
- [150] J. H. Eland, *Chemical Physics* **294**, 171 (2003).
- [151] O. Furuhashi, T. Kinugawa, S. Masuda, C. Yamada, and S. Ohtani, *Chemical Physics Letters* **337**, 97 (2001).
- [152] M. Ahmad, P. Lablanquie, F. Penent, J. G. Lambourne, R. I. Hall, and J. H. D. Eland, *Journal of Physics B: Atomic, Molecular and Optical Physics* **39**, 3599 (2006).
- [153] M. Hochlaf, R. Hall, F. Penent, H. Kjeldsen, P. Lablanquie, M. Lavollée, and J. Eland, *Chemical Physics* **207**, 159 (1996).
- [154] J. Bouhnik, I. Gertner, B. Rosner, Z. Amitay, O. Heber, D. Zajfman, E. Sidky, and I. Ben-Itzhak, *Physical Review A* **63**, 032509 (2001).
- [155] T. Masuoka, *The Journal of Chemical Physics* **101**, 322 (1994).
- [156] S. Hsieh and J. H. D. Eland, *Journal of Physics B: Atomic, Molecular and Optical Physics* **29**, 5795 (1996).
- [157] M. Lucchini, K. Kim, F. Calegari, F. Kelkensberg, W. Siu, G. Sansone, M. J. J. Vrakking, M. Hochlaf, and M. Nisoli, *Phys. Rev. A* **86**, 043404 (2012).
- [158] T. Osipov, T. Weber, T. N. Rescigno, S. Y. Lee, A. E. Orel, M. Schöffler, F. P. Sturm, S. Schössler, U. Lenz, T. Havermeier, M. Kühnel, T. Jahnke, J. B. Williams, D. Ray, A. Landers, R. Dörner, and A. Belkacem, *Phys. Rev. A* **81**, 011402 (2010).
- [159] B. Olsson, G. Kindvall, and M. Larsson, *The Journal of Chemical Physics* **88**, 7501 (1988).
- [160] J. Senekowitsch, S. O'Neil, P. Knowles, and H. J. Werner, *The Journal of Physical Chemistry* **95**, 2125 (1991).

- [161] F. R. Bennett, *The Journal of Chemical Physics* **103**, 3613 (1995).
- [162] V. Krishnamurthi, K. Nagesha, V. R. Marathe, and D. Mathur, *Phys. Rev. A* **44**, 5460 (1991).
- [163] T. Sedivcova, P. R. Zdanska, V. Spirko, and J. Fiser, *The Journal of Chemical Physics* **124**, 214303 (2006).
- [164] Y.-K. Kim and J.-P. Desclaux, *Physical Review A* **66**, 012708 (2002).
- [165] L. D. Landau and E. M. Lifshitz, *Quantum mechanics non-relativistic theory*, Vol. 3 (Pergamon Press, 1991) p. §148.
- [166] Z. Amitay, D. Zajfman, P. Forck, U. Hechtfisher, B. Seidel, M. Grieser, D. Habs, R. Repnow, D. Schwalm, and A. Wolf, *Physical Review A* **54**, 4032 (1996).



## **Publications attached with the thesis**

- 1. Charge symmetric dissociation of doubly ionized N<sub>2</sub> and CO molecules**  
A. Pandey, B. Bapat, K.R. Shamasundar, The Journal of Chemical Physics, **140, 3** (2014)
- 2. Effect of transmission losses on measured parameters in multi-ion coincidence momentum spectrometers**  
A. Pandey, and B. Bapat, International Journal of Mass Spectrometry, **361, 0** (2014)



## Charge symmetric dissociation of doubly ionized N<sub>2</sub> and CO molecules

A. Pandey,<sup>1,a)</sup> B. Bapat,<sup>1</sup> and K. R. Shamasundar<sup>2</sup>

<sup>1</sup>Physical Research Laboratory, Ahmedabad 380009, India

<sup>2</sup>Indian Institute of Science Education and Research, Mohali, Sector 81, SAS Nagar 140306, India

(Received 1 September 2013; accepted 23 December 2013; published online 21 January 2014)

We report a comparative study of the features in dissociative double ionization by high energy electron impact of N<sub>2</sub> and CO molecules. The ratio of cross-section of charge symmetric dissociative ionization to non-dissociative ionization (CSD-to-ND ratio) and the kinetic energy release (KER) spectra of dissociation are experimentally measured and carefully corrected for various ion transmission losses and detector inefficiencies. Given that the double ionization cross sections of these iso-electronic diatomics are very similar, the large difference in the CSD-to-ND ratios must be attributable to the differences in the evolution dynamics of the dications. To understand these differences, potential energy curves (PECs) of dications have been computed using multi-reference configuration interaction method. The Franck-Condon factors and tunneling life times of vibrational levels of dications have also been computed. While the KER spectrum of N<sub>2</sub><sup>2+</sup> can be readily explained by considering dissociation via repulsive states and tunneling of meta-stable states, indirect dissociation processes such as predissociation and autoionization have to be taken into account to understand the major features of the KER spectrum of CO<sup>2+</sup>. Direct and indirect processes identified on the basis of the PECs and experimental KER spectra also provide insights into the differences in the CSD-to-ND ratios. © 2014 AIP Publishing LLC. [<http://dx.doi.org/10.1063/1.4861665>]

### I. INTRODUCTION

In an ionizing collision between a fast charged particle and a molecule, the process of electron removal is in general very rapid compared to the nuclear motion within the target molecule. Further evolution of the molecular ion formed in the collision is entirely determined by the dynamics of the nuclei and remaining electrons in the system. Depending on the nature of electronic state in which it is created, the molecular ion may dissociate or stay as a stable system after ionization. Most molecular ions with charge higher than two, due to strong Coulomb repulsion between the nuclei, possess purely repulsive potential energy surfaces (PES) with little structure. As a result, such ions are generally unstable and dissociate quickly into two or more fragment ions.<sup>1</sup>

The PES of singly and doubly ionized molecules, however, exhibit interesting features arising due to competition between bonding and repulsive forces. In addition to purely repulsive states, there are several states having a minimum followed by a potential barrier connected to a dissociation asymptote which generally lies below the minimum. This leads to meta-stable vibrational states whose life-time is governed by tunneling through the potential barrier. Dications are of special interest as they contain relatively smaller number of electronic states which support vibrational structure and hence are better candidate for probing various dissociation processes.

There are two types of dissociation processes, direct and indirect. A direct dissociation process is one in which the molecular ion follows the same potential energy curve on

which it is created in during the entire dissociation. If only direct processes are significant in a dissociation, the observed properties of dissociation are relatively simple to calculate. All features in kinetic energy release (KER) spectra can then be identified as a result from the properties of individual electronic states. The tunneling life times of these vibrational states govern the features appearing in the KER spectrum. Indirect processes such as autoionization and predissociation arise due to coupling between states. Depending on the strength of the coupling, new dissociation pathways open up. Then, the tunneling life-time of a given state can provide only an upper bound for the true life-time. This may result in features in the KER spectrum that would otherwise not appear. Several investigations have shown the significance of indirect processes in dissociation of dications.<sup>2-5</sup>

The dications of N<sub>2</sub> and CO formed by charged particle collision or photoabsorption have been studied extensively with a view to understand the dynamics and evolution of multiply charged molecular ions employing a variety of experimental methods.<sup>1,6-15</sup> Their electron-spectra have also been analyzed extensively to probe the properties of vibrational states.<sup>16-19</sup> The life time of the dications has also been studied in great detail and it is known that these dications have states with life times ranging from a few nano-seconds up to several seconds.<sup>20-22</sup> In general, a dication may undergo either charge symmetric dissociation (CSD) in which the net positive charge on the molecular ion is equally shared by fragments, or charge asymmetric dissociation (CAD) in which charge sharing is unequal. The CSD and CAD of N<sub>2</sub><sup>2+</sup> and CO<sup>2+</sup> have been analyzed in many experiments. CSD is the energetically favored channel for these dications. This can be attributed to the second ionization potential which is

<sup>a)</sup>Electronic mail: amrendra@prl.res.in

much larger than the first one for all the dissociation fragment atoms. As a result, CSD is easily accessed in experiments and has been extensively discussed.

In the past, KER spectra of CSD of  $N_2^{++}$  and  $CO^{++}$  have been recorded experimentally with sufficient accuracy, resolving the contribution from many vibrational levels of low-lying states.<sup>6,8</sup> There are many theoretical works involving computation of potential energy curves (PECs) of these dications<sup>7,9,11,23–27</sup> to explain the experimental observations of different types of experiments, and some of the features in KER spectrum have been discussed in these studies.<sup>6,9,10</sup> The magnitude and the overall shape of the double ionization cross sections of these iso-electronic diatomics are very similar,<sup>28</sup> so a comparison of the detailed features of the dissociation of the dications is of interest. While KER spectrum depends purely on dissociative processes, the CSD-to-ND ratio is a measure of relative importance of dissociative and non-dissociative processes. In this work, we estimate carefully corrected CSD-to-ND ratios for these molecules which are not available in literature. Since these ratios are sensitive to dissociation processes and life-time of states, we attempt to understand why these ratios are widely different (factor of 8) for these molecules. This requires identification of pathways for dissociation of the dications in both charged species. For this purpose, accurate *ab initio* calculations of the PECs of dications covering a range of 20 eV above the double ionization threshold have been performed. These are used to calculate the Franck–Condon (FC) factors and the tunneling life times of vibrational levels of all electronic states exhibiting a local minimum. Identified contributions of direct and indirect processes are used to understand the differences in the KER spectra and CSD-to-ND ratios of the dications.

## II. EXPERIMENT

### A. Apparatus

Molecular ions are created by the impact of high energy (1.3 keV) electrons on molecules under single collision condition. The electron beam and the effusive molecular beam overlap in an interaction volume of about 2 mm<sup>3</sup> in a crossed-beams geometry. A recoil ion momentum spectrometer (RIMS) is employed<sup>29</sup> to analyze the collision products. In brief, the RIMS consists a single-field time-of-flight (ToF) mass spectrometer combined with a multi-hit capable, large area, position-sensitive detector based on a microchannel plate (MCP) and a delay-line anode. The details of the set-up can be found in Sharma and Bapat.<sup>30</sup> A uniform electric field of 60 V cm<sup>-1</sup> is applied to extract the ions. The length of the accelerating region is 11 cm, followed by a field-free drift region of 22 cm. Ion ToF is measured by electron–ion coincidence. Measuring the ToF is a means to separate the ions based on their mass/charge ratio and to obtain the component of initial momentum parallel to the spectrometer axis. The two transverse components are obtained by measuring, in addition, the position of hit ( $x$ ,  $y$ ) of the ion on the detector plane after flying through extraction and drift region. The spectrometer is capable of detecting multiple ionic fragments in a time-ordered manner, arriving within a time-window

of 32  $\mu$ s after being triggered by the ejected electron from the ionization zone. Collision rates are kept sufficiently low to avoid false coincidences (ionization rate  $<100$  s<sup>-1</sup>), enabling the determination of correlated kinematics between ionic fragments. The ToF and position data can be converted event-by-event into a momentum map of the fragments and used for further analysis.

The momentum resolution for the three components are calculated by taking the full-width at half-maximum (FWHM) of the ToF and position distributions of ions from a monoatomic gas. For this purpose, a control experiment was performed using Ar as the target, under otherwise identical conditions. The spread in the momenta for the Ar<sup>+</sup> account for the thermal width of gas beam, finite size of ionization source and all other errors collectively. Momentum resolutions, in atomic units, are  $\sigma_{p_z} = 10$  a.u.,  $\sigma_{p_x} = 23$  a.u.,  $\sigma_{p_y} = 24$  a.u., which translates to a kinetic energy resolution of 225 meV in the worst case.

### B. Analysis of experimental data

First hit ToF spectrum of  $N_2$  and  $CO$  molecules are shown in Figure 1; only the region that covers the fragmentation of doubly ionized molecular ions are shown (In both cases, due to almost same mass, the singly ionized parent ions appear at 6.574  $\mu$ s mean ToF.). The first hit ToF spectrum shows the ions that reach the detector first after fragmentation. All dications which have not dissociated within the flight time will contribute to the first hit ToF spectrum along with the lightest of the fragment ions formed by dissociation. Since  $N_2^{++}$  and  $CO^{++}$  have same ToF, it is essential to ensure that there is no cross-contamination across the two experimental runs. By allowing a few days of pumping out time between runs, cross-contamination was nearly eliminated. This is confirmed by the fact that the  $CO^{++}$  peak is very sharp, whereas  $N_2$  contamination would have broadened the peak to the shape shown in Figure 1. Further, there is no peak in the  $N_2$  spectrum around the positions where  $C^+$  and  $O^+$  would appear. The estimated contamination error is less than 1%.

To measure the CSD-to-ND ratio, it is necessary to make an accurate estimate of the counts of doubly ionized molecular ions of  $N_2^{++}$  and  $CO^{++}$  and of dications that dissociate via the CSD channel. The estimate of the counts of doubly ionized molecular ions is obtained from the first hit ToF spectrum shown in Figure 1. Because the peaks for both dications in ToF spectrum are mixed with broader peaks from fragment ions, accurate estimates are not easy. The  $CO^{++}$  peak lies on the overlapping tails of the  $C^+$  and  $O^+$  peaks, while the  $N_2^{++}$  peak lies over the broad  $N^+$  peak. To separate the contribution of the undissociated dication from the peak, we note that the fragment ion peak results from a mixture of ions arising from a multitude of several precursor states, the width of the peak reflecting the kinetic energy distribution of the ions. The contribution from each state is approximated by a Gaussian function centered at the mean ToF, determined from the experiment. We carry out unconstrained fitting of each ToF spectrum in the region 3.0–6.0  $\mu$ s with Gaussian functions. Twelve Gaussian functions are used for the  $N_2$  spectrum and 18 for the  $CO$  spectrum. The residual

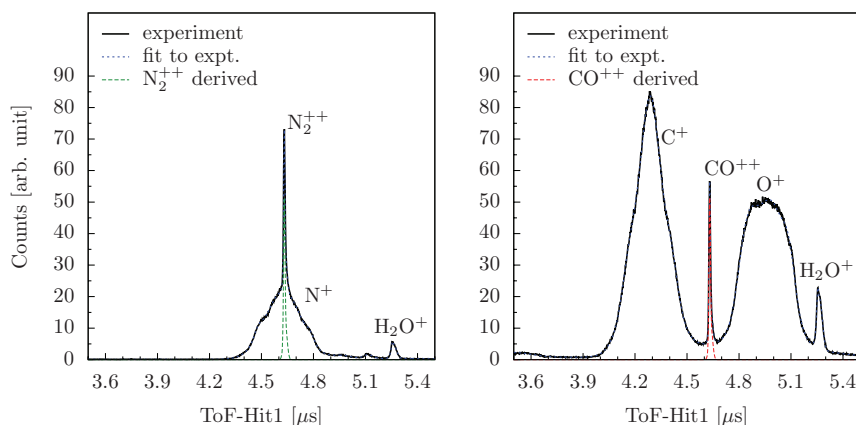


FIG. 1. Partial first hit ToF spectra of  $N_2$  and  $CO$ , covering the range of doubly ionized molecular ions and the ions arising from their dissociation. Spectra are normalized to make the non-dissociated doubly ionized molecular ion counts (of  $N_2^{++}$  and  $CO^{++}$ ) equal. The broken line (dots) is the cumulative fit using multiple Gaussian functions, as described in the text. It overlaps almost entirely with the raw data. The long dashed line shows peak of the undissociated dication derived from the fit.

error between fitted and experimental spectra is less than 4% at any point in the entire range considered. The fitted curves are shown by dotted lines in Figure 1. Amongst all Gaussian functions needed to fit the entire range of ToF under consideration, two very narrow Gaussians centered around the peak of the dications ( $\mu = 4.631 \mu\text{s}$ ,  $\sigma = 0.0047 \mu\text{s}$ ) and ( $\mu = 4.637 \mu\text{s}$ ,  $\sigma = 0.0122 \mu\text{s}$ ) with relative amplitudes 1:0.2 are common to both cases and their sum accounts for the undissociated molecular dications. (The ToF distributions of undissociated species would be very narrow, as the only kinetic energy they have is thermal.) The rest of the Gaussian functions correspond to the broader features due to dissociation. The sum of the two narrow Gaussians is taken to be the intensity of the undissociated dications. The robustness of the fit is established by the fact that the ToF distributions of the monocations  $N_2^+$  and  $CO^+$  are similarly well-fitted by a pair of narrow Gaussian functions, ( $\mu = 6.556 \mu\text{s}$ ,  $\sigma = 0.0072 \mu\text{s}$ ) and ( $\mu = 6.569 \mu\text{s}$ ,  $\sigma = 0.0243 \mu\text{s}$ ) also in the proportion 1:0.2, and this is common to the two species. Furthermore, the standard deviation of the fit for the monocations (comprising the sum of the two narrow Gaussians) is  $\sqrt{2}$  times the standard deviation of the fit for the dications (also comprising the sum of two narrow Gaussians). This is consistent with the fact that

the ToF of singly charged ions would be  $\sqrt{2}$  times the ToF of doubly charged ions. In Figure 1, the ToF spectra are normalized in such a manner that the counts under the fitted  $N_2^{++}$  and  $CO^{++}$  peaks, representing ND counts, are equal. In unnormalized spectra, the common peak for  $H_2O^+$  would appear identical. The time correlation maps of CSD of  $N_2^{++}$  and  $CO^{++}$  shown in Figure 2 are normalized by their corresponding ND counts.

To obtain the correct CSD-to-ND ratio, we need to correct the recorded experimental cross sections for the intrinsic detection efficiency of the detector. The detection efficiency of the MCP depends upon the charge state and mass of the detected ions.<sup>31</sup> The upper bound of detection efficiency is defined by open area ratio which in our case is 0.6. At the applied front plate bias of  $-2800 \text{ V}$ , the detection efficiency for  $N_2^{++}$  and  $CO^{++}$  is 0.52, while for the singly charged ions  $C^+$ ,  $N^+$ , and  $O^+$ , it is 0.50. These values have been taken from the report by Liénard *et al.*<sup>32</sup> The corrected counts of  $N_2^{++}$  and  $CO^{++}$  are thus obtained by dividing the observed counts by the corresponding efficiency. The observed counts from CSD need a correction for the detection efficiency for pair coincidence measurement. We take this factor to be the square of the singles counting efficiency, i.e., 0.25.

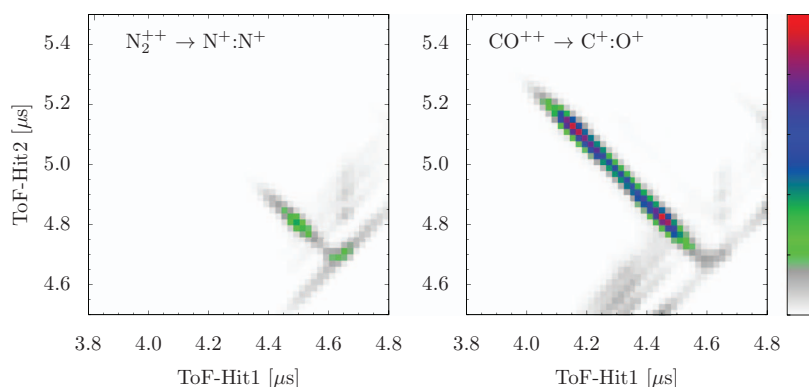


FIG. 2. ToF Hit1-Hit2 correlation maps of the CSD channels  $N_2^{++} \rightarrow N^+:N^+$  and  $CO^{++} \rightarrow C^+:O^+$ . The intensity in the correlation maps is normalized to the respective counts of undissociated doubly ionized molecular ions. The colour (intensity) scale is common to the two maps.

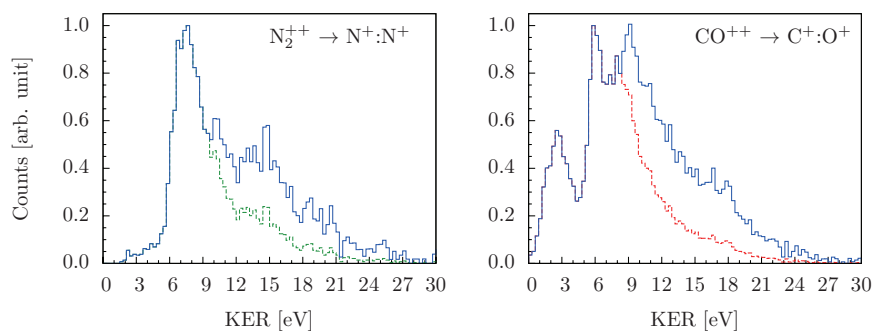


FIG. 3. KER spectra of the CSD channel of  $N_2^{++}$  and  $CO^{++}$ . In both plots, the histogram shown with a broken line is the observed spectrum, whereas the KER spectrum after correction for losses is shown by the continuous line. Correction is applicable to the  $N_2^{++}$  spectrum from 9.70 eV onwards, and to the  $CO^{++}$  spectrum from 8.50 eV onwards.

The observed number of ion pair counts requires further correction due to loss in transmitting the ions. Transmission loss arises due to two factors—finite size of the detector and finite strength of the extraction field. The loss is a function of the initial kinetic energy of the particles. In particular, there is an upper limit of the kinetic energy,  $KE_{limit}$  (4.85 eV in our case), of an ion, which even when emitted perpendicular to the extraction field, will be transmitted to the detector. Beyond this energy, the transmission will depend on the angle of ejection of the ion. The loss factor is derived for a break-up into two fragments having masses  $m_1$ ,  $m_2$  ( $m_1 < m_2$ ), assuming isotropic emission of ions. The limiting value of the kinetic energy release,  $KER_{limit}$ , taking into account momentum conservation rules for two-body break-up, up to which there is full transmission works out to be  $(1 + m_1/m_2) \times KE_{limit}$ . The fraction of events lost for  $KER > KER_{limit}$  is equal to  $(1 - KER_{limit}/KER)^{1/2}$ . The observed intensity in the KER spectrum is corrected to the true intensity using the calculated loss factor. In case of CSD of  $N_2^{++}$ , loss starts from 9.70 eV KER and from 8.50 eV for  $CO^{++}$ . For CSD of  $CO^{++}$ , loss starts from relatively less KER value because although the momentum is shared equally in a two-body break-up process, the kinetic energy of  $C^+$  is higher than that of  $O^+$ , for a given KER. At 8.50 eV KER for dissociation of  $CO^{++}$ ,  $C^+$  ions attain 4.85 eV energy and thus loss starts. The corrected KER spectrum of CSD of  $N_2^{++}$  and  $CO^{++}$  are shown in Figure 3 with continuous lines. The counts of the CSD are taken from the corrected KER spectrum. We have also considered the loss because of the dead time (20 ns) of the multi-hit detection. However, this loss turns out to be very small. The loss is 0.5% at 1 eV KER for CSD of  $N_2^{++}$ , and it decreases as square root of the energy.

The CSD channel appears as an island in the ToF Hit1–Hit2 correlation maps in Figure 2. The intensity of the island relates to the propensity of dissociation, while the extent of the island reflects the distribution of the component of momentum of the ions along the spectrometer axis. (The other components of momentum would be similarly distributed in the case of isotropic emission, and would show up in the  $x$ ,  $y$  image on the detector.) In Figure 2, the correlation maps are normalized to the counts under the peaks of the non-dissociated dications, obtained from the fits in the ToF-Hit1 spectrum. The normalization is carried out after

applying all corrections. The relative intensities in the correlation maps show that  $N_2^{++}$  is less likely to dissociate than  $CO^{++}$ .

After including all the corrections discussed above, the CSD-to-ND ratio for  $N_2^{++}$  is 0.07 and for  $CO^{++}$  it is 0.56. If the loss in transmission is not accounted for, the CSD-to-ND ratios would be 0.04 and 0.38, respectively.

The correction for the loss in transmission of ions not only changes the CSD-to-ND ratios significantly but also modifies the KER distribution itself, particularly at larger KER values. It is important to note that the maximum KER observed in the raw spectrum (about 30 eV in both cases) is the correct limit of the largest KER of dissociation. That is because ions ejected along the spectrometer axis will always be transmitted to the detector irrespective of their kinetic energy up to an upper limit of  $qV$ , where  $q$  is the ion charge and  $V$  is the maximum retarding potential in the spectrometer, which is +180 V in this experiment. It is clear that the raw KER data can be quite misleading because of various inefficiencies and losses in the spectrometer. This point is often ignored in a large number of reports. A systematic analysis of the losses is not available in literature to the best of our knowledge. Based on the estimates of the momentum resolution, the resolution in KER spectrum for two body break up channels for equal energy sharing is 300 meV, by error propagation of two independent variables. At this resolution we cannot determine the KER contributions coming from each vibrational level as has been achieved in other experiments.<sup>6</sup> However, the contributions coming from various electronic states can be clearly identified.

### III. THEORY

We have performed *ab initio* calculations of the ground electronic state of neutral molecules and the PECs of the dications to enable computation of various vibrational levels, their tunneling life-times, their FC factors with respect to  $v = 0$  level of ground electronic state, and the resulting KER values. For repulsive states leading to dissociation, the distribution of KER values are also computed.

### A. Calculation of potential energy curves

Electronic states of  $N_2$  and CO and their singly- and doubly charged molecular ions have been calculated under the BO approximation. All states are calculated using MOLPRO program package.<sup>33</sup> The complete active space self-consistent field (CASSCF) method and the multi-reference configuration interaction (MRCI) method have been used for the calculations using the standard correlation-consistent cc-pV5Z basis set. The CASSCF wave functions have been chosen to be of full-valence type, and have been used as the reference function in the subsequent MRCI calculation. The electronic states of  $N_2$  and its molecular ions are calculated in the finite point group  $D_{2h}$ , while for CO the  $C_{2v}$  group is used. State-averaging has been employed in CASSCF calculations in order to allow for a balanced description of several electronic states of dications. The symmetry of the computed electronic states has been reassigned to the corresponding symmetry of full symmetry group, i.e.,  $D_{\infty h}$  and  $C_{\infty v}$  for  $N_2$  and CO, respectively. The atomic states of N,  $N^+$ , C,  $C^+$ , and O,  $O^+$  have also been calculated using same method and their relative energy levels have been cross-checked values reported with NIST database<sup>34</sup> and other ionization data.<sup>35</sup>

Few PECs of doubly ionized molecular ions of  $N_2$  and CO are shown in Figure 4 and Figure 5, respectively. Computed data for all calculated states are given in the supplementary material (Tables A 1–A 8).<sup>36</sup> These PECs are plotted relative to the lowest ground state vibrational level of their neutral parents,  $N_2[{}^1\Sigma_g^+, v=0]$  and  $CO[{}^1\Sigma^+, v=0]$ . If vertical excitation is assumed, the excitation energy for the ground state  ${}^1\Sigma_g^+$  of  $N_2^{++}$  is 42.49 eV. For  $CO^{++}$  ground state  ${}^1\Sigma^+$  it is 40.97 eV. These results are in agreement with the results of other theoretical and experimental investigations.<sup>17,19</sup>

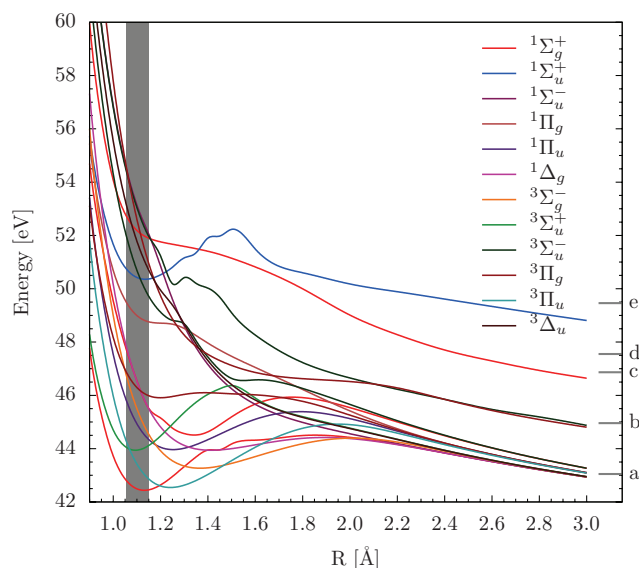


FIG. 4. A few low-lying PECs of  $N_2^{++}$ , plotted with respect to the ground state of  $N_2$ ;  ${}^1\Sigma_g^+$ ,  $v=0$ . FC region centered at 1.103 Å is shown by vertical line. The values of the potential energy in the separated ion limit at 3 Å for different CSD pathways of  $N_2^{++}$  are shown at the right edge: a( ${}^3P: {}^3P$ ) at 43.05 eV, b( ${}^3P: {}^1D$ ) at 44.96 eV, c( ${}^1D: {}^1D$ ) at 46.86 eV, d( ${}^3P: {}^1S$ ) at 47.55 eV, e( ${}^1D: {}^1S$ ) at 49.46 eV.

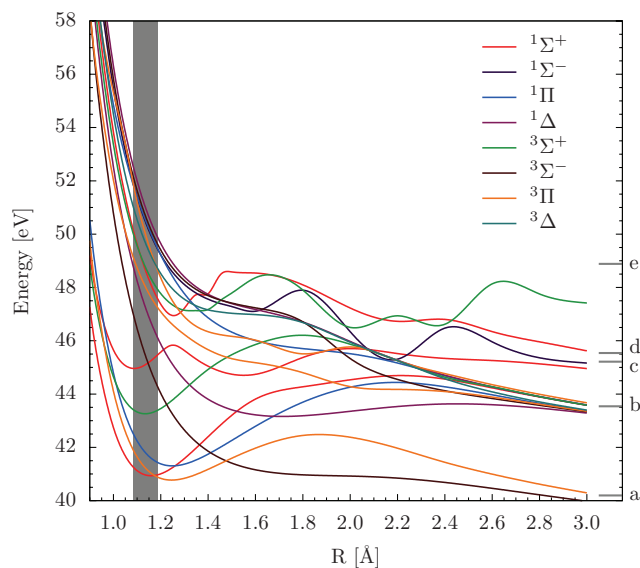


FIG. 5. A few low-lying PECs of  $CO^{++}$ , plotted with respect to the ground state of CO;  ${}^1\Sigma^+$ ,  $v=0$ . FC region centered at 1.135 Å is shown by vertical line. The values of the potential energy in the separated ion limit at 3 Å for different CSD pathways of  $CO^{++}$  are shown at the right edge: a( ${}^2P: {}^4S$ ) at 40.20 eV, b( ${}^2P: {}^2D$ ) at 43.54 eV, c( ${}^2P: {}^2P$ ) at 45.21 eV, d( ${}^4P: {}^4S$ ) at 45.54 eV, e( ${}^4P: {}^2D$ ) at 48.88 eV.

All PECs are calculated up to an internuclear separation  $R = 3 \text{ \AA}$ , since at this distance, the nature of PECs is almost entirely Coulombic and is appropriate for the identification of asymptotic limit. To identify the states of the separate atom (ion) limits of these dications, we match the potential energy given by the above curves to the value at the same  $R$  of a Coulombic energy function of two singly charged ions. The asymptotic function is taken to be  $E_a(i, j, R) = E_1^i + E_2^j + k/R$ , where  $E_1^i$  and  $E_2^j$  are the electronic energies of the separated fragments that are calculated separately. The value of the constant  $k$  is 14.40, when energies are in eV and  $R$  in Å.

Although reasonably accurate PECs of some of the low-lying states of these molecules are available in literature, our work requires that we calculate more number of states (at least two for each symmetry). The high accuracy calculations of  $N_2^{++}$  are by Bennett<sup>25</sup> and Wu *et al.*<sup>7</sup> Bennett<sup>25</sup> has used MRCI wavefunctions with cc-pV5Z basis sets, but report only five PECs that support vibrational states. Recently, Wu *et al.*<sup>7</sup> have calculated fifteen states (nine states supporting vibrational structure and six repulsive states) using MRCI calculations at the level of the cc-pV5Z basis set. However, since their calculation does not take into account the vibrational distribution, their reported KER values are not vibrationally resolved. Further, they have considered only one dissociation limit of  $N^+({}^3P) + N^+({}^3P)$ . The maximum KER in their calculation is from the repulsive  ${}^1\Sigma_u^-$  state at 14.41 eV, which is inadequate to explain the source of the broad peak observed at 15 eV. In this study, we have calculated a larger number of states (40) going up to 20 eV above the double ionization threshold, as reported in the supplementary material.<sup>36</sup>

For  $CO^{++}$ , most accurate calculations are by Sedivcova *et al.*<sup>27</sup> and Eland *et al.*<sup>11</sup> with similar accuracy. In order to

understand life-times of meta-stable states, Sedivcova *et al.*,<sup>27</sup> provide nine low lying PECs of CO<sup>++</sup>, seven of them supporting vibrational structure and two repulsive ones, calculated at MRCI level with cc-pVXZ [X = 5, 6] atomic basis sets. Eland *et al.*<sup>11</sup> have reported calculation of seven low-lying states supporting vibrational levels using MRCI wavefunction and cc-pV5Z basis set. Among other works,<sup>9,10,26</sup> Lablanquie *et al.* have reported all CO<sup>++</sup> states lying in the excitation range 35–60 eV. However, these calculations are only at CASSCF level with much smaller basis sets. Further, Lablanquie *et al.* report <sup>3</sup>Π state as ground state of CO<sup>++</sup> as well as the lowest state for vertical excitation, whereas accurate calculations show <sup>1</sup>Σ<sup>+</sup> to be the lowest state for vertical excitation. High accuracy calculations are necessary for obtaining accurate KER values, since PECs are very steep in the FC region. In this work, we have calculated about 30 states, which is a more comprehensive calculation on CO<sup>++</sup> compared to that available in the literature. The computed data are presented in the supplementary material.<sup>36</sup>

## B. Franck-Condon factors and kinetic energy release

The FC region for the ionizing transitions is shown by a shaded vertical region in Figures 4 and 5. The width of the region covers up to  $3\sigma$  of the probability density distribution of the  $v = 0$  ground state of the neutrals. To investigate the contribution to dissociation of the states having a local minimum, the vibrational levels supported in these minima and their tunneling life times have been computed. The states may be observed as stable, meta-stable or decaying in our experiment, depending on how their life times compare to the mean ToF of the stable dication. Molecular ions in vibrational levels that are stable against tunneling contribute to the non-dissociative cross-sections, while the ones that are unstable against tunneling or the ones that are excited to higher meta-stable and repulsive electronic states contribute to the dissociative cross sections. FC factors are calculated to determine the relative population in stable and meta-stable states, using LEVEL8.0 codes.<sup>37</sup> The PECs of N<sub>2</sub> and CO and their dications calculated from the MOLPRO codes are used in these calculations.

The KER values for PECs supporting at least one vibrational level are calculated as the difference between the energy of the vibrational level and the asymptotic limit energy of the electronic state. For repulsive electronic states, the KER is actually a distribution centered around the KER value resulting due to a state formed from a vertical transition from the equilibrium bond-length of the neutral, dissociating to its corresponding asymptote. The width of the distribution corresponding to a repulsive state is obtained by mapping the probability distribution of the ground vibrational states of neutrals across the given repulsive PEC.

While calculating the KER distribution it is necessary to take into account the probability of the states being accessed, which is specific to the perturbing agent. In the case of high energy electron impact, where there are no selection rules, the probability of excitation to a state at an energy  $\epsilon$  above the ground state is known to be<sup>38</sup> proportional to  $1/\epsilon^2$ . Hence, the amplitude of a particular transition contributing to the KER

distribution is corrected by a factor proportional to  $1/\epsilon^2$ , the proportionality factor being different for the two dications. We do not attempt to fit a combination of the excitation functions at different excitation energies to match the experimental KER distribution. Our focus is on explaining the features in the distribution.

The KER values derived from the computed PECs cover almost the entire range of KER observed in the experiment. The computed PECs cover up to 20 eV excitation above the double ionization threshold. We expect the contribution from even higher lying states to be less important based on two reasons. The first reason is that the excitation probability for the present collision system, as has been discussed above, decreases as an inverse square function of the excitation energy. So the higher lying states will be less populated in the collision with respect to lower lying states for a given charged species. The second reason is that higher lying states will be mostly of repulsive nature and thus they will always lead to larger KER values, and contribute mainly to the tail of the KER distribution. It should be noted that the major features in the N<sub>2</sub><sup>++</sup> as well as CO<sup>++</sup> KER spectrum are below 22 eV, which we have been able to explain with the states we have computed.

## IV. RESULTS

### A. KER distributions

Three categories of states need to be considered to explain the KER distributions. Only vertical transitions are considered. The first category is of states that support vibrational levels and are relatively stable against tunneling. States of this category will not contribute to dissociation if only tunneling is responsible. The second category is of states that support vibrational levels, but are unstable against tunneling for several vibrational levels. The third category is of states that are either purely repulsive or support a few vibrational levels with relatively small FC factors ( $<10^{-3}$ ) and decaying from the FC overlap region.

As described earlier, the KER distribution for CSD via repulsive states of doubly ionized molecular ions is obtained by reflecting the probability distribution of ground vibrational level of ground electronic state of neutral parent across the PEC in the FC region. The KER distribution corresponding to that PEC is then a Gaussian function whose area is proportional to the magnitude of the transition function which as described earlier varies as  $1/\epsilon^2$ . The experimental KER spectra and the computed contributions from different states for the two dications appear in Figures 6 and 7. The vibrational levels having FC factor greater than  $10^{-3}$  of N<sub>2</sub><sup>++</sup> and CO<sup>++</sup> are shown in Figure 8. The details of vibrational levels of N<sub>2</sub><sup>++</sup> and CO<sup>++</sup> are given in the supplementary material (Tables B 1–B 11).<sup>36</sup>

We first consider the case of N<sub>2</sub><sup>++</sup>, referring to Figures 4 and 8 and Table C1 given in the supplementary material.<sup>36</sup> The states <sup>1</sup>Σ<sub>g</sub><sup>+</sup> and <sup>1</sup>Σ<sub>u</sub><sup>+</sup> can be placed in the first category as their tunneling contributions are from higher vibrational levels with small FC factors. The states <sup>1</sup>Σ<sub>g</sub><sup>-</sup>, <sup>1</sup>Σ<sub>u</sub><sup>-</sup>, <sup>1</sup>Π<sub>u</sub>, <sup>1</sup>Π<sub>g</sub>, <sup>2</sup>Σ<sub>g</sub><sup>+</sup>, <sup>2</sup>Σ<sub>u</sub><sup>+</sup> fall in the second category. From Figure 8,

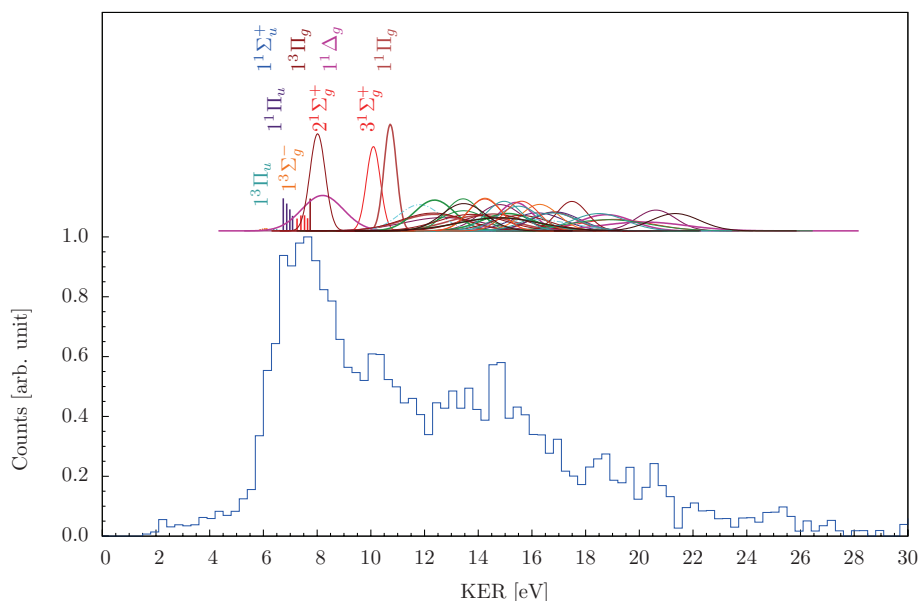


FIG. 6. Experimental and theoretical KER distributions for the channel  $N_2^{++} \rightarrow N^+:N^+$ . Corrected experimental KER distribution shown by histogram in lower panel. Upper panel (offset by 1.05) shows the KER distribution arising from repulsive states of  $N_2^{++}$  (Gaussian curves) and the contribution from tunneling of vibrational levels (bars).

it can be seen that the KER from tunneling vibrational levels of these electronic states ranges from about 6.0 eV (for  $1^3\Sigma_g^-$  state) up to 8.0 eV (for the  $1^3\Pi_g$  state). In fact, all meta-stable vibrational levels of these states have very small FC factors, the largest value being 0.1. These vibrational levels have life times of up to few milliseconds. If tunneling were the only decay mechanism, then only these state levels would contribute to the CSD channel. Although the  $1^1\Delta_g$  state is deep enough to support five vibrational states, all of them have very small FC factors (due to minimum being far away from FC region).

This state crosses to several other electronic states having stable vibrational states and hence may indirectly contribute to KER.

The experimental KER distribution shows distinctive peaks around 6.5 eV, 7.5 eV, 10.0 eV, and 15.0 eV. The electronic states responsible for the first two peaks are clearly the meta-stable states identified above. The peak around 10.0 eV can be attributed clearly to the repulsive states  $3^1\Sigma_g^+$  and  $1^1\Pi_g$ , giving rise to KER values centered at 10.01 eV and 10.72 eV. This is to be contrasted with the report of Lundqvist

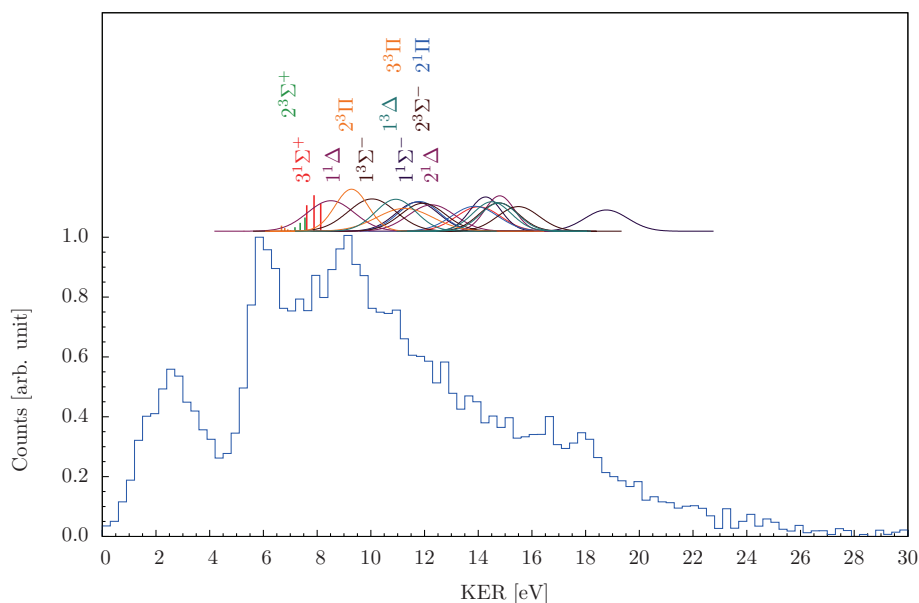


FIG. 7. Experimental and theoretical KER distributions for the channel  $CO^{++} \rightarrow C^+:O^+$ . Corrected experimental KER distribution shown by histogram in lower panel. Upper panel (offset by 1.05) shows the KER distribution arising from repulsive states of  $CO^{++}$  (Gaussian curves) and the contribution from tunneling of vibrational levels (bars).

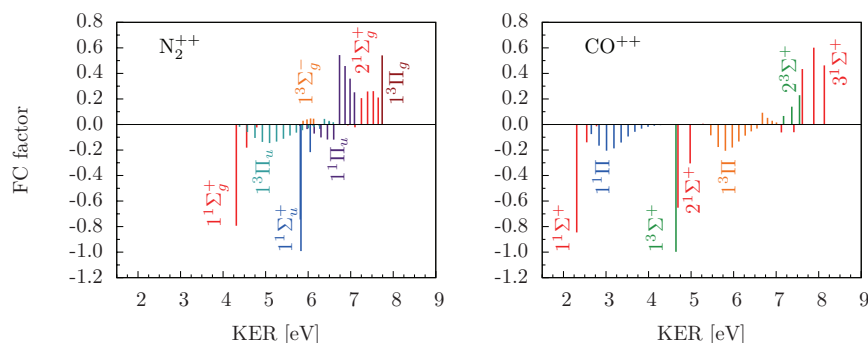


FIG. 8. Vibrational levels of  $N_2^{++}$  and  $CO^{++}$  having FC factor greater than  $10^{-3}$  are shown with respect to the KER that would be obtained upon dissociation from this state. Each vibrational level is shown by a bar of height equal to the FC factor. The FC factors for vibrational levels which are found to be stable against tunneling are shown with negative sign. The positive FC factors have been multiplied by 5.0 to enhance their visibility.

*et al.*,<sup>6</sup> who had tentatively assigned the broader KER structure at 10 eV to the purely repulsive  $1^1\Pi_g$  state. Lundqvist *et al.*<sup>6</sup> have observed the feature at 15 eV but have provided explanation for features only up to 12 eV, based on the calculations by Senekowitsch *et al.*<sup>24</sup> and Olsson *et al.*,<sup>23</sup> the latter being limited in the number of PECs calculated. As shown in Figure 6, a large number of higher lying states which are purely repulsive in the FC region contribute to the KER distribution at higher energies. Since the state density in this range is very high, it is not possible to make an exact correspondence between the state and the structures in the KER distribution beyond 11 eV. However, our calculations do predict a large number of states around a KER value of 15.0 eV, where the experimental spectrum also shows a prominent feature. It is interesting to note that this feature is hardly seen in the raw KER spectrum, emphasizing the importance of correcting the raw KER spectra for losses and inefficiencies of the spectrometer; this will be seen once again in the KER spectrum of CSD of  $CO^{++}$ .

Now, we consider CO and referring to Figures 5 and 8 and Table C 2 given in the supplementary material.<sup>36</sup> The states  $1^1\Sigma^+$ ,  $1^1\Pi$ , and  $1^3\Sigma^+$  can be identified to belong to the first category. These states have several stable vibrational levels and tunneling occurs only for levels that are very high. The FC factors for these high vibrational levels are very small. On the other hand,  $1^3\Pi$ ,  $2^1\Sigma^+$ ,  $3^1\Sigma^+$ , and  $2^3\Sigma^+$  are in the second category. These states support vibrational levels which have modest FC factors (about 0.02 to 0.1) and dissociate through tunneling.

In contrast to  $N_2^{++}$ , the KER distribution for CSD of  $CO^{++}$  has a much richer structure. It has a relatively broad low-intensity peak at 2.8 eV which is well-separated from two narrower peaks at 6.0 eV and 9.5 eV. From Figure 8, it can be seen that the vibrational states with significant tunneling contribute to KER starting from 6.7 eV (for  $1^3\Pi$  state) up to 8.0 eV (for  $3^1\Sigma^+$  state). If only tunneling were the sole mechanism for dissociation, there would be no contribution from vibrational levels to KER values less than 6.7 eV. Therefore, the KER peaks at 2.8 and 6.0 eV cannot be explained without invoking other dissociation mechanisms. As shown in upper panel of Figure 7, at higher KER values beyond 8.6 eV only repulsive states contribute, starting with states  $1^1\Delta$  and  $2^3\Pi$ , readily explaining the KER peak at 9.5 eV.

Apart from tunneling, two other dissociation mechanisms are possible. The first mechanism is based on predissociation where the stable vibrational states of an electronic state couple to continuum states of a repulsive state via non-adiabatic, spin-orbit and other interactions leading to dissociation. From Figure 5, the states  $1^3\Sigma^-$ ,  $1^1\Delta$ , and  $2^3\Pi$  are the possible candidates through which some of the seven electronic states belonging to first and second category may undergo predissociation. Assuming weak coupling of crossing states, the vibrational levels closest to the crossing point will contribute significantly to predissociation. The FC factors of such vibrational levels pre-dissociating through  $1^1\Delta$  and  $2^3\Pi$  states are found to be insignificant (less than 0.005) and these levels are unlikely to be populated. The KER values for predissociation of  $1^3\Sigma^-$  state through different states are as follows.  $1^1\Sigma^+$ : 6.56 and 6.78 eV,  $2^1\Sigma^+$ : 9.76 eV,  $1^1\Pi$ : 6.35 eV,  $1^3\Sigma^+$ : 8.24 eV,  $1^3\Pi$ : 6.12 eV. The FC factors are significant ( $>0.1$ ) only for  $1^1\Pi$  and  $1^3\Pi$  states. Therefore, the KER peak at 6.0 eV will receive significant contributions from both of these states. Tarisien *et al.*<sup>10</sup> have identified the origin of this peak to be the vibrational levels of  $1^3\Pi$  state; our calculated PECs enable us to clarify that this happens through strong predissociation of  $3^1\Pi$  and  $1^1\Pi$  states via repulsive  $3^1\Sigma^-$  state and not via tunneling.

Although predissociation from lower vibrational levels may contribute to KER below 6.0 eV (estimated lower limit is 2.3 eV), the couplings are not expected to be significant as these levels are far from the relevant crossing-points. Therefore, it is not possible to explain the KER peak at 2.8 eV on the basis of predissociation. A possible mechanism is dissociation from a highly excited electronic state of singly ionized  $CO^{+*}$  lying between the lowest CSD asymptote of  $CO^{++}$  and the double-ionization threshold of CO (the latter is about 5.5 eV above the former). Such a state, if accessed during electron-impact ionization, will be autoionizing and undergoes dissociation to the lowest CSD asymptote of  $CO^{++}$ . This possibility has been established by Hsieh and Eland<sup>3</sup> who report that the KER distribution arising purely from autoionization of  $CO^{+*}$  extends up to 4.7 eV KER. Their reported distribution is very similar to ours. This channel has been further investigated by Osipov *et al.*,<sup>5</sup> who have proposed that  $CO^{+*}$  first dissociates to  $C^+$  and  $O^*$ , followed by  $O^*$  autoionizing to  $O^+$ .

The main reasons for differences in the KER spectra of the two species can be understood qualitatively with the aid of the PECs shown in Figures 4 and 5. The crossing of the meta-stable states with repulsive states occurs at a much larger bond-distance from the FC region in  $N_2^{++}$  as compared to  $CO^{++}$ . In  $N_2^{++}$ , these crossings occur only beyond 1.5 Å, whereas in  $CO^{++}$ , several such crossings (with  $1^3\Sigma^-$  and  $1^1\Delta$  repulsive states) occur within 1.5 Å. Further, in  $N_2^{++}$ , most of the repulsive states involved in crossings are not effective because they dissociate to the same asymptote as the meta-stable states they cross with. In contrast, in  $CO^{++}$ , most meta-stable states (except  $1^3\Pi$ ) dissociate to a higher asymptote ( $C^+{:}^2P$  and  $O^+{:}^2D$ ), whereas the repulsive state  $1^3\Sigma^-$  which crosses with most of them dissociates to the lowest asymptote ( $C^+{:}^2P$  and  $O^+{:}^4S$ ). Since only triplet and quintet states are possible for the lowest asymptote in  $CO^{++}$ , all the singlet states necessarily dissociate into a higher asymptote. The calculations of spin-orbit interaction by Sedivcova *et al.*<sup>27</sup> show that in  $CO^{++}$ ,  $1^3\Sigma^-$  has strong coupling with  $1^1\Sigma^+$  and  $1^1\Pi$  states which are facile pre-dissociation channels.

## B. CSD-to-ND ratios

The experimental values of the CSD-to-ND ratios for  $N_2^{++}$  and  $CO^{++}$ , after applying all corrections, are 0.07 and 0.56, respectively. In the case of  $CO^{++}$ , both predissociation and autoionization contribute to CSD, which is clearly not the case for  $N_2^{++}$ . If only autoionization of highly excited states of  $CO^{++}$  contributes as major source of indirect process, CSD-to-ND ratio would be comparable to the CSD-to-ND ratio of  $N_2^{++}$  (region  $r_1$  in Figure 9). If we exclude the contribution to CSD arising from autoionization by removing the counts in KER distribution up to 4.7 eV (region  $r_1$  in Figure 9) and instead include those counts in the ND channel, the CSD-to-ND ratio becomes 0.44. Further, if predissociation of  $1^1\Pi$  and  $1^3\Pi$  through  $1^3\Sigma^-$  is separated collectively with the autoionization contribution by removing all counts from the KER distribution up to 7.2 eV (region  $r_1$  and  $r_2$ ) and instead considering them as non-dissociative, the CSD-to-ND ratio will become 0.32 that is again more than four times larger than  $N_2^{++}$  case. As seen earlier, predissociation through  $1^3\Sigma^-$  can in fact contribute up to 9.8 eV and beyond. Even if we make the drastic assumption that all counts in KER distribution of  $CO^{++}$  up to 10.8 eV arise from predissociation and autoionization (region  $r_1$ ,  $r_2$ , and  $r_3$ ) and exclude them from the CSD yield, though there will be a significant contribution in that KER range from repulsive curves, the CSD-to-ND ratio is 0.17. Even after accounting for the contributions of indirect dissociation process that could be identified in this study, the CSD-to-ND is higher in CO by a factor of 2. This shows that predissociation from higher lying states that will contribute in the KER spectrum above 9.8 eV is still significant. Though, in the range above 9.8 eV, identification of KER features is not possible, the underlying mechanism is profoundly non-adiabatic, as in the lower KER range.

Since the total FC factors for these molecules are quite similar, we can assume that total number of dication molecules produced are roughly equal. Moreover, the total

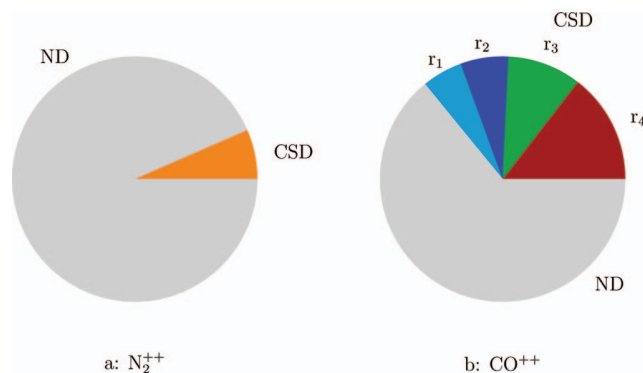


FIG. 9. CSD and ND fractions of (a)  $N_2^{++}$  and (b)  $CO^{++}$  are shown in the figure. In case of  $CO^{++}$ , CSD yield is shown in four parts as discussed in the text. Region  $r_1$  represents CSD fraction corresponding to KER values below 4.7 eV. This region covers autoionization of high lying states of  $CO^{++}$ . CSD corresponding to the KER range from 4.7 to 7.2 eV largely arises from predissociation of  $1^1\Pi$  and  $1^3\Pi$  through  $1^3\Sigma^-$  and is shown as region  $r_2$ . Region  $r_3$  covers counts in the KER spectrum up to 10.8 eV that can arise from all known possible predissociation and autoionization channels (for details, see text). Region  $r_4$  represents counts corresponding to KER value greater than 10.8 eV.

double ionization cross section for these molecules are nearly identical.<sup>28</sup> We can, therefore, estimate the ratio of total non-dissociative cross-sections of both dication as well as the ratio of their CSD cross-sections based on the observed CSD-to-ND ratios. The non-dissociative cross-section of  $N_2^{++}$  thus turns out to be 1.46 times that of  $CO^{++}$ , while the CSD cross-section of  $CO^{++}$  turns out to be more than 5 times that of  $N_2^{++}$ , which is also seen in Figure 9. The discussions at the end of Subsection IV A based on features of PECs provide support for this conclusion.

## V. CONCLUSIONS

We have performed a combined experimental and theoretical comparative analysis of the CSD of  $N_2^{++}$  and  $CO^{++}$  molecular ions. For both dications, we have provided a comprehensive set of PECs using MRCI calculations at the level of the cc-pV5Z basis set. The KER spectrum for CSD of these dications has been determined and the importance of correcting the raw experimental KER data for transmission losses and detection inefficiencies prior to interpretation has been emphasized. An approximate excitation probability function is taken into consideration in determining the contribution to the KER from a particular excitation. The major features of the KER spectrum of CSD have been clarified on the basis of *ab initio* calculations of the PECs. With the help of calculated PECs and their KER, we could resolve a few unidentified structures in the observed KER spectrum that have been either not attempted or not fully understood earlier. While the KER spectrum of  $N_2^{++}$  can be readily explained in terms of repulsive or tunneling states, in the case of  $CO^{++}$ , recourse has to be taken to indirect dissociation channels, namely, predissociation and autoionization.

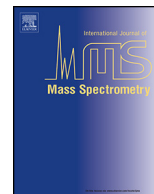
The CSD-to-ND ratio for these dications has been estimated from experimental data and found to be much larger

in the case of  $\text{CO}^{++}$  as compared to  $\text{N}_2^{++}$ . The relative significance of direct and indirect processes is found to have a bearing on the CSD-to-ND ratios. By exploiting the information about the sources of the features in the KER spectra of the two species, we have been able to separate out the autoionization and predissociation contributions in the lower range of KER values to the overall dissociative yield. These indirect processes do not contribute as much to CSD in the case of  $\text{N}_2^{++}$  as they do in the case of  $\text{CO}^{++}$ , and this partially explains the higher CSD-to-ND ratio for  $\text{CO}^{++}$ . Since autoionization and curve-crossing predissociation processes fall under non-BO dynamics,<sup>39</sup> our work shows that these processes play a significant role in the CSD of  $\text{CO}^{++}$ , but not much in the case of  $\text{N}_2^{++}$ , indicating the effect of asymmetry in non-BO dynamics.<sup>40</sup>

## ACKNOWLEDGMENTS

A.P. wishes to thank IISER Mohali for hospitality during the course of this work. A.P. and B.B. would like to thank K. P. Subramanian, S. B. Banerjee, I. A. Prajapati, and K. Saha for the assistance during the experiment.

- <sup>1</sup>D. Mathur, *Phys. Rep.* **391**, 1 (2004).
- <sup>2</sup>T. Masuoka, *J. Chem. Phys.* **101**, 322 (1994).
- <sup>3</sup>S. Hsieh and J. H. D. Eland, *J. Phys. B* **29**, 5795 (1996).
- <sup>4</sup>M. Lucchini, K. Kim, F. Calegari, F. Kelkensberg, W. Siu, G. Sansone, M. J. J. Vrakking, M. Hochlaf, and M. Nisoli, *Phys. Rev. A* **86**, 043404 (2012).
- <sup>5</sup>T. Osipov, Th. Weber, T. N. Rescigno, S. Y. Lee, A. E. Orel, M. Schöffler, F. P. Sturm, S. Schössler, U. Lenz, T. Havermeier, M. Kühnel, T. Jahnke, J. B. Williams, D. Ray, A. Landers, R. Dörner, and A. Belkacem, *Phys. Rev. A* **81**, 011402 (2010).
- <sup>6</sup>M. Lundqvist, D. Edvardsson, P. Baltzer, and B. Wannberg, *J. Phys. B* **29**, 1489 (1996).
- <sup>7</sup>Z. Wu, C. Wu, X. Liu, Y. Deng, Q. Gong, D. Song, and H. Su, *J. Phys. Chem. A* **114**, 6751 (2010).
- <sup>8</sup>M. Lundqvist, P. Baltzer, D. Edvardsson, L. Karlsson, and B. Wannberg, *Phys. Rev. Lett.* **75**, 1058 (1995).
- <sup>9</sup>P. Lablanquie, J. Delwiche, M.-J. Hubin-Franskin, I. Nenner, P. Morin, K. Ito, J. H. D. Eland, J.-M. Robbe, G. Gandara, J. Fournier, and P. G. Fournier, *Phys. Rev. A* **40**, 5673 (1989).
- <sup>10</sup>M. Tarisien, L. Adoui, F. Frémont, D. Lelièvre, L. Guillaume, J.-Y. Chesnel, H. Zhang, A. Dubois, D. Mathur, S. Kumar, M. Krishnamurthy, and A. Cassimi, *J. Phys. B* **33**, L11 (2000).
- <sup>11</sup>J. H. D. Eland, M. Hochlaf, G. C. King, P. S. Kreymin, R. J. LeRoy, I. R. McNab, and J.-M. Robbe, *J. Phys. B* **37**, 3197 (2004).
- <sup>12</sup>F. Penent, R. I. Hall, R. Panajotović, J. H. D. Eland, G. Chaplier, and P. Lablanquie, *Phys. Rev. Lett.* **81**, 3619 (1998).
- <sup>13</sup>J. Rajput, S. De, A. Roy, and C. P. Safvan, *Phys. Rev. A* **74**, 032701 (2006).
- <sup>14</sup>I. Ben-Itzhak, S. G. Ginther, V. Krishnamurthi, and K. D. Carnes, *Phys. Rev. A* **51**, 391 (1995).
- <sup>15</sup>T. Mizuno, T. Yamada, H. Tsuchida, Y. Nakai, and A. Itoh, *Phys. Rev. A* **81**, 012704 (2010).
- <sup>16</sup>J. H. D. Eland, *Chem. Phys.* **294**, 171 (2003).
- <sup>17</sup>O. Furuhashi, T. Kinugawa, S. Masuda, C. Yamada, and S. Ohtani, *Chem. Phys. Lett.* **337**, 97 (2001).
- <sup>18</sup>M. Ahmad, P. Lablanquie, F. Penent, J. G. Lambourne, R. I. Hall, and J. H. D. Eland, *J. Phys. B* **39**, 3599 (2006).
- <sup>19</sup>M. Hochlaf, R. I. Hall, F. Penent, H. Kjeldsen, P. Lablanquie, M. Lavollée, and J. H. D. Eland, *Chem. Phys.* **207**, 159 (1996).
- <sup>20</sup>D. Mathur, L. H. Andersen, P. Hvelplund, D. Kella, and C. P. Safvan, *J. Phys. B* **28**, 3415 (1995).
- <sup>21</sup>J. P. Bouhnik, I. Gertner, B. Rosner, Z. Amitay, O. Heber, D. Zajfman, E. Y. Sidky, and I. Ben-Itzhak, *Phys. Rev. A* **63**, 032509 (2001).
- <sup>22</sup>L. H. Andersen, J. H. Posthumus, O. Vahtras, H. Ågren, N. Elander, A. Nunez, A. Scrinzi, M. Natiello, and M. Larsson, *Phys. Rev. Lett.* **71**, 1812 (1993).
- <sup>23</sup>B. Olsson, G. Kindvall, and M. Larsson, *J. Chem. Phys.* **88**, 7501 (1988).
- <sup>24</sup>J. Senekowitsch, S. O'Neil, P. Knowles, and H. J. Werner, *J. Phys. Chem.* **95**, 2125 (1991).
- <sup>25</sup>F. R. Bennett, *J. Chem. Phys.* **103**, 3613 (1995).
- <sup>26</sup>V. Krishnamurthi, K. Nagesha, V. R. Marathe, and D. Mathur, *Phys. Rev. A* **44**, 5460 (1991).
- <sup>27</sup>T. Šedivcová, P. R. Žďánská, V. Špirko, and J. Fišer, *J. Chem. Phys.* **124**, 214303 (2006).
- <sup>28</sup>Y.-K. Kim, K. K. Irikura, and M. A. Ali, *J. Res. Natl. Inst. Stand. Technol.* **105**, 285 (2000).
- <sup>29</sup>J. Ullrich, R. Moshhammer, A. Dorn, R. Dörner, L. Ph. H. Schmidt, and H. Schmidt-Böcking, *Rep. Prog. Phys.* **66**, 1463 (2003).
- <sup>30</sup>V. Sharma and B. Bapat, *Eur. Phys. J. D* **37**, 223 (2006).
- <sup>31</sup>G. W. Fraser, *Int. J. Mass Spectrom.* **215**, 13 (2002).
- <sup>32</sup>E. Liénard, M. Herbane, G. Ban, G. Darius, P. Delahaye, D. Durand, X. Fléchar, M. Labalme, F. Mauger, A. Mery, O. Naviliat-Cuncic, and D. Rodríguez, *Nucl. Instrum. Methods Phys. Res. A* **551**, 375 (2005).
- <sup>33</sup>H.-J. Werner, P. J. Knowles, G. Knizia, F. R. Manby, and M. Schütz, *Wiley Interdiscip. Rev.: Comput. Mol. Sci.* **2**, 242 (2012).
- <sup>34</sup>See <http://cccbdb.nist.gov> for the calculation of energy states (Release 15b, August 2011).
- <sup>35</sup>Y.-K. Kim and J.-P. Desclaux, *Phys. Rev. A* **66**, 012708 (2002).
- <sup>36</sup>See supplementary material at <http://dx.doi.org/10.1063/1.4861665> for the details of calculation.
- <sup>37</sup>R. J. Le Roy, see <http://leroy.uwaterloo.ca/programs/> for the details of LEVEL8.0 program, 2007.
- <sup>38</sup>L. D. Landau and E. M. Lifshitz, *Quantum Mechanics Non-Relativistic Theory* (Pergamon Press, 1991), Vol. 3, p. 148.
- <sup>39</sup>J. N. Bardsley, *Chem. Phys. Lett.* **1**, 229 (1967).
- <sup>40</sup>R. S. Berry, *J. Chem. Phys.* **45**, 1228 (1966).



# Effect of transmission losses on measured parameters in multi-ion coincidence momentum spectrometers



Amrendra Pandey\*, B. Bapat

Physical Research Laboratory, Ahmedabad 380009, India

## ARTICLE INFO

### Article history:

Received 13 December 2013

Received in revised form 25 January 2014

Accepted 27 January 2014

Available online 4 February 2014

### PACS:

34.50 Gb

34.80 Gs

39.90.+j

### Keywords:

Multi-coincidence spectrometers

Ion transmission losses

Loss corrections

## ABSTRACT

We address the effect of transmission losses on the measured kinematic parameters of molecular fragmentation processes in a time-of-flight based ion momentum spectrometer. We suggest means to correct for these losses for two-body fragmentation having isotropic distribution. As an example, we discuss the kinetic energy release spectrum observed in recoil ion momentum spectrometer of doubly ionized nitrogen molecules formed upon high energy electron impact. Further, we highlight the difficulties in calculating losses in many-body fragmentation and anisotropic emissions and show that such effects cannot be accounted without employing additional information about the process. In many cases, such information cannot be extracted from the observed data in the experiment and thus we have to rely on careful assumptions.

© 2014 Elsevier B.V. All rights reserved.

## 1. Introduction

Dissociative ionization of molecules is a much studied process as it is a prototype for the evolution of a quantum mechanical many-body system from a bound state to a multi-particle continuum. Since the time scales of ionization and dissociation are quite different, the DI process is seen as a two-step process – electron removal, followed by separation of atoms and ions constituting the molecule. The formation of a transient molecular ion marks the division of the two steps, and a study of the kinematics of the dissociating partners is a means to discovering the properties of the transient molecular ion. The advent of the sophisticated experimental technique of multi-particle coincidence momentum imaging has propelled such studies immensely, enabling near-complete measurement of the kinematics of the fragments in many instances. Several parameters that characterize the DI process, such as kinetic energy release (KER) spectrum [1–3], studies concerning the metastable molecular ions [4,5], anisotropy of the fragmentation [6,7] as well as cross sections and branching ratios [8–13] of various channels have been investigated for many molecules. Since, literature is very extensive on the properties of dissociative ionization, we are mentioning a few references, preferably on diatomic molecules, on these kinematical parameters. The greatest power

of this technique lies in its ability to address the dynamical evolution of the unstable or metastable molecular ions by measuring the complete momentum vector of each fragment created in the fragmentation process, covering thereby the complete phase space spanned by the fragments. Thus, at least in principle, it becomes possible to obtain very high order differential cross-sections for these processes – encompassing, naturally, the commonly known and useful kinetic energy and angular distributions of the fragments [14–18].

In this article, we present an analysis of the errors in measured kinetic energy release (KER) distribution, anisotropy and relative cross sections arising because of energy dependent transmission of the ions through the spectrometer. We first discuss means to calculate the transmission loss factor for a charged particle for isotropic and anisotropic distributions. We then obtain the loss factor for two-body fragmentation and the corrections to the KER spectrum assuming isotropic distribution of fragmentation. As an illustration, we analyze the KER distribution of charge symmetric breakup of doubly ionized  $N_2$  molecule. The correction because of dead time loss for this channel has also been taken into account. We address the problem of obtaining a general function for loss factor correction for three-body fragmentation. The problem of determining anisotropy if the losses are present is also discussed. We find that in cases where anisotropy exists, losses cannot be accounted for on the basis of the recorded data alone, precluding a conclusion about the nature of the anisotropy. In addition to the losses discussed here, there are other losses due to non-ideal transmission

\* Corresponding author. Tel.: +91 7926314561.

E-mail addresses: [amrendra@prl.res.in](mailto:amrendra@prl.res.in), [amrendra.akp@gmail.com](mailto:amrendra.akp@gmail.com) (A. Pandey).

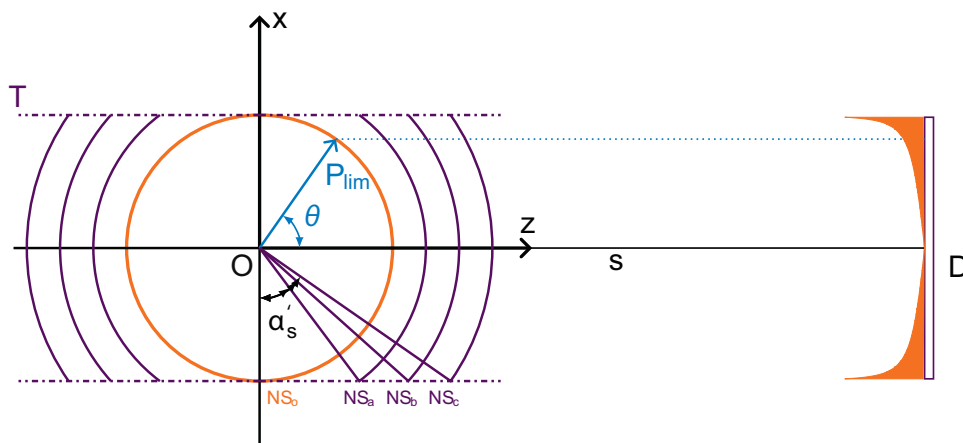


**Fig. 1.** A cross sectional view of Newton sphere,  $NS_0$  of radius  $P_{lim}$ , centered at  $O$  is shown in the  $y$ -plane. Three other Newton spheres,  $NS_a$ ,  $NS_b$ ,  $NS_c$  corresponding to momentum greater than  $P_{lim}$  are shown truncated. Only the part of the Newton spheres shown here will be within detector size upon transportation, the remaining part will not be detected. The lost part of the Newton spheres is parametrized by  $\alpha$ , the complement of the polar angle made by the radius vector at the point of intersection of the Newton sphere with the tangent ( $T$ )  $x = P_{lim}$ .  $s$  is the distance between the ionization region and the detector  $D$ .  $\theta$  is the polar angle defined with respect to spectrometer ( $z$ -)axis. The projection of the Newton sphere,  $NS_0$  is shown by the shaded area on the detector. For simplicity, the conversion factor from momentum space to the distance is taken to be unity, and thus the range of the projection on the detector plane is shown having same radius as of the Newton sphere.

of the meshes in the spectrometer and inefficiency of the detectors, which though important, are separate from the main issue of this article. A discussion of these factors can be found in Ma et al. [19] and Liénard et al. [20].

**2. Measurement of kinematic parameters**

In most collision experiments the initial orientation of molecules before interaction with the projectile is generally random, though induced orientation may be seen in the case of intense laser ionization [21]. Molecular fragmentation rarely results in a unique fragment kinetic energy value and thus there will be a set of Newton spheres for a given ion created in the fragmentation process centered at ionization source. In an ion momentum spectrometer the measurement of the momentum vectors is usually carried out by transporting and projecting the ions by means of electric and magnetic fields on to a planar imaging detector. The component of the momentum parallel to the spectrometer axis is obtained from the time-of-flight (ToF) of the ion after passing through the electric and magnetic fields [22]. For a given ion ToF a correspondence between the observed position on the detector plane with the Newton sphere is maintained in experiments and is used to calculate the other two momentum components perpendicular to the spectrometer axis by inverse mapping.

There is an upper limit on the kinetic energy for a given ion for complete transmission of the Newton sphere, introducing two type of imperfections in the observed quantities. First, the relative distribution of Newton spheres of different ions observed in the fragmentation process gets distorted. Second, the distribution of high energy ions of a particular species may appear to be anisotropic, when in fact it is merely that ions emitted in certain directions could not be transmitted to the detector. Furthermore, since loss depends on the kinetic energy of the ions, the loss fraction of a given species for two different fragmentation pathways will be different depending upon their kinematics, resulting in distortion of the relative cross sections for different fragmentation pathways.

**3. Analysis of losses**

A schematic diagram of the spectrometer and a typical Newton sphere centered at the ideal point source (taken as the origin) are shown in Fig. 1. The  $+z$ -axis is the spectrometer axis, along which

extraction fields are applied. The detector plane is at  $z = s$ . The region between the source and the detector may have one or more fields, or a field free region; these details do not significantly alter the discussion to follow. Ions on a given Newton sphere of radius  $P$ , will have a range of flight times distributed around a value  $t_0$  corresponding to the flight time  $t_0$  of ions created in  $z = 0$  plane on the Newton sphere. Because there is no field applied in the transverse direction, transverse momentum  $\mathbf{P}_\perp$  is not affected in transmission to the detector. As a result, there is a one to one correspondence between the position on the detector plane and the points on the Newton sphere. The mapping of the Newton sphere from momentum space to the detector plane is given by the equations  $\mathbf{r} = t \mathbf{P}_\perp / m$ . The flight time and the longitudinal component of the momentum are related by a one-to-one function depending on the spectrometer parameters. When the ion kinetic energy  $P^2/2m$  is much less than the energy gain in the extraction field,  $qE_s$ , to a good approximation, we have  $t_0 - t = P_\parallel / qE_s$ . The distribution of the intensity on the detector plane, shown in Fig. 1 by shaded area, is for an isotropic Newton sphere and has been discussed by Amitay et al. [23]. Note that the projection of the Newton sphere on the detector plane has its maximum at  $\theta = \pi/2$  and decreases rapidly for smaller  $\theta$ . This point will be again emphasized in Section 4.1.

An ion formed in the ionization region will be detected only when  $P_\perp \leq R \times m/t$ , where  $R$  is the active radius of the detector. Corresponding to the limiting value  $P_{\perp lim}$  beyond which loss starts, is an angle  $\alpha = \cos^{-1}(P_{\perp lim}/P)$ , Fig. 1, which parametrizes the lost part of the Newton sphere. The solid angle corresponding to the portion of the Newton sphere that will fall outside the detector is  $4\pi \sin(\alpha)$ . So the loss factor for isotropic emission of particles is

$$LF(P) = \sin \left( \cos^{-1} \left( \frac{P_{\perp lim}}{P} \right) \right) \tag{1}$$

For the anisotropic case, if function  $f(\theta, P) : 0 < \theta < \pi$  represents the anisotropy of Newton sphere of radius  $P$ , then the loss factor for the momentum  $P$  will be given by

$$LF(P) = \frac{\int_{\pi/2-\alpha}^{\pi/2+\alpha} f(\theta, P) \sin(\theta) d\theta}{\int_0^\pi f(\theta, P) \sin(\theta) d\theta} \tag{2}$$

Note that in Eq. (2),  $\theta$  is defined with respect to the spectrometer axis to simplify the expressions. If the Newton sphere has anisotropy about some other axis (e.g. the projectile beam), the function  $f(\theta, P)$  must be defined accordingly.

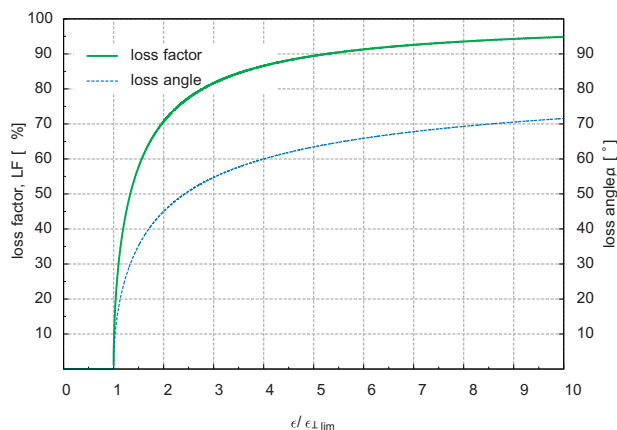


**Fig. 2.** Loss angle and loss factor for an ion are shown as a function of multiples of  $\epsilon_{\perp \text{lim}}$ . There will be no transmission loss for Newton spheres having radius less than  $\epsilon_{\perp \text{lim}}$ .

It is useful to rewrite the loss factor in terms of particle's kinetic energy  $\epsilon$ . Corresponding  $P_{\perp \text{lim}}$  we define  $\epsilon_{\perp \text{lim}} = P_{\perp \text{lim}}^2/2m$ , in terms of which the loss factor for isotropic distribution is

$$LF(\epsilon) = \left(1 - \frac{\epsilon_{\perp \text{lim}}}{\epsilon}\right)^{1/2} \quad (3)$$

The loss angle and loss factor as a function of the particle's energy are plotted in Fig. 2.

#### 4. Effect of losses on kinematic parameters in a two-body breakup

In a fragmentation leading to two or more atoms or ions, the sum of the kinetic energies of the fragmentation partners, also called the kinetic energy release (KER) is of interest.

Consider a fragmentation process  $AB \rightarrow A + B$  ( $m_A \leq m_B$ ), with  $KER = \epsilon_A + \epsilon_B$ . The conservation of linear momentum implies ( $\epsilon_A \times m_A = \epsilon_B \times m_B$ ) that the lighter fragment will always have larger kinetic energy. Consequently the loss factor will be effectively determined by the loss of lighter fragment and the limiting value of the kinetic energy up to which there is complete collection will be given by

$$KER_{\text{lim}} = \epsilon_{A \perp \text{lim}} \times \left(1 + \frac{m_A}{m_B}\right) \quad (4)$$

In terms of KER, the loss factor for two-body fragmentation can be written as

$$LF(KER) = \left[1 - \frac{KER_{\text{lim}}}{KER}\right]^{1/2} \quad (5)$$

The loss factor is a function of the kinetic energy of an ion, but independent of its mass. Since in a two-body breakup the kinetic energies of the partners are in inverse proportion of their masses, the loss factors will in general be different for the two fragments. This characteristic affects the measured energy-differential and partial cross-sections as well as the branching ratios. More importantly, since the loss angle for lighter species is always larger than the heavier one, many pair coincidences will be recorded as singles in two-body fragmentation. For many-body fragmentation having additional complications, multiple fragmentation events will be recorded as a lower order events than they truly are. This means that in most cases the measured branching ratio for multiple ion fragmentation will be incorrect. However, for a pair breakup in which the kinetic energy is measured, a reasonable correction can be applied because of a peculiar property of a ToF device. An ion emitted along the axis of a ToF device will be recorded without

discrimination (as is the case for high KE ions emitted at large angles to the spectrometer axis). Hence the upper limit of the kinetic energy of the ion will be known from the ToF distribution even for an otherwise lossy spectrometer. The limiting KE value  $\epsilon_{\text{lim}}$  for complete transmission can be obtained analytically or by a particle trajectory simulation for the given spectrometer configuration as described earlier. Thus the loss factor for that ion can be well accounted for and hence the correction to the partial cross-section for that species can be readily made.

Another loss factor comes in due to the deadtime ( $t_d$ ) of the detector and the signal processing electronics. If the two ions in a breakup have nearly equal flight times, then they may not be detected as separate particles, thereby reducing the apparent (observed) yield for that channel. The problem is particularly important when the two ions have the same  $m/q$  ratio. The general expression for ToF of an ion can be written as

$$t = a \left(\frac{m}{q}\right)^{1/2} - \frac{P_{\parallel}}{qE_s} \quad (6)$$

where  $E_s$  is the field strength in the extraction region and  $a$  is related to other spectrometer parameters. Since two identical ions (such as  $N^+$ ,  $N^+$  from the breakup of  $N_2^+$ ) will always have the same magnitude of the momentum, they will be detected as separate only when their parallel components of momentum satisfy the condition ( $2P_{\parallel}/qE_s > t_d$ ). This means that for any value of KER in a two-body breakup, there will be a loss of detected ion pair coincidences. From this relationship, we find that for isotropic emission the loss fraction due to deadtime reduces with the radius  $\sqrt{\epsilon}$  of the Newton sphere being sampled as  $t_d q E_s / \sqrt{8m\epsilon}$ . A discussion on the loss because of the deadtime can be found in Ali et al. [24].

##### 4.1. Case analysis

The process studied is electron-impact dissociative double ionization of  $N_2$ . There are many fragmentation channels observed in the experiment, here we take one channel for analysis of loss correction:



This fragmentation channel does not indicate any metastable properties for transient ion  $N_2^{++}$ . Fragmentation channels involving metastability that have been observed in many cases [25], would be rather complicated to analyze for loss corrections and is not discussed here. In the experiment, molecular ions are created by high energy (1.3 keV) electron impact on an effusive molecular beam in a crossed-beams geometry. The ions are mass and momentum analyzed by a recoil ion momentum spectrometer (RIMS) as described in [26]. In brief, RIMS consists a single field time-of-flight (ToF) mass spectrometer combined with a multi-hit capable, large area, position-sensitive detector based on a microchannel plate and a delayline anode. The active diameter of MCPs detectors used in the setup is 76 mm. A uniform electric field of  $60 \text{ V cm}^{-1}$  is applied to extract the ions. The length of the accelerating region is 110 cm, followed by a field-free drift region of 220 mm. Ion time-of-flight is measured by an electron-ion coincidence. Measuring the time-of-flight is a means to separate the ions and to obtain the component of initial momentum parallel to the spectrometer axis. The two transverse components are obtained by measuring, in addition, the position of hit ( $x, y$ ) of the ion on the detector plane after flying through extraction and drift region by delayline anode. Collision rates are kept sufficiently low to avoid false coincidences, enabling the determination of correlated kinematics between ionic fragments. The time-of-flight and position data can be converted event-by-event into a momentum map of the fragments and used

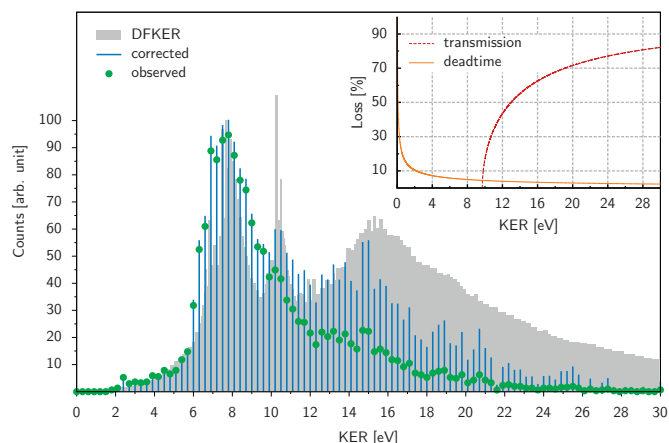


**Fig. 3.** KER distribution for the fragmentation channel  $N_2^{++} \rightarrow N^+:N^+$  is shown. The observed KER from RIMS setup [26], operated in the condition described in the text, is shown by dots. The KER distribution corrected for the transmission loss and dead time loss is shown by vertical lines. Up to 9.70 eV, transmission loss because of finite detector size is zero, however the dead time loss decreases with KER and thus effective for the lower KER range. Loss factors due to incomplete transmission and finite deadtime are shown in the inset. Our spectrum is compared with the Doppler-free measurement of the KER distribution (DFKER) by Lundqvist et al. under 200 eV electron impact [1].

reproduced with permission from Institute of Physics Publishing Limited.

for further analysis. Correlated kinematics between ionic fragments are used to deduce KER spectrum of fragmentation channels.

The KER spectrum of fragmentation of  $N_2^{++}$  into  $N^+$ ,  $N^+$  is shown in Fig. 3. The observed KER spectrum from the RIMS setup is shown by dots. The KER spectrum is plotted with 300 meV bin size, which represents the energy resolution for the two-body breakup. The loss corrected KER is shown by vertical lines. Loss because of finite detector size starts from 9.70 eV and increases with KER, whereas loss because of the dead time is significant only in the lower KER range. For the 60 V  $cm^{-1}$  field applied in the spectrometer and a 20 ns estimated deadtime of the detection system, the loss due to deadtime of detection for the  $N^+$ ,  $N^+$  pair is calculated to be  $0.155/\sqrt{KER}$ . The loss factors due to incomplete transmission and finite deadtime are also shown in the inset of Fig. 3. It is very interesting to note that a peak appears at 10.5 eV in the corrected spectrum, which was very weak in the raw spectrum. This is because the loss factor is a very rapid function of the KER initially. As shown in Fig. 2, for an increase in KER by 50% above  $KER_{lim}$ , loss increases by 60%. The peak at 10.5 eV has been observed in experiments in which transmission losses are negligible. One such spectrum, DFKER spectrum reported by Lundqvist et al., is shown in Fig. 3 [1]. There is one more broad structure in the KER spectrum at 15 eV, which becomes prominent after applying the corrections. This analysis clearly shows the importance of loss corrections in obtaining an accurate KER distribution. The cross-section for the breakup channel ( $N_2^{++} \rightarrow N^+ + N^+$ ) is thereby corrected upwards by 30%.

## 5. Loss analysis for other cases

### 5.1. Triple fragmentation

There are several complications that make it impossible to generalize the analysis of losses in three-body or higher fragmentations.

The breaking of the bonds may be simultaneous or step-wise. In a concerted breakup all fragments are ejected simultaneously and thus the conservation of momentum is described by a single equation relating all the fragments. In a sequential breakup, the order of

fragmentation will decide the conservation rules relating the fragments in the momentum equations [27–29]. It is also necessary to know that how much KER is released in each step separately. Depending on the masses of the fragments and kinetic energies release evolved in each step of the fragmentation, it may be possible to identify the fragment that is most likely to be lost, and a correction to the partial cross-section for that channel may be calculated.

There are several possibilities for the shape of the molecule and the transient molecular ion even for a triatomic molecule. The transient molecular ion may have more than one conformation as have been shown in many reports [30–33]. The momentum sharing between the fragments depends on the geometry of the transient molecular ion. For instance, in the complete atomization of a triatomic molecular ion in a linear geometry, the central fragment will have zero momentum, and only the terminal fragments will gain equal momentum after dissociation. Consequently, the loss factor will be governed by the lighter of the two terminal atoms. Whereas for a transient molecular ion having an equilateral triangle geometry, all fragments will have equal momenta (in case of concerted breakup) and the loss in recorded triple breakup events will be governed by the fragment having the smallest mass.

Cases in which geometry of the molecule has no obvious symmetries are even more difficult to handle because more momentum components appear in the breakup process. Calculation of losses for the processes having more than three-body fragmentation are even more complex because of the presence of more intermediate steps and involved geometries and consequently become less reliable.

### 5.2. Measurement of anisotropy

In a collision process, the directional dependence of the interaction Hamiltonian is a function of the momentum transfer (in the case of charged projectiles) or the polarization (in the case of photons). Since in a collision experiment all transverse directions of momentum transfer are equally likely, the resultant fragment distribution is anisotropic in the polar angle w.r.t. the projectile direction and symmetric in the azimuthal angle. In the case of photons similar considerations hold with the polarization vector as the reference axis. The loss patterns of the fragment ions in the anisotropic case then depend on the geometry of the spectrometer. If extraction of ions take place in the direction perpendicular to the plane of containing the projectile and target beams, anisotropy of the fragment distributions will show up as an absence of azimuthal symmetry on the detector plane. Geometries in which projectile direction and spectrometer axis are the same, the azimuthal symmetry would be maintained.

The degree of anisotropy is expressed by  $\beta$  parameter [34]. If there are losses in transmission, the value of  $\beta$  derived from an apparently asymmetric distribution may give a wrong conclusion about the anisotropy and thus the nature of interaction. For instance, if the Newton sphere has a distribution which is more intense along the extraction axis, then the lossy nature of the spectrometer will lead to an apparent enhancement of the anisotropy. On the other hand, if the true anisotropy is such that there is enhanced intensity perpendicular to the spectrometer axis, the intensity distribution appear to be less anisotropic. In general the anisotropy inferred from the observation would be wrong. In these cases, it is mandatory to confirm that there are no transmission losses.

## 6. Conclusion

We have obtained the general equation of the solid angle from which energetic ions formed in molecular fragmentation will be

lost in transmission in a typical ion momentum spectrometer. We have obtained expressions for the loss factor and the limiting value of the kinetic energy for the transmission of a single ion created in the ionization region. The loss factor in the KER spectrum of two-body fragmentation of a molecular system has also been derived. Effect of difference in the masses of fragments on the reliability of the KER spectra, cross-sections and branching ratios has been brought out. For three- or more than three-body fragmentation, loss depends on the geometry of the molecular ion as well as the fragmentation pathways. We have also discussed the effect of transmission loss on the anisotropy measurements and the limitations in obtaining a correction scheme. We conclude that, it is essential to perform the analysis of losses in such studies to get the correct picture of the fragmentation processes in all cases, and while it is possible to apply corrections to two-body fragmentations, it is not possible to do so in a generalized manner for three-body and anisotropic breakups.

## References

- [1] M. Lundqvist, D. Edvardsson, P. Baltzer, B. Wannberg, Doppler-free kinetic energy release spectrum of  $N_2^{2+}$ , *Journal of Physics B: Atomic, Molecular and Optical Physics* 29 (8) (1996) 1489.
- [2] P. Lablanquie, J. Delwiche, M.-J. Hubin-Franskin, I. Nenner, P. Morin, K. Ito, J.H.D. Eland, J.-M. Robbe, G. Gandara, J. Fournier, P.G. Fournier, Experimental and theoretical investigation of the spectroscopy and dynamics of multiply charged CO cations, *Physical Review A* 40 (1989) 5673–5689.
- [3] M. Tarisien, L. Adoui, F. Frémont, D. Lelièvre, L. Guillaume, J.-Y. Chesnel, H. Zhang, A. Dubois, D. Mathur, S. Kumar, M. Krishnamurthy, A. Cassimi, Ion-induced molecular fragmentation: beyond the coulomb explosion picture, *Journal of Physics B: Atomic, Molecular and Optical Physics* 33 (1) (2000) L11.
- [4] D. Mathur, L.H. Andersen, P. Hvelplund, D. Kella, C.P. Safvan, Long-lived, doubly charged diatomic and triatomic molecular ions, *Journal of Physics B: Atomic, Molecular and Optical Physics* 28 (15) (1995) 3415.
- [5] L.H. Andersen, J.H. Posthumus, O. Vahtras, H. Ågren, N. Elander, A. Nunez, A. Scrinzi, M. Natiello, M. Larsson, Very slow spontaneous dissociation of  $CO^{2+}$  observed by means of a heavy ion storage ring, *Physical Review Letters* 71 (12) (1993) 1812–1815.
- [6] U. Werner, N.M. Kabachnik, V.N. Kondratyev, H.O. Lutz, Orientation effects in multiple ionization of molecules by fast ions, *Physical Review Letters* 79 (9) (1997) 1662.
- [7] C. Caraby, A. Cassimi, L. Adoui, J.P. Grandin, Expected strong angular dependence of multi-ionization cross sections of diatomic molecules, *Physical Review A* 55 (3) (1997) 2450.
- [8] M.A. El Ghazaly, J. Jureta, X. Urbain, P. Defrance, Total cross sections and kinetic energy release for the electron impact dissociation of  $H_2^+$  and  $D_2^+$ , *Journal of Physics B: Atomic, Molecular and Optical Physics* 37 (12) (2004) 2467.
- [9] Y.-K. Kim, K.K. Irikura, M.A. Ali, Electron-impact total ionization cross sections of molecular ions, *Journal of Research of the National Institute of Standards and Technology* 105 (2) (2000) 285–291.
- [10] J.D. Bozek, N. Saito, I.H. Suzuki, Anisotropic dissociation of CO around the C K and O K ionization edges, *The Journal of Chemical Physics* 100 (1994) 393.
- [11] N. Saito, I.H. Suzuki, Asymmetry of departing fragment ion in the K-shell excitation of  $N_2$ , *Physical Review Letters* 61 (1988) 2740–2743.
- [12] J.D. Bozek, N. Saito, I.H. Suzuki, Asymmetry parameters for CO around the C K and O K ionization edges from the anisotropy of the ion distributions, *Physical Review A* 51 (6) (1995) 4563.
- [13] T.P. Rakitzis, A.J. van den Brom, M.H.M. Janssen, Directional dynamics in the photodissociation of oriented molecules, *Science* 303 (5665) (2004) 1852–1854.
- [14] A.I. Chichinin, K.-H. Gericke, S. Kauczok, C. Maul, Imaging chemical reactions – 3D velocity mapping, *International Reviews in Physical Chemistry* 28 (4) (2009) 607–680.
- [15] J. Ullrich, R. Moshhammer, A. Dorn, R. Dörner, L.P.H. Schmidt, H. Schmidt-Böcking, Recoil-ion and electron momentum spectroscopy: reaction-microscopes, *Reports on Progress in Physics* 66 (9) (2003) 1463.
- [16] M.N.R. Ashfold, N.H. Nahler, A.J. Orr-Ewing, O.P.J. Vieuxmaire, R.L. Toomes, T.N. Kitsopoulos, I.A. Garcia, D.A. Chestakov, S.-M. Wu, D.H. Parker, Imaging the dynamics of gas phase reactions, *Physical Chemistry Chemical Physics* 8 (1) (2006) 26–53.
- [17] H. Schmidt-Böcking, R. Dörner, O. Jagutzki, T. Jahnke, V. Mergel, L.P.H. Schmidt, T. Weber, A. Czasch, C. Wimmer, M. Hattass, A. Knapp, M. Schöffler, C.L. Cocke, M. Prior, A. Kheifets, E. Weigold, F. Afaneh, Many-particle dynamics in atomic and molecular physics investigated with the coltrims-technique: new insight into e–e correlation, *Nuclear Physics A* 737 (2004) 306–313.
- [18] R. Dörner, V. Mergel, O. Jagutzki, L. Spielberger, J. Ullrich, R. Moshhammer, H. Schmidt-Böcking, Cold target recoil ion momentum spectroscopy: a momentum microscope to view atomic collision dynamics, *Physics Reports* 330 (2) (2000) 95–192.
- [19] C. Ma, M.R. Bruce, R.A. Bonham, Absolute partial and total electron-impact-ionization cross sections for  $CF_4$  from threshold up to 500 eV, *Physical Review A* 44 (1991) 2921–2934.
- [20] E. Liénard, M. Herbane, G. Ban, G. Darius, P. Delahaye, D. Durand, X. Fléchar, M. Labalme, F. Mauger, A. Mery, O. Naviliat-Cuncic, D. Rodriguez, Performance of a micro-channel plates position sensitive detector, *Nuclear Instruments and Methods in Physics Research Section A: Accelerators, Spectrometers, Detectors and Associated Equipment* 551 (2) (2005) 375–386.
- [21] J.H. Sanderson, A. El-Zein, W.A. Bryan, W.R. Newell, A.J. Langley, P.F. Taday, Geometry modifications and alignment of  $H_2O$  in an intense femtosecond laser pulse, *Physical Review A* 59 (1999) R2567–R2570.
- [22] J. Ullrich, V.P. Shevelko, Many-Particle Quantum Dynamics in Atomic and Molecular Fragmentation, Springer-Verlag, Berlin Heidelberg, 2003.
- [23] Z. Amitay, D. Zajfman, P. Forck, U. Hechtfischer, B. Seidel, M. Grieser, D. Habs, R. Repnow, D. Schwalm, A. Wolf, Dissociative recombination of  $CH^+$ : cross section and final states, *Physical Review A* 54 (5) (1996) 4032.
- [24] I. Ali, R. Dörner, O. Jagutzki, S. Nüttgens, V. Mergel, L. Spielberger, K. Khayyat, T. Vogt, H. Bräuning, K. Ullmann, R. Moshhammer, J. Ullrich, S. Hagmann, K.-O. Groeneveld, C.L. Cocke, H. Schmidt-Böcking, Multi-hit detector system for complete momentum balance in spectroscopy in molecular fragmentation processes, *Nuclear Instruments and Methods in Physics Research Section B: Beam Interactions with Materials and Atoms* 149 (4) (1999) 490–500.
- [25] T.A. Field, J.H.D. Eland, Lifetimes of metastable molecular doubly charged ions, *Chemical Physics Letters* 211 (4) (1993) 436–442.
- [26] V. Sharma, B. Bapat, An apparatus for studying momentum-resolved electron-impact dissociative and non-dissociative ionisation, *The European Physical Journal D – Atomic, Molecular, Optical and Plasma Physics* 37 (2) (2006) 223–229.
- [27] F. Lègaré, K.F. Lee, I.V. Litvinyuk, P.W. Dooley, A.D. Bandrauk, D.M. Villeneuve, P.B. Corkum, Imaging the time-dependent structure of a molecule as it undergoes dynamics, *Physical Review A* 72 (2005) 052717.
- [28] C. Maul, K.-H. Gericke, Photo induced three body decay, *International Reviews in Physical Chemistry* 16 (1) (1997) 1–79.
- [29] S. Hsieh, J.H.D. Eland, Reaction dynamics of three-body dissociations in triatomic molecules from single-photon double ionization studied by a time- and position-sensitive coincidence method, *Journal of Physics B: Atomic, Molecular and Optical Physics* 30 (20) (1997) 4515.
- [30] V. Sharma, B. Bapat, Alteration of molecular symmetry during dissociative ionization, *Physical Review A* 75 (2007) 040503.
- [31] B. Bapat, V. Sharma, Bent dissociative states of  $CO_2^+$ , *Journal of Physics B: Atomic, Molecular and Optical Physics* 40 (1) (2007) 13.
- [32] T. Osipov, C.L. Cocke, M.H. Prior, A. Landers, T. Weber, O. Jagutzki, L. Schmidt, H. Schmidt-Böcking, R. Dörner, Photoelectron-photoion momentum spectroscopy as a clock for chemical rearrangements: isomerization of the di-cation of acetylene to the vinylidene configuration, *Physical Review Letters* 90 (23) (2003) 233002.
- [33] N. Neumann, D. Hant, L.P.H. Schmidt, J. Titze, T. Jahnke, A. Czasch, M.S. Schöffler, K. Krejdi, O. Jagutzki, H. Schmidt-Böcking, R. Dörner, Fragmentation dynamics of  $CO_2^{2+}$  investigated by multiple electron capture in collisions with slow highly charged ions, *Physical Review Letters* 104 (2010) 103201.
- [34] B.J. Whitaker, *Imaging in Molecular Dynamics: Technology and Applications*, Cambridge University Press, New York, 2003.